Thesis

Measurement of the carbon and oxygen fluxes and their ratio in cosmic rays with the AMS experiment on the international space station

LI, Yang

Abstract

One of the most fundamental measurements in cosmic rays is the determination of the rigidity dependent fluxes, or spectra, of primary nuclei in cosmic rays, such as H, He, C, and O. These primary nuclei are believed to be produced and accelerated by supernova. The spectra carry information about the acceleration and propagation of cosmic rays. Another class of nuclei is produced by nuclear interactions of these primary nuclei with interstellar matter, such as Li, Be, and B. The spectra and relative abundances of these nuclei reveal propagation parameters, such as the average amount of interstellar material traversed by cosmic rays and their age. This thesis discusses a measurement of the carbon and oxygen fluxes, as well as their ratio, in cosmic rays with rigidity from 2 GV to 2.6 TV, based on data collected by AMS during the first 5 years of operation onboard the International Space Station.

Reference

LI, Yang. *Measurement of the carbon and oxygen fluxes and their ratio in cosmic rays with the AMS experiment on the international space station*. Thèse de doctorat : Univ. Genève, 2017, no. Sc. 5114

URN : urn:nbn:ch:unige-974485
DOI : 10.13097/archive-ouverte/unige:97448

UNIVERSITÉ DE GENÈVE
Département de Physique Nucléaire et Corpusculaire

FACULTÉ DES SCIENCES
Professeur Martin Pohl

Measurement of the Carbon and Oxygen Fluxes and their Ratio in Cosmic Rays with the AMS Experiment on the International Space Station

THÈSE

présentée à la Faculté des sciences de l'Université de Genève
pour obtenir le grade de Docteur ès sciences, mention physique

par

Yang Li

de Chine

Thèse N° 5114

GENÈVE
Atelier d'impression ReproMail
2017

UNIVERSITÉ DE GENÈVE

FACULTÉ DES SCIENCES

DOCTORAT ÈS SCIENCES, MENTION PHYSIQUE

Thèse de Monsieur Yang LI

intitulée :

«Measurement of the Carbon and Oxygen Fluxes and their Ratio in Cosmic Rays with the AMS Experiment on the International Space Station»

La Faculté des sciences, sur le préavis de Monsieur M. POHL, professeur ordinaire et directeur de thèse (Département de physique nucléaire et corpusculaire), Monsieur X. WU, professeur associé (Département de physique nucléaire et corpusculaire), Monsieur T. GOLLING, professeur associé (Département de physique nucléaire et corpusculaire), Monsieur S. HAINO, docteur (Academia Sinica, Taipei City, Taiwan), Monsieur A. OLIVA, docteur (Centro de Investigaciones Energéticas, Medioambientales y tecnológicas, Madrid, España), autorise l'impression de la présente thèse, sans exprimer d'opinion sur les propositions qui y sont énoncées.

Genève, le 23 août 2017

Thèse - 5114 -

Le Doyen

N.B. - La thèse doit porter la déclaration précédente et remplir les conditions énumérées dans les "Informations relatives aux thèses de doctorat à l'Université de Genève".

Measurement of the Carbon and Oxygen Fluxes and their Ratio in Cosmic Rays with the AMS Experiment on the International Space Station

by

Yang Li

Abstract

One of the most fundamental measurements in cosmic rays is the determination of the rigidity dependent fluxes, or spectra, of primary nuclei in cosmic rays, such as H, He, C, O, Ne, Mg, Si, and Fe. These primary nuclei, of energies below the knee at $\sim 10^{15}$ eV, are believed to be produced in, and accelerated by, supernova remnants in our galaxy. The spectra carry information about the acceleration of cosmic rays and their subsequent propagation. Another class of nuclei is produced by nuclear interactions of these primary nuclei with interstellar matter, such as ^{3}He, Li, Be, B, F, and other sub-Fe nuclei. The spectra and relative abundances of these nuclei reveal propagation parameters, such as the average amount of interstellar material traversed by cosmic rays and their age.

This thesis discusses a measurement of the carbon and oxygen fluxes, as well as the carbon to oxygen flux ratio, in cosmic rays with rigidity (momentum per unit charge) from 2 GV to 2.6 TV, based on data collected by AMS during the first 5 years of operation (May 19, 2011 to May 26, 2016) onboard the International Space Station. The detailed variations with rigidity of the carbon and oxygen fluxes spectral indices are also discussed. A preliminary analysis of the ^{3}He to ^{4}He flux ratio as a function of kinetic energy per nucleon from 0.6 GeV/n to 10 GeV/n is also described.

Thesis Supervisor: Martin Pohl
Title: Professor

Résumé

Une des mesures les plus fondamentales concernant les rayons cosmiques est la détermination du flux en fonction de la rigidité, ou spectre, des rayons cosmiques primaires, comme H, He, C, O, Ne, Mg, Si, et Fe. Aux énergies en-dessous du "genou" à $\sim 10^{15}$ eV, ces noyaux primaires sont supposés être produits et accélérés dans des supernovae et leurs vestiges à l'intérieur de notre galaxie. Les spectres contiennent des informations concernant leur accélération et propagation. Une autre classe de noyaux, contenant ^{3}He, Li, Be, B, F, et autres noyaux plus légers que le fer, est produite par des interactions nucléaires des noyaux primaires avec le milieu interstellaire. Leur abondance relative et leurs spectres révèlent des paramètres de la propagation, comme par exemple la quantité moyenne de matière interstellaire traversée ainsi que leur âge.

Cette thèse traite la mesure des flux de C et O, et de leur rapport C/O, en rayons cosmiques avec une rigidité magnétique (quantité de mouvement par unité de charge électrique) entre 2 GV et 2.6 TV, basée sur les données collectionnées par AMS pendant ses premières 5 années d'opération (19 mai 2011 à 26 mai 2016), à bord de la Station Spatiale Internationale. Une analyse préliminaire du rapport des flux ^{3}He/^{4}He en fonction de l'énergie cinétique dans l'intervalle 0.6 GeV/n à 10 GeV/n est également traitée.

Acknowledgments

It has been a great pleasure and a unique experience working in the AMS collaboration. I am thankful to everyone involved in the development of this Ph.D. thesis.

Foremost, I would like to express my sincere gratitude to Profs. Samuel Ting and Zhenhui He for giving me the opportunity to join the AMS collaboration.

I am extremely grateful to Profs. Martin Pohl and Divic Rapin for making it possible to carry out my doctoral work within the AMS group at UNIGE. In particular, I highly appreciate the great expertise, enthusiasm, and continuous support Prof. Pohl has dedicated to the supervision of this work. He always provided insightful comments and suggestions when questions occurred. His excellent guidance throughout all parts of this work improved this thesis considerably.

I appreciate Prof. Xin Wu's unconditional support and valuable comments.

I would like to address special thanks to Prof. Sadakazu Haino for giving me the opportunity of preparing this work in collaboration with him and for providing outstanding support and endless patience during the development of this work. This doctoral work could not have been carried out without his encouragement and help.

I am indebted to Dr. Qi Yan for sharing his expert knowledge and creative ideas. Many aspects of particle physics and data analysis became clear to me thanks to the many discussions with him.

I would like to thank my thesis committee members for their interest, insightful questions, and helpful feedback.

I would also like to thank my colleagues of the AMS Nuclei Group, including Drs. Vitaly Choutko and Alberto Oliva. It was a pleasant and challenging activity working with the talented, inspiring, and devoted people in this group.

Thanks to the many friends I have made at CERN, including Drs. Mike Capell, Hai Chen, Melanie Heil, Andrew Levin, and Zhili Weng from MIT; Profs. Zhijun Liang and Zhicheng Tang from IHEP; Hsin-Yi Chou, Dr. William Creus, and Prof. Yuan-Hann Chang from NCU. Thanks to my former and current colleagues at UNIGE, especially Dr. Pierre Saouter and Stefania Vitillo for helpful discussions about physics.

Finally, never enough thanks to my family, especially for the little coming baby Clara, and to my dear lovely wife Dandan.

Contents

List of Figures

List of Tables

Introduction

Cosmic Rays (CRs) are fully ionized atomic nuclei and other particles filling the galactic space and reaching the Earth with energies starting at around 1 MeV and continuing to around 10^{21} eV. CRs contribute an energy density in the Galaxy of about 1 eV cm^{-3}.

The main component of high-energy particles in CRs are protons (hydrogen nuclei); about 10% are alpha particles (helium nuclei), and 1% are neutrons or heavier nuclei. Together, these account for 99% of the CRs, and the remaining 1% are electrons and photons [1]. The abundance of CR neutrinos is estimated to be comparable to that of high-energy photons, but it is very high at low energy because of the large production of neutrinos from the nuclear processes occurring in the Sun.

Solar energetic particles contribute to the CR spectrum (below a few GeV) [2]. CRs with energies above several GeV and less than $\sim 3 \times 10^{15}$ eV originate outside the solar system and are thought to be produced mainly by astrophysical sources in our Galaxy, the Milky Way. CRs with higher energies (above $\sim 10^{18}$ eV) are believed to have an extragalactic origin, with the transition region from galactic to extragalactic assumed to be in the 10^{15-17} eV band.

Primary CRs are high-energy protons and nuclei of heavier elements such as helium, carbon, and oxygen, plus a minority electron component, produced in and accelerated by astrophysical sources and arriving at Earth. The propagation path of these charged particles in the InterStellar Medium (ISM) is continuously deflected by galactic magnetic fields, therefore the propagation process of primary CRs gives important information on understanding the nature of CR accelerators.

Secondary CRs are those particles produced by collisions of the primaries with the

ISM. These include nuclei such as lithium, beryllium, and boron (rare end-products in stellar nucleosynthesis), as well as antiprotons and positrons. Whether a small fraction of antiprotons and positrons may be primary (e.g., from collisions of Dark Matter particles) is an open question of current primary interest. From the relative abundance of such secondaries, particularly the boron to carbon flux (B/C) ratio, we learn about how CRs propagate through the ISM and hence about the nature of the ISM, such as the dimension, matter density, and magnetic fields of the Galaxy. Understanding the propagation process is also of fundamental importance to understand Whether the excess of positrons could be a signal of physics beyond the Standard Model, indicating some evidence for Dark Matter.

The *Alpha Magnetic Spectrometer* (AMS) is a multipurpose high-energy particle detector installed on the International Space Station (ISS) on May 19, 2011 to conduct a unique long-duration ($\sim$ 20 year) mission of fundamental physics research in space. AMS allows a direct study of the CRs before their first interaction with the nuclei in Earth's atmosphere. One aim of this experiment is to measure the fluxes of galactic CR nuclei with absolute charge up to 26, as well as the flux ratios, in the GV–TV rigidity (momentum per unit charge) region with unprecedented precision.

The outline of this thesis is as follows:

Chapter 1 briefly reviews the origin, acceleration, and subsequent propagation processes of CRs in the Galaxy and discusses the physics and measurements of secondary-to-primary flux ratios of galactic CR nuclei.

Chapter 2 briefly presents the layout and description of the AMS detector, the trigger, the data acquisition system, and the Monte Carlo simulation.

Chapter 3 describes in detail the determination of the carbon and oxygen rigidity spectra, as well as systematic errors studies, and then presents the results of the carbon and oxygen fluxes and their ratio from 2 GV to 2.6 TV. The variations with rigidity of the carbon and oxygen flux spectral indices, as well as the spectral index of the carbon to oxygen flux ratio, are also discussed.

Chapter 4 describes a preliminary analysis of the helium isotopic composition, including the measurement strategy, analysis procedure, and studies on the statistical

and systematic errors. A preliminary result of the ^{3}He to ^{4}He flux ratio as a function of kinetic energy per nucleon from 0.6 GeV/n to 10 GeV/n is presented.

Chapter 1

Cosmic-Ray Nuclei in the Galaxy

1.1 Observations of Cosmic Rays

Since the discovery of CRs by Victor Hess [3] at the beginning of the twentieth century (1912), an enormous number of experiments have been performed on the Earth's surface (ground-based and underground), on balloons, on satellites, and even on space stations. From those data, we know today different properties of CRs, such as that CRs span many orders of magnitude in energy, and that they are of cosmic origin and travel through the interstellar space. However, the question of their production, acceleration, and propagation mechanism still remains challenging. This section gives a brief overview of the general phenomenology of CRs.

The experimental observables about CRs, from which one can learn about their origin and other properties, are principally the relative abundances of different nuclei and of their isotopic composition (*chemical composition*), the distribution in energy (*energy spectrum*) of each component, and the distribution of arrival directions. By comparing the chemical composition of various astrophysical objects, such as the Sun, the ISM, supernovae or neutron stars, one can obtain information about the CR acceleration sites. The observed energy spectra of CRs may be characteristic of two basic processes: the acceleration in the astrophysical sources and the subsequent propagation in the Galaxy. In order to better understand the physics of the acceleration mechanism, it is necessary to study the propagation process first.

1.1.1 Energy Spectrum

Figure 1-1 gives a global view of the energy spectrum of charged CRs with all the nuclear species summed together, the so-called all-particle spectrum, which spans over many decades in flux and energy. The flux covers an enormous range of energy, from less than a GeV to more than 10^{20} eV. Additionally, the flux falls rapidly with energy, from many thousands of particles per square meter per second at low energies ($E \sim 1$ GeV) to less than one particle per square kilometer per century at the highest energies ($E \sim 10^{20}$ eV).

The CR flux in Figure 1-1 is shown in a double-logarithmic scale. Below a few GeV the flux is modulated by solar activities and depends also on the magnetic latitude as it is affected by the local Earth geomagnetic field. Above few tens of GeV the differential flux as a function of energy, $\Phi(E)$, can be approximated by a power law:

$$\Phi(E) \equiv \frac{dN}{dE} = A \cdot E^{-\alpha}.$$

In a log-log scale, the power law becomes linear:

$$\log[\Phi(E)] = \log(A \cdot E^{-\alpha}) = \log(A) - \alpha \cdot \log(E).$$

The parameter α is the *differential spectral index* of the CR flux, or the slope of the CR spectrum in log-log scale, and A a normalization factor corresponding to the intercept with the y-axis in log-log scale. Since many CR spectra are steep (α being typically between 2 and 4), it is useful to weight the differential flux, the y-axis, with some power of the energy in order to flatten the steeply falling spectrum, and to look for features such as small changes in the spectral index. In this way, the straight line has a different slope:

$$\log[E^{\beta} \cdot \Phi(E)] = \log(A \cdot E^{-\alpha+\beta}) = \log(A) - (\alpha - \beta) \cdot \log(E).$$

The numerical values of the parameters, α and A, can be determined by fitting the experimental data.

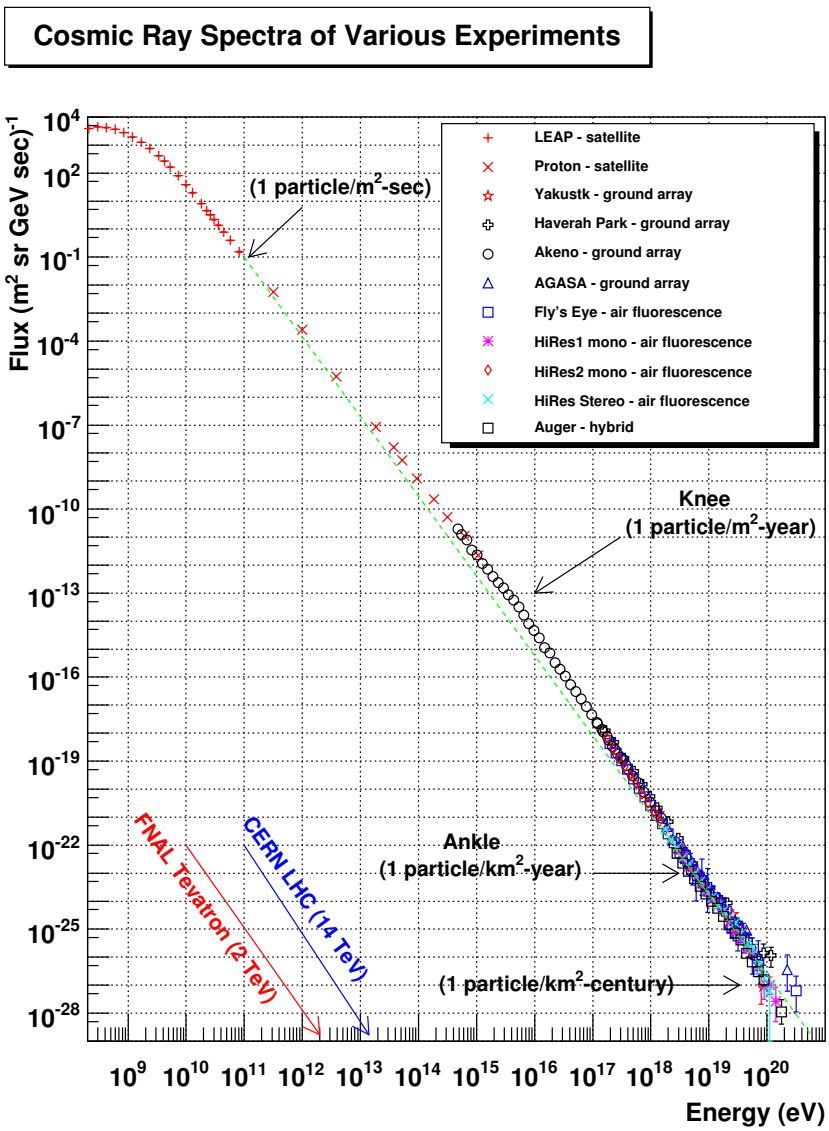

Figure 1-1: Differential energy spectrum of charged CRs of all types [4]. The green dashed line shows a E^{-3} spectrum. The blue and red arrows indicate the center-of-mass energy reached at the LHC at CERN and the Tevatron at Fermilab, respectively.

Figure 1-2 shows a representation of the all-particle CR flux multiplied by $E^{2.6}$, i.e., $\beta = 2.6$, from air shower measurements. The choice of $E^{\beta} = E^{\alpha}$ allows to represent the flux with a flat line parallel to the x-axis.

There are different quantities to describe the differential spectra of the CR components, and three main ones are shown below:

(1) By particles per unit rigidity. *Rigidity*, R, is defined as momentum per unit charge, or the Larmor radius (gyroradius), r_L, multiplied by the magnetic field

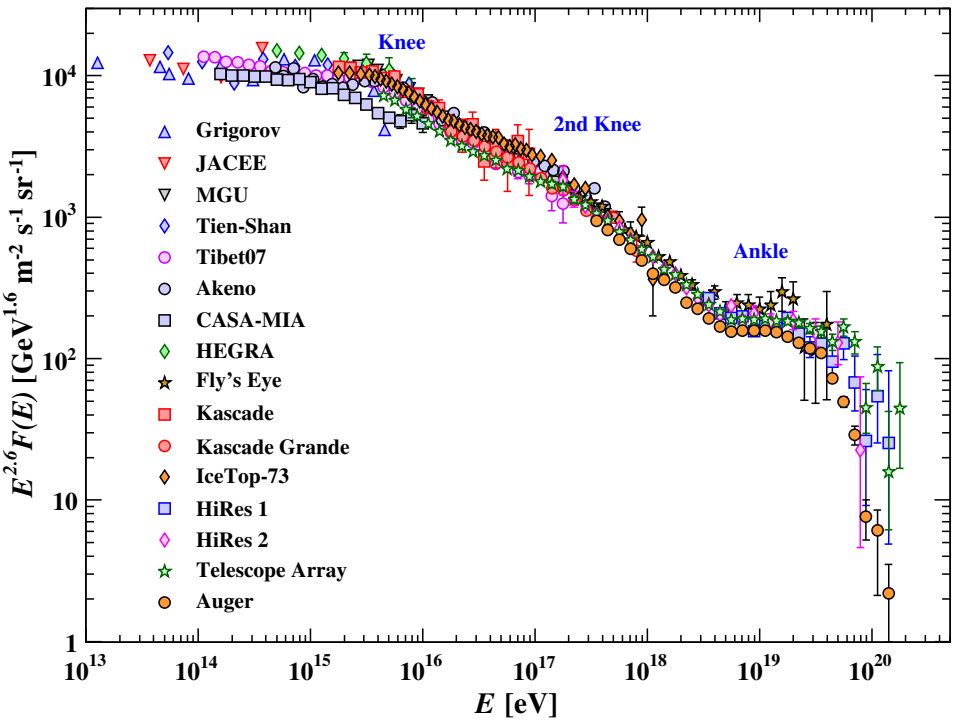

Figure 1-2: The all-particle CR spectrum as a function of energy per nucleus (E) from measurements by different air shower experiments. The spectrum has been multiplied by $E^{2.6}$. Taken from Ref. [5].

strength B:

$$R \equiv \frac{p}{Z} = r_L B.$$

As features of charged particle acceleration must depend on rigidity, spectra of charged CRs in this quantity may give information about their propagation (and probably also acceleration) through galactic or extragalactic magnetic fields. The rigidity is measured in [V].

(2) By particles per energy-per-nucleon. This spallation process of CR nuclei propagating through the ISM depends on energy per nucleon, which is approximately conserved when a CR nucleus breaks up due to interaction with nuclei of the ISM. The energy-per-nucleon is measured in [GeV/nucleon] or [GeV/A]

or [GeV/n], where the "A" or "n" stands for "nucleon".

(3) By particles per energy-per-nucleus. Generally the energy-per-nucleus is measured when a experiment measures a quantity that is related to total energy by using, e.g., a calorimeter. The energy-per-nucleus is measured in [GeV].

The unit of differential flux $\Phi(E)$ is $[\mathrm{m}^{-2}\mathrm{s}^{-1}\mathrm{sr}^{-1}\mathcal{E}^{-1}]$, where $\mathcal{E}$ is one of the three quantities' units listed above.

A remarkable feature of Figure 1-2 is that two transition points are clearly visible corresponding to the changes in the spectral index. The first transition point, known as the *knee* of the spectrum, occurs at $\sim 3 \times 10^{15}$ eV [6, 7]. The second clear break point, the *ankle*, occurs at an energy of $\sim 4 \times 10^{18}$ eV [8]. Finally, at the highest energies ($\sim 10^{20}$ eV) a cutoff of the spectrum appears [9, 10]. Another feature is at $\sim 4 \times 10^{17}$ eV, called the *second knee*. These features define several energy regions in the CR spectrum, in which the changes of the differential spectral index α are as follows.

From 10 GeV to the knee (10^{15} eV), the differential spectral index is $\alpha \sim 2.7$; from the knee to the ankle (10^{18} eV), $\alpha \sim 3.1$; above 10^{19} eV, $\alpha \sim 2.6$ and then at about 10^{20} eV the spectrum cuts off. Around the second knee, there is a softening of the spectrum (i.e., from $\alpha \sim 3.1$ to $\alpha \sim 3.3$) before the hardening at the ankle. CR physicists usually refer to α becoming larger (smaller) as the *spectral softening (hardening)*. An energy spectrum becomes harder when having more high-energy particles. The knee is commonly associated to propagation effects and a transition between two populations of CRs (galactic and extragalactic) [11, 12]. This is mainly because the galactic magnetic field is not able to confine CRs with energy above $\sim 10^{18}$ eV given the limited size and magnetic field strength of the confinement region. The cutoff at $\sim 10^{20}$ eV may be due to interactions between extragalactic CR protons and Cosmic Microwave Background (CMB) photons, the so-called Greisen-Zatsepin-Kuz'min (GZK) effect [13, 14].

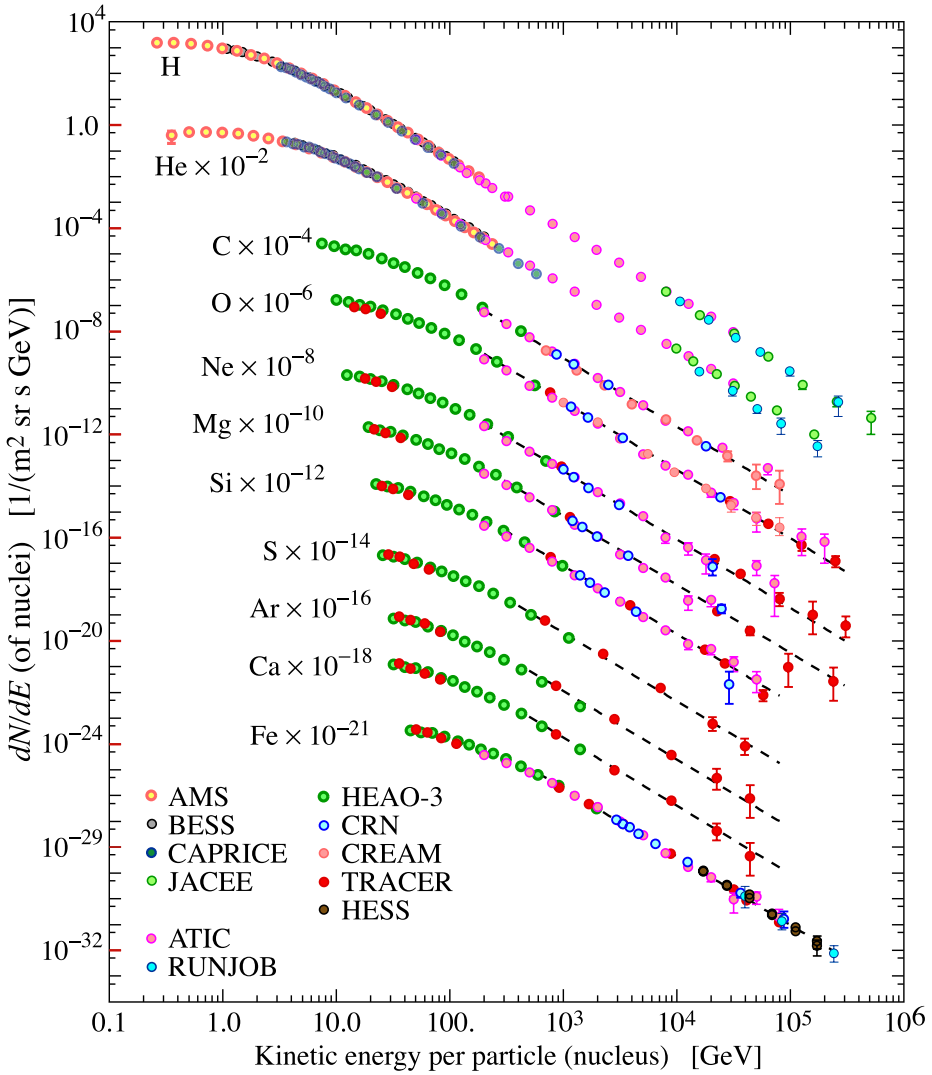

Figure 1-3: Fluxes of primary CR nuclei as functions of energy-per-nucleus. Taken from Ref. [5].

1.1.2 Chemical Composition

CRs are mainly protons ($\sim 90\%$) and heavier nuclei. Precise knowledge of the chemical composition of CRs also provides essential information about the origin, acceleration, and propagation history of CR particles. One particular way is to compare the relative abundances of nuclear species in CRs with those in the solar system. Figure 1-3 shows the absolute fluxes of the main components of primary CR nuclei arriving at Earth. The relative abundances of elements with $Z \leq 28$ in CRs are shown in Figure 1-4 and are compared with the abundances in the solar system. Both

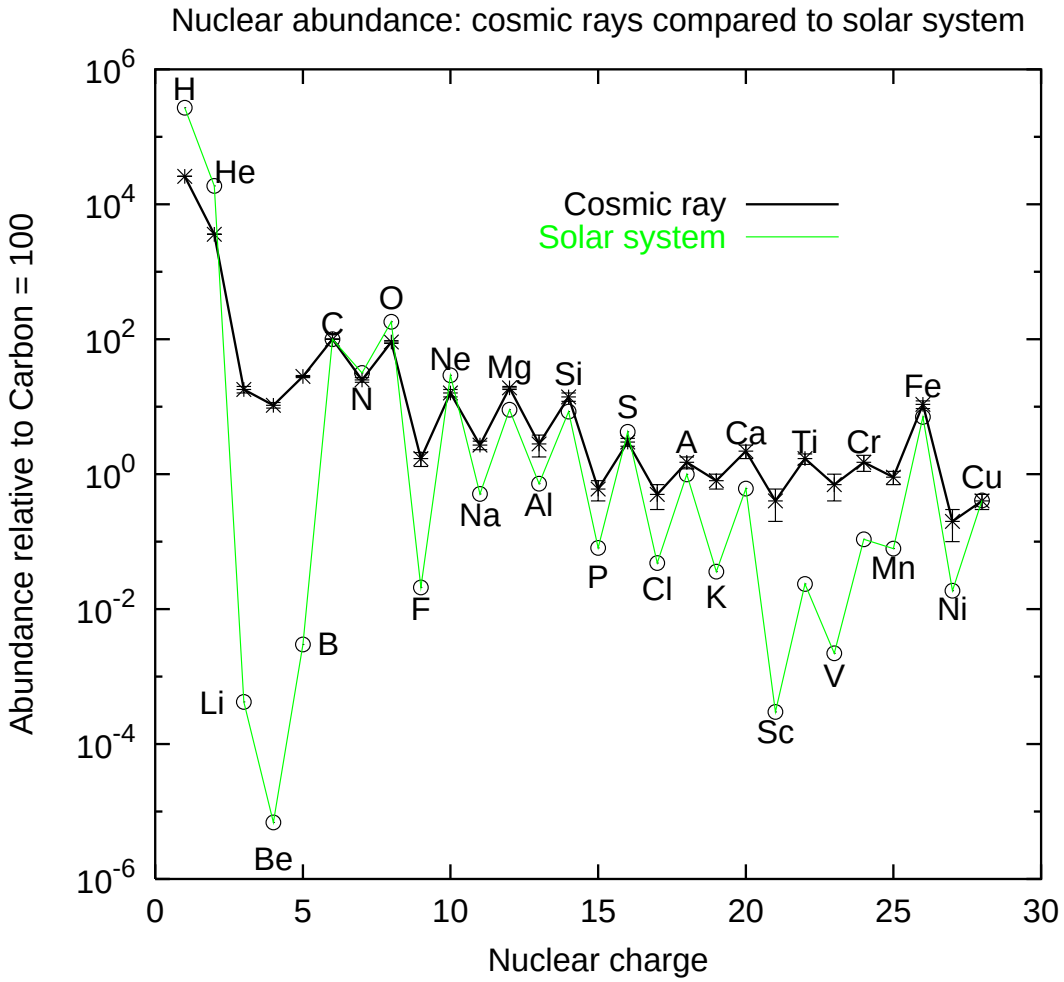

Figure 1-4: Comparison of the elemental abundances in CRs and in the solar system. Both are normalized to the abundance of carbon = 100. Taken from Ref. [18].

show the well known odd-even effect, i.e., even-Z nuclei (more tightly bound) being more abundant than odd-Z nuclei. Also, both abundances exhibit a similarity on the "peaks" (even-Z nuclei) besides a clear deficit of hydrogen (H) and helium (He). The underabundance of H and He in CRs, however, is one of the two remarkable differences in this comparison. This difference is not fully understood, but may be due to the fact that H is relatively hard to ionize and inject into the acceleration process, or that a genuine difference indeed exists in the composition of the sources [15, 16]. Another possibility is that galactic CR H and heavier nuclei are accelerated by different sources [16, 17].

The second difference is the overabundance of Li, Be, B (below the C peak) and

Sc, Ti, V, Cr, Mn (below the Fe peak) elements ("valley" elements in Figure 1-4) in the CRs. This difference is thought to be an important tool for understanding the propagation and confinement of CRs in the Galaxy. It can be explained within a scenario that primary CR nuclei, such as C, O, and Fe, are produced in stellar endproducts, while the secondaries, such as Li, Be and B, are produced by collisions of heavier elements in primary CRs with the ISM, which is called the spallation process. With the knowledge of the spallation cross-sections of the relevant nuclei at GeV energies, the secondary-to-primary flux ratio of stable nuclei in CRs not only provides a measure of the average amount of the ISM that CRs have traversed, but also can be used to infer the average escape time (or confinement time), $\tau_{\rm esc}$, of CRs in the Galaxy. In particular, the boron to carbon flux ratio is the standard reference ratio used to deduce the energy dependence of $\tau_{\rm esc}$. This is mainly due to 1) that B are entirely secondary, produced by collisions of heavier primary CR nuclei, mainly C, N, and O, with the ISM and 2) that the spallation cross-sections are better known than those of Be and Li. This is discussed in Section 1.2.5.

1.1.3 Anisotropy

The arrival direction of charged CRs is nearly isotropic at most energies due to the diffusive propagation effects in the galactic magnetic field [11], which provide a necessary mechanism for efficiently randomizing CR directions.

A small but statistically significant anisotropy in the arrival direction distribution of high-energy CRs has been observed with several experiments in the northern and southern hemispheres, with an amplitude of the order of 10^{-4}–10^{-3} in relative intensity. In the northern hemisphere, this anisotropy has been observed in the energy range from tens to hundreds of GeV with muon detectors [19–21]; from one to tens of TeV with the Tibet ASγ [22, 23], Super-Kamiokande [24], Milagro [25, 26], MINOS [27], ARGO-YBJ [28, 29] and HAWC [30] experiments; and above 100 TeV with the EAS-TOP [31] experiment. In the southern hemisphere, it has been observed with the IceCube Neutrino Observatory up to $\sim$ 400 TeV [32–35] and its air shower array, IceTop, up to $\sim$ 2 PeV [36]. In both hemispheres, observations show similar results.

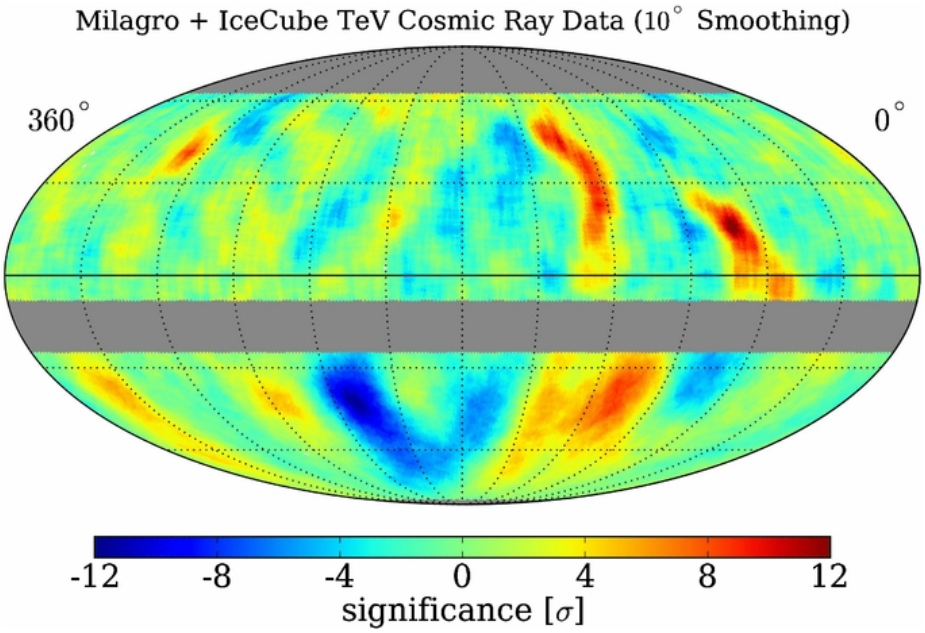

Figure 1-5: Significance sky maps of CR anisotropy observed by Milagro in the northern hemisphere [25] and IceCube in the southern hemisphere [33]. Taken from Ref. [33].

The galactic CR flux has anisotropies both on large angular scales ($> 60°$) and on smaller scales (typically between $\sim 10°$ and $\sim 30°$). Figure 1-5 shows the combined sky map of small-scale anisotropy observed by Milagro with a median energy of 1 TeV [25] and IceCube with a median energy of 20 TeV [33].

The origin of such anisotropies in the distribution of galactic CR arrival directions on the sky is not well understood at these energies. The large angular scale anisotropy could be explained by the diffusive transport of CRs from nearby sources in the Galaxy [37–43]. The motion of the solar system (the Compton-Getting effect [44, 45]) may also contribute to the CR anisotropy. On the other hand, the intermediate and small angular scale anisotropy could be an effect of interstellar magnetic turbulence [46–48], potentially with an additional heliospheric influence [49, 50].

1.2 Galactic Cosmic Rays

It is believed that CRs with energies up to the knee ($\sim 10^{15}$ eV) are produced in and accelerated by galactic sources. The origin of the galactic CRs is thought to

be associated with the most energetic astronomical objects in the Galaxy, primarily with supernovae and their products—Superova Remnants (SNRs) [51] and pulsars. The energy spectra of galactic CRs are shaped by two basic processes—the acceleration in the sources and the subsequent propagation in the ISM. The bulk of galactic CRs are believed to be accelerated in SNRs in our Galaxy [52, 53]. After leaving the sources, the charged CR particles diffuse in random magnetic fields, which accounts for the high isotropy of galactic CRs and their relatively long confinement time in the Galaxy. This galactic diffusion model explains the data on CR energy spectra, composition, and anisotropy. Combining the diffusive propagation model in the Galaxy, the idea that charged CRs are primarily accelerated in SNR shocks through diffusive shock acceleration (DSA) [54–58] is generally referred to as the *supernova remnant paradigm* [59] for the origin of galactic CRs.

1.2.1 Acceleration Mechanism

The power-law CR energy spectrum below the knee is thought to be the result of CR acceleration in SNR shocks [60]. The spectrum is softened to the observed index $\alpha \sim 2.75$ by subsequent propagation in the ISM and eventual leakage from the Galaxy. Charged CRs produced by particle ejection in possible astrophysical sources in the Galaxy may be accelerated in regions where strong turbulent magnetic fields exist. In 1949 Enrico Fermi [61] proposed an acceleration mechanism[1] in which particles could gain energy through stochastic and random collisions with clouds in the ISM. This process is currently widely refered to as *second-order Fermi acceleration*. These interstellar clouds move randomly with characteristic velocity V and act as magnetic mirrors from which charged particles are reflected, as shown in Figure 1-6. By assuming a characteristic escape time, $\tau_{\rm esc}$, this original version of Fermi's theory results in a power-law distribution of particle energies. Particle energy is gained during a head-on collision and lost during a tail-on collision, as shown in Figure 1-7. The parameters are:

[1] In this section the description and calculation of second- and first-order Fermi acceleration [62] follow Longair's textbook [16].

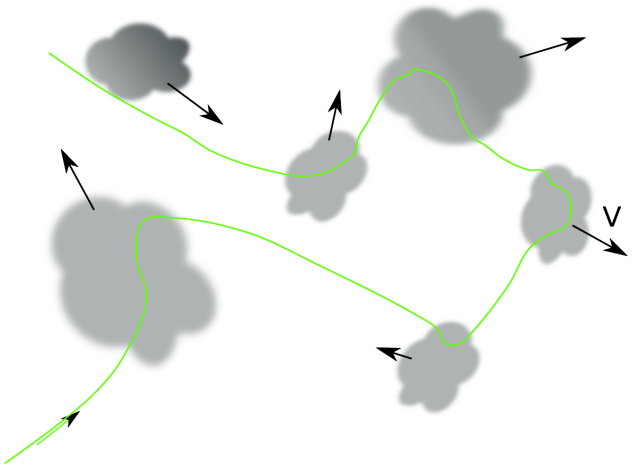

Figure 1-6: Reflection of particles due to magnetic mirror effects.

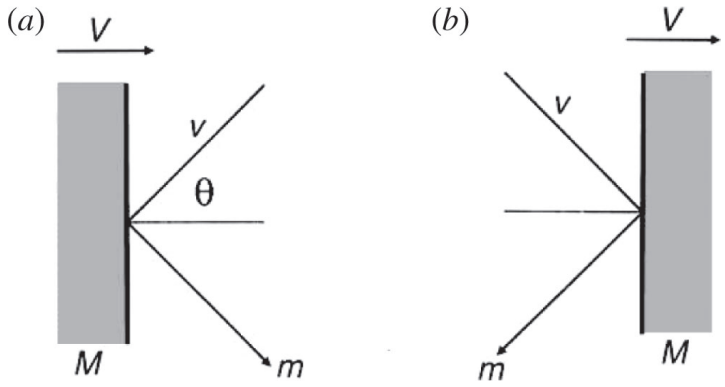

Figure 1-7: Geometry of collisions between a particle of mass m and a cloud of mass M: (a) a head-on collision; (b) a tail-on collision. Taken from Ref. [62].

- V: characteristic velocity of the cloud in observer's frame,
- v: velocity of particle,
- θ: angle of incidence,
- m: particle mass ($\ll M \equiv$ cloud mass).

One key point is that head-on collisions are more likely than tail-on collisions: the probability of a head-on collision is proportional to $v + V\cos\theta$, while the probability of a tail-on collision is proportional to $v - V\cos\theta$. Here we consider a fully relativistic analysis. The particle energy E in the cloud's (center of momentum) reference frame

is

$$E' = \gamma(E + Vp\cos\theta), \tag{1.1}$$

where p is the particle's momentum and $\gamma = (1 - V^2/c^2)^{-1/2}$. The x-component of momentum in the cloud's frame is

$$p'_{\rm x} = p'\cos\theta' = \gamma\left(p\cos\theta + \frac{VE}{c^2}\right). \tag{1.2}$$

In the collison, the particle's energy is conserved, and the x-component of the particle's momentum is reversed, $p'_{\rm x} \to -p'_{\rm x}$. Then transforming back to the observer's frame, we get

$$E'' = \gamma(E' + Vp'_{\rm x}). \tag{1.3}$$

Combining Eqs. (1.1), (1.2), and (1.3) yields the particle energy in the observer's frame:

$$E'' = \gamma^2 E\left[1 + \frac{2Vv\cos\theta}{c^2} + \left(\frac{V}{c}\right)^2\right].$$

Then expanding to second order in V/c and solving for ΔE, we find:

$$\Delta E \equiv E'' - E = E\left[\frac{2Vv\cos\theta}{c^2} + 2\left(\frac{V}{c}\right)^2\right]. \tag{1.4}$$

Now we still need to average over the angle of incidence, θ. Assuming that the particle is randomly scattered in pitch angle (distribution of angles is random) and that the particles are relativistic ($v \approx c$), and using that the probability of an angle between θ and $\theta + d\theta$ is proportional to $\sin\theta d\theta$, we average θ over the range from 0 to π and find the average of the θ-dependent term (the first term) in Eq. (1.4) becomes

$$\left\langle\frac{2V\cos\theta}{c}\right\rangle = \left(\frac{2V}{c}\right)\frac{\int_{-1}^{1} X[1 + (V/c)X]dX}{\int_{-1}^{1}[1 + (V/c)X]dX} = \frac{2}{3}\left(\frac{V}{c}\right)^2,$$

where $X = \cos\theta$. Including the last term in Eq. (1.4) , the average energy gain per collision is

$$\left\langle \frac{\Delta E}{E} \right\rangle = \frac{8}{3}\left(\frac{V}{c}\right)^2. \tag{1.5}$$

The average increase in energy is proportional to $(V/c)^2$, so the process is known as "second-order" acceleration owing to the value of the exponent. If we define L as the mean free path between clouds along the field lines and ϕ as the pitch angle, the time between collisions is $\sim L/c\cos\phi$, which can be averaged to $2L/c$, then the average rate of energy increase can be derived from Eq. (1.5):

$$\frac{dE}{dt} = \frac{4}{3}\left(\frac{V^2}{cL}\right)E = \alpha E. \tag{1.6}$$

It is possible to obtain the energy spectrum, $N(E)$, of the accelerated particles by solving a diffusion-loss equation in steady state, considering this energy rate, Eq. (1.6), and assuming that $\tau_{\rm esc}$ is the characteristic time for a particle to remain in the acceleration region (or the escape time). And the solution is [62]

$$N(E) = \text{constant} \times E^{-x} \tag{1.7}$$

where $x \equiv 1+(\alpha\tau_{\rm esc})^{-1}$. Thus, the second-order Fermi acceleration mechanism results in a power-law energy spectrum, but note that α and $\tau_{\rm esc}$ are model-dependent.

Although the second-order Fermi acceleration succeeds in predicting a power-law spectrum, there are some problems with this mechanism, e.g.,

1) The random velocities of clouds are relatively small: $V/c \lesssim 10^{-4}$, and the observed cloud density is low. For a CR mean free path of ~ 0.1 pc, collisions would likely occur only a few times per year. Thus, there is very little chance of a significant particle energy gain.
2) This theory does not include energy losses that compete with energy gains (e.g., ionization).
3) The theory fails to predict the observed value of $\sim$2.7 for the exponent in the power-law spectrum.

4) Energy gains are second-order, $\sim \mathcal{O}(V^2/c^2)$; some collisions result in energy losses.

In 1954, Fermi proposed a more efficient way of accelerating CRs in which every interaction resulted in an increase in energy, turning the energy gain $\sim \mathcal{O}(V/c)$ (*first-order Fermi acceleration*) [63]. The DSA process is first-order Fermi acceleration in the presence of strong shock waves where charged particles can bounce back and forth between upstream and downstream of the shock.

In order to formulate the Fermi acceleration mechanism in a more general way, we define $E = \beta E_0$ as the average energy of the particle after a collision, where E_0 is the energy before the collision, and define P as the probability that the particle remains in the acceleration region after a collision. After k collisions there are $N = N_0 P^k$ particles with energies $E = E_0 \beta^k$. Hence, the energy spectrum is

$$N(E)\, dE = \text{constant} \times E^{-1+(\ln P/\ln \beta)}\, dE.$$

From second-order Fermi acceleration, or Eq. (1.7), this means that

$$\frac{\ln P}{\ln \beta} \equiv -(\alpha \tau_{\text{esc}})^{-1}.$$

The first-order Fermi acceleration can occur when the relativistic particles collide with strong shock waves (e.g., produced in supernova explosions or active galactic nuclei), which can reach supersonic velocities ($\sim 10^3$ times the velocity of an interstellar cloud).

Due to the turbulence behind the shock and the irregularities in front of it, the particle velocity distribution is isotropic in the frame of reference in which the interstellar gas is stationary on either side of the shock front. As a result, in this reference frame the particle energy gain is symmetric for particles crossing the shock from downstream to upstream and from upstream to downstream. Ref. [16] shows

that in a round trip of crossing the shock the average fractional energy increase is

$$\left\langle \frac{\Delta E}{E} \right\rangle = \frac{4}{3}\frac{V}{c},$$

which means that the energy change after a round trip is

$$\beta = \frac{E}{E_0} = 1 + \frac{4}{3}\frac{V}{c}.$$

Another quantity to work out is the particle escape probability from the shock, $P_{\rm esc} \equiv 1 - P$. Using classical kinetic theory, one can obtain

$$P_{\rm esc} = \frac{4}{3}\frac{V}{c}.$$

So that we have

$$\begin{aligned} \ln P &= \ln\left(1 - \frac{4}{3}\frac{V}{c}\right) \simeq -\frac{4}{3}\frac{V}{c}, \\ \ln \beta &= \ln\left(1 + \frac{4}{3}\frac{V}{c}\right) \simeq \frac{4}{3}\frac{V}{c}, \\ \Rightarrow \frac{\ln P}{\ln \beta} &= -1. \end{aligned}$$

The differential energy spectrum is then

$$N(E)\, dE \propto E^{-2}\, dE.$$

The first-order Fermi acceleration predicts a value of the power law exponent which is not too different from the observed value of ~ 2.7 for galactic CRs.

In summary, the first-order Fermi acceleration mechanism provides an efficient way for accelerating CR particles in SNR shock waves. This model requires that particle velocity vectors are randomized in both the upstream and downstream regions of the shock.

1.2.2 Propagation

After leaving the source, charged CRs produced in our Galaxy diffuse in random magnetic fields of the order of $\sim \mu$G throughout the ISM before reaching Earth. In the SNR shock waves acceleration mechanism, reacceleration, and propagation of charged CRs in the Galaxy are related, i.e., both processes are affected by the diffusive scattering of CR particles by irregularities in the galactic magnetic field.

1.2.3 Diffusion Model

The ISM is composed primarily of hydrogen; the remainder is helium plus only trace amounts of carbon, oxygen, and nitrogen comparative to hydrogen [64]. The diffusion model [11, 12, 65] is the basic model for the investigation of galactic CR propagation in the ISM. It manages to explain the gross features of the data on energy spectra, composition, and anisotropy of CRs. In this model, the CR propagation equation[2] includes different physics processes such as diffusion, convection (by galactic winds), energy losses or gains (diffusive reacceleration in the ISM), nuclear spallation, radioactive decay, and production of secondary particles and isotopes.

For a particular particle species, the CR propagation equation can be written as

$$\begin{aligned}\frac{\partial\psi(\vec{r},\,p,\,t)}{\partial t} =& q(\vec{r},\,p,\,t)\\ &+\vec{\nabla}\cdot(D_{xx}\vec{\nabla}\psi-\vec{V}\psi)\\ &+\frac{\partial}{\partial p}\left(p^2D_{pp}\frac{\partial}{\partial p}\frac{\psi}{p^2}\right)-\frac{\partial}{\partial p}\left[\dot{p}\psi-\frac{p}{3}(\vec{\nabla}\cdot\vec{V})\psi\right]\\ &-\frac{\psi}{\tau_{\rm f}}-\frac{\psi}{\tau_{\rm r}},\end{aligned} \tag{1.8}$$

where

(i) $\psi=\psi(\vec{r},\,p,\,t)$ is the CR number density per unit of total particle momentum p at position $\vec{r}$ and time t, i.e., $\psi(p)dp = 4\pi p^2 f(\vec{p})dp$ in terms of phase-space density $f(\vec{p})$;

(ii) $q(\vec{r},\,p,\,t)$ is the CR source term including primary, nuclear spallation and decay

[2] In this section the description of the CR propagation equation follows Ref. [12]

contributions; primaries may be produced by CR sources whose distribution is discrete in space and time;

(iii) D_{xx} is the spatial diffusion tensor (when assuming an isotropic diffusion process the notation D will be used as the scalar diffusion coefficient);

(iv) $\vec{V}$ is the convection velocity;

(v) D_{pp} is the diffusion coefficient in momentum space and determines the diffusive reacceleration by the interstellar turbulence;

(vi) $\dot{p} \equiv dp/dt$ is the momentum gain or loss rate;

(vii) $\tau_{\rm f}$ is the timescale for loss by fragmentation;

(viii) $\tau_{\rm r}$ is the timescale for radioactive decay.

The first line on the right-hand side of Eq. (1.8) accounts for the sources (CR injection spectrum); the second line for the diffusion and convection; the third line for the density changes due to energy losses or gains (reacceleration); and the fourth line for the losses due to spallation and radioactive decay.

GALPROP [66] and DRAGON2 [67] are two of the most well-known and advanced projects developed for the numerical calculations of CR propagation.

1.2.4 Leaky Box Model

The leaky box model [68] is a steady-state solution for the transport of CRs through the ISM. It is a simpler model that can be used to explain the main features of the experimental data.

In the leaky box model, charged CRs propagate freely in a containment volume (box) in which particles are injected by sources q uniformly distributed, and the volume is filled with a uniform distribution of matter and radiation fields. Charged CRs can escape from this volume with a characteristic escape time $\tau_{\rm esc}$ independent of position. Under the leaky box approximation, no spatial dependence of CR distribution, source density, escape time, and any other parameters is taken into account, and the diffusion and convection terms are approximated by the leakage term so that the terms $\vec{\nabla} \cdot (D_{xx}\vec{\nabla}\psi - \vec{V}\psi)$ in Eq. (1.8) are substituted by the term $-\psi/\tau_{\rm esc}$, with the time scale of escape $\tau_{\rm esc}$ being inversely proportional to the spatial diffusion coefficient

$$\tau_{\rm esc} \propto D^{-1}. \tag{1.9}$$

For the calculations of abundances of not very heavy stable nuclei, the leaky box model can be a correct approximation to the (flat-halo) diffusion model. However, the leaky box model cannot be applied to the propagation of electrons and positrons due to the much higher energy losses (dominated by synchrotron radiation and inverse Compton scattering) and to the much higher escape probability.

Considering number density $\psi(E)$ of only one CR species and neglecting energy losses, the CR transport equation becomes a simplified verson:

$$\frac{\partial \psi(E)}{\partial t} = -\frac{\psi(E)}{\tau_{\rm esc}} + q(E). \tag{1.10}$$

In steady state $\partial\psi(E)/\partial t = 0$ (flux independent of time), Eq. (1.10) becomes

$$\begin{aligned} 0 &= -\frac{\psi(E)}{\tau_{\rm esc}} + q(E), \\ \Rightarrow \psi(E) &= \tau_{\rm esc}\, q(E). \end{aligned} \tag{1.11}$$

Theoretical prediction for $q(E)$ (e.g., first-order Fermi acceleration mechanism) is $\sim E^{-2}$, while from observations we learn $\sim E^{-2.7}$. Thus, $\tau_{\rm esc}$ has to be energy-dependent and required by observations $\tau_{\rm esc} \propto E^{-0.7}$. Energy per unit charge (E/Z) is important if diffusion in magnetic fields determines the escape process, and then there is the prediction: $\tau_{\rm esc} \propto (E/Z)^{-0.7}$. Therefore, with a $\tau_{\rm esc} \sim 10^7$ yr the CR density is enhanced by a factor of 10^3–10^4 relative to free streaming.

1.2.5 Stable Secondary-to-Primary Ratios

From the measurement of the secondary-to-primary flux ratios of stable nuclei, such as the B/C ratio or the flux ratio of sub-iron elements to iron, one can infer 1) the energy dependence of the CR escape time which provides an important constraint on the spectral index of CRs at the sources and 2) the average amount of ISM traversed

by CRs between injection and observation.

For stable CR nuclei, among different factors in the propagation equation the diffusion process is the most effective at high energies. The source of primary CRs (injection spectrum) is power-law energy dependent, $E^{-\gamma}$. With the use of the steady state assumption and Eqs. (1.9) and (1.11), the energy dependence of the number density of CR primaries $\psi_{\rm pri}$ can be obtained:

$$\psi_{\rm pri} \propto q_{\rm pri}\, \tau_{\rm esc} \propto E^{-\gamma}\, D^{-1} \propto E^{-\gamma+\delta}. \tag{1.12}$$

The energy dependence of the number density of CR secondaries is given by

$$\psi_{\rm sec} \propto q_{\rm sec}\, \tau_{\rm sec} \propto \psi_{\rm pri}\, P_{\rm f}\, \tau_{\rm sec} \propto E^{-\gamma+\delta}\, D^{-1} \propto E^{-\gamma+2\delta}. \tag{1.13}$$

where $P_{\rm f}$ is the probability of fragmentation of the primaries. Combining Eqs. (1.12) and (1.13) results in

$$\begin{aligned} &\frac{\psi_{\rm sec}}{\psi_{\rm pri}} \propto E^{\delta} \\ \Rightarrow\ &\frac{\psi_{\rm sec}}{\psi_{\rm pri}} \propto R^{\delta},\ \text{(if rigidity } R \text{ is measured)} \end{aligned} \tag{1.14}$$

where the spatial diffusion coefficient dependence on rigidity is

$$D \propto R^{-\delta}. \tag{1.15}$$

In Eqs. (1.14) and (1.15), the dependence is expressed in rigidity (rather than kinetic energy per nucleon) so that it can be compared with other nuclei. This is due to the fact that propagation in magnetic fields is identical for different CR particles in terms of rigidity but not kinetic energy per nucleon. Most importantly, it can be inferred from Eq. (1.14) that the spectral slope of the secondary-to-primary flux ratio at high rigidities is determined by δ.

The reference ratio is the B/C ratio. Carbon nuclei in CRs are thought to be mainly produced by and accelerated in astrophysical sources, while boron nuclei are

Table 1.1: Summary of recent direct measurements of cosmic-ray boron flux, carbon flux, and their ratio.

Experiment	**Measurement**	**Energy range**	**Experimental technique**
HEAO-3-C2 [72]	B flux, C flux, B/C	0.6–35 [GeV/n]	Čerenkov counters
CRN-Spacelab2	C flux [73] B flux, B/C [74]	73–1503 [GeV/n] 73–207 [GeV/n]	Čerenkov counters and Transition radiation detector
Buckley *et al.* [75]	C flux B/C	4–139 [GeV/n] 4–65 [GeV/n]	Ring imaging Čerenkov detector
ATIC-2	C flux [76] B/C [77]	18–2516 [GeV/n] 20–307 [GeV/n]	Calorimeter
CREAM-I [78]	B/C	1–4000 [GeV/n]	Transition radiation detector and Calorimeter
CREAM-II [79]	C flux	66–12834 [GeV/n]	Calorimeter
TRACER	B flux, C flux [80], B/C [81]	0.8–5000 [GeV/n]	Čerenkov detector and Transition radiation detector
PAMELA [82]	B flux, C flux, B/C	2–260 [GV], 0.4–129 [GeV/n]	Magnetic spectrometer
AMS-02 [83]	B/C	1.9–2300 [GV], 0.4–1300 [GeV/n]	Magnetic spectrometer

entirely secondary, i.e., produced by collisions of heavier primary CR nuclei, such as carbon and oxygen, with nuclei of the ISM. Moreover, carbon and oxygen being the major progenitors of boron in CRs, the production cross-sections are better measured than those of other secondaries such as lithium and beryllium.

The diffusion spectral index δ is predicted to be $\delta = -1/3$ with the Kolmogorov theory of interstellar turbulence [69,70], or $\delta = -1/2$ using the Kraichnan theory [71]. The measured B/C spectral index Δ, obtained from a fit at high rigidities of $(\mathrm{B/C}) \propto R^{\Delta}$, approaches the diffusion spectral index δ asymptotically ($\Delta \simeq \delta$).

Because of the importance of the B/C ratio to the understanding of CRs, over the last 30 years there have been a large number of (direct and indirect) measurements. Some of the recent direct measurements are listed in Table 1.1.

1.2.6 Radioactive Isotopes

The measurements of long-lived radioactive secondary nuclei with lifetimes comparable to $\tau_{\rm esc}$, such as ^{10}Be (half-life 1.39×10^6 yr) and ^{26}Al (half-life 8.7×10^5 yr) [84], are thought to be useful probes of CR propagation. The ratios of unstable to stable isotopes of these secondary nuclei provide a major constraint on CR propagation models such as the confinement time of CRs in the Galaxy [16, 85]. Among these nuclei isotopes, ^{10}Be is the longest lived and best measured. The ^{10}Be isotope is unstable, undergoing β decay into ^{10}B.

In the leaky box model, an energy-dependent escape length is defined as

$$\lambda_{\rm esc}(E) \equiv \rho\, \beta\, c\, \tau_{\rm esc}(E),$$

where ρ is the average density of the interstellar matter and $\beta \simeq 1$ for relativistic particles. As mentioned before, $\tau_{\rm esc}$ is interpreted as the average time in the containment volume, and thus $\lambda_{\rm esc}$ as the average amount of ISM traversed by CRs. The flux ratio of an unstable to a stable isotope, such as the ^{10}Be/^{9}Be raio, depends separately on the average escape time ($\tau_{\rm esc}$) and average density (ρ) [15]. Therefore, an experimental measurement of this unstable/stable ratio allows separation of these two parameters (ρ and $\tau_{\rm esc}$) in the propagation model. This measurement can be combined with the measurements of stable secondary-to-primary ratios (such as the B/C ratio) which determine the average amount of interstellar matter traversed ($\lambda_{\rm esc}$), to derive the CR confinement time in the Galaxy.

Chapter 2

Alpha Magnetic Spectrometer

2.1 AMS Detector

AMS is a general purpose high-energy particle physics detector in space with a large geometrical acceptance (effective acceptance $\sim$ 0.5 m^2 sr) [86]. As shown in Figures 2-1(a) and 2-1(b), the AMS detector consists of nine layers of precision silicon tracker [87]; a transition radiation detector (TRD) [88–90]; four planes of time of flight (TOF) scintillation counters [91, and references therein]; a permanent magnet [92, 93]; an array of 16 anticoincidence counters (ACC) [94], inside the magnet bore; a ring imaging Čerenkov detector (RICH) [95–99]; and an electromagnetic calorimeter (ECAL) [100–102]. Figure 2-1(b) also shows a 369 GeV positron event recorded by AMS. The reconstructed trajectory, or track, is shown by the red line.

AMS operates continuously on the ISS and has been monitored and controlled around the clock from the ground by the AMS Collaboration since launch. The AMS Payload Operation Control Center (POCC) is located at CERN, Geneva.

2.1.1 Definition of the Coordinate System

The timing, location, attitude, and orientation of AMS are provided by a combination of global positioning system (GPS) units affixed to AMS and to the ISS.

The AMS coordinate system is right-handed and concentric with the center of the

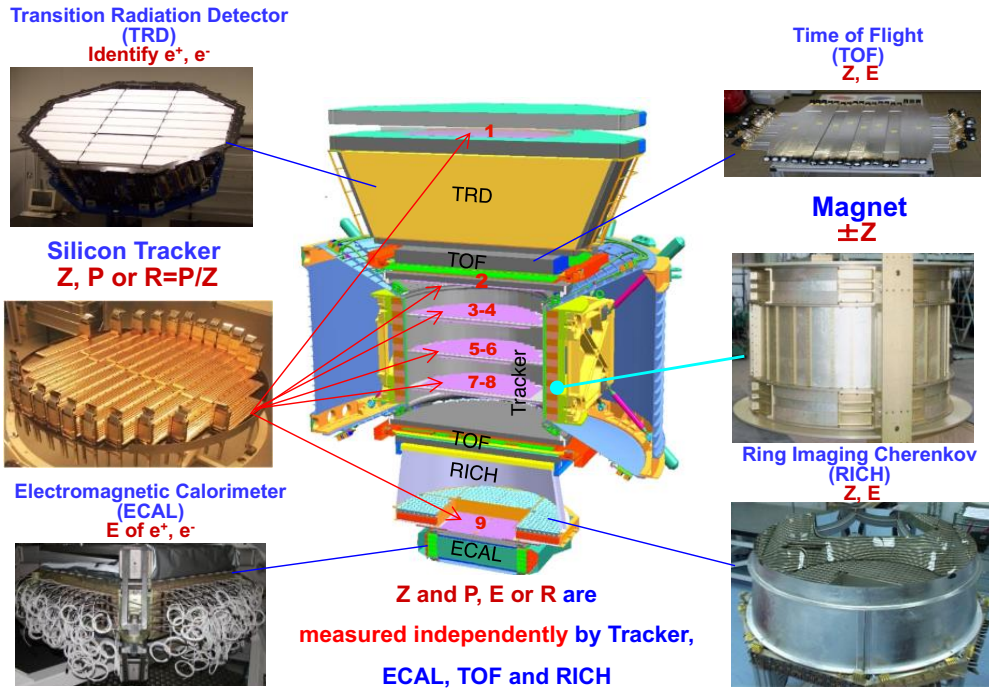

(a) The AMS detector and its different subdetectors.

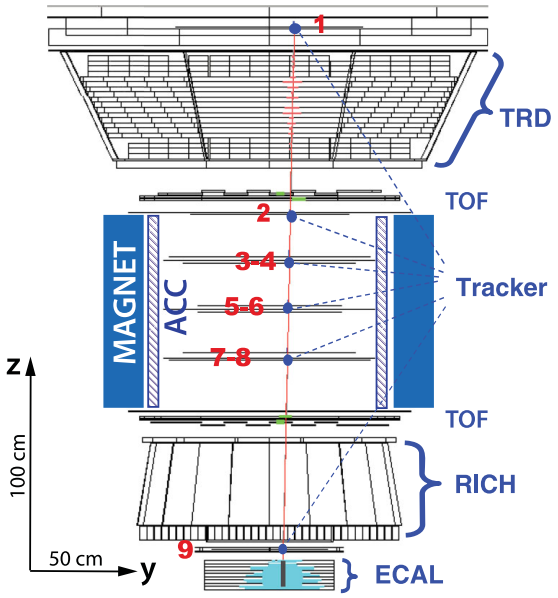

(b) A high-energy positron of 369 GeV measured by the AMS detector in the bending (y-z) plane. Taken from Ref [103].

Figure 2-1: The layout of the AMS detector.

permanent magnet. The x-axis is parallel to the main component of the magnetic field, and the z-axis points vertically upwards. The (y-z) plane is the bending plane.

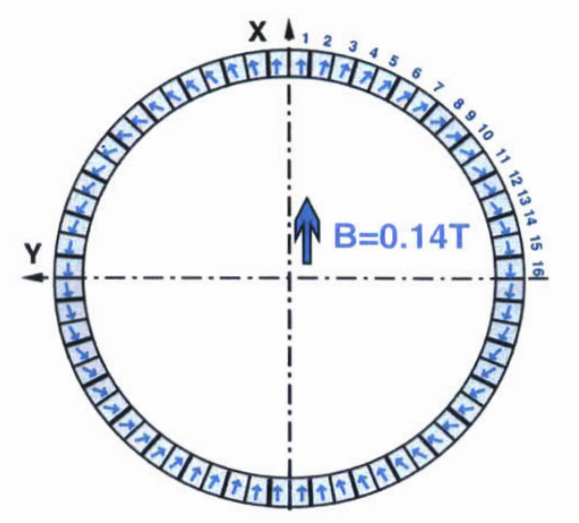

Figure 2-2: Magnetic field orientation of the AMS magnet sectors. Taken from Ref. [104].

AMS is mounted on the ISS with a 12° roll to port to avoid the ISS solar panels being in the field of view of the detector. The terms above, below, upward- and downward-going refer to the AMS coordinate system.

2.1.2 Permanent Magnet

The magnet is made of 64 sectors (each sector composed of 100 blocks) of high-grade Neodymium-Iron-Boron. These sectors are assembled in a cylindrical shell structure with a length of 0.8 m and an inner diameter of 1.1 m.

As shown in Figure 2-2, the central field of the permanent magnet is 0.14 T in the x direction, with negligible dipole moment (less than 2×10^{-2} T) outside the magnet in order to eliminate the effect of torque and electronics interference on the ISS.

Before flight, the field was measured in 120 000 locations to an accuracy of better than 2×10^{-4} T. Two detailed measurements of the magnetic field map were made, one in 1997 (before the engineering flight of AMS-01) and the other in 2010. The results show that the field did not change within 1%, limited by the accuracy of the 1997 measurement, as shown in Figure 2-3. On orbit, the temperature of the magnet varies from -3°C to $+15$°C. The magnetic field strength is corrected with a measured temperature dependence of $-0.09\%/$°C.

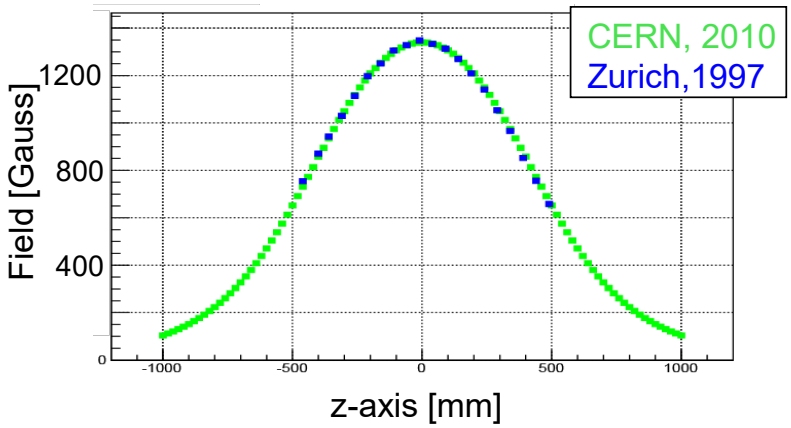

Figure 2-3: The AMS magnetic field map intensity over the z-axis measured in 1997 and 2010. $z = 0$ corresponds to the magnet center.

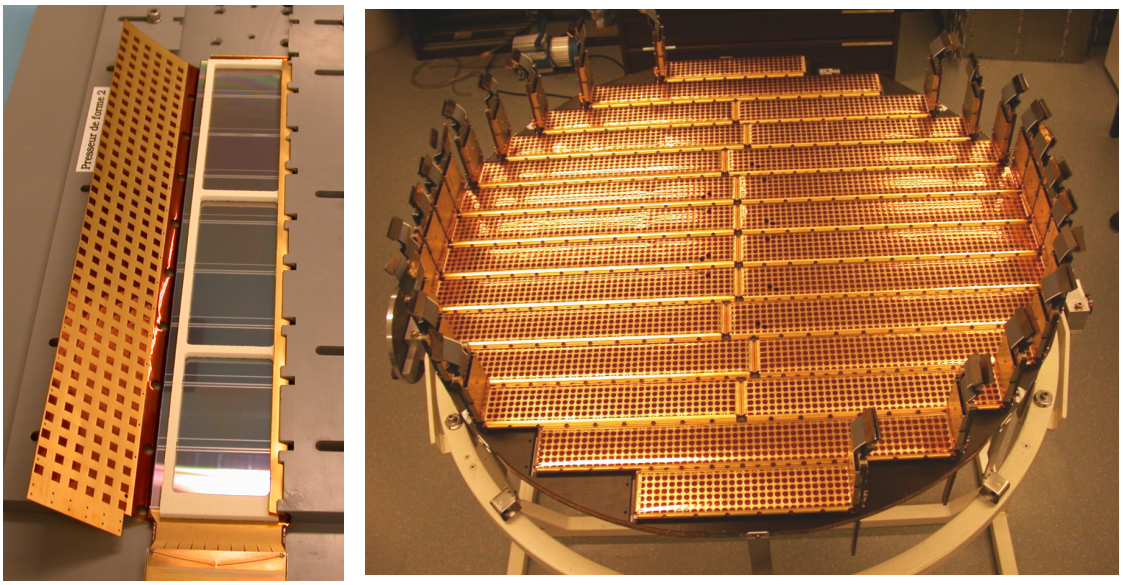

(a) Ladder p-side before the shielding.

(b) Tracker L2 assembled with 24 ladders.

Figure 2-4: Pictures of the ladder and tracker L2. Taken from Ref [105].

2.1.3 Silicon Tracker

The tracker is composed of 192 ladders, each containing double-sided microstrip silicon sensors with dimensions of $\sim 72 \times 41 \times 0.3$ mm^2, readout electronics, and mechanical support [87, 92].

The tracker has nine layers, the first (L1) at the top of the detector, the second (L2) above the permanent magnet, six (L3 to L8) within the bore of the permanent

magnet, and the last (L9) above the ECAL; see Figure 2-1. L2 to L8 constitute the Inner Tracker (ITk). L9 covers the ECAL acceptance. In the ITk, three planes of aluminum honeycomb with carbon fiber skins are equipped with one layer of silicon ladders on each side of the plane. These three planes are constituted by i) L3 and L4, ii) L5 and L6, and iii) L7 and L8, respectively, as indicated in Figure 2-1. Each layer is composed of 16 to 26 ladders and each ladder composed of 9 to 15 daisy-chained silicon sensors. A picture of a ladder and tracker plane L2 is shown in Figure 2-4(a) and 2-4(b), respectively. In total, the AMS tracker is composed of 2284 silicon sensors covering a sensitive area of 6.75 m^2.

Tiny aluminum strips running in orthogonal directions are implanted on the two sides of the 300 μm thick high-purity n-doped silicon substrate, providing a two-dimensional position measurement of charged particles. The junction side, or p-side, is composed of p^+-doped strips, for an implantation (readout) pitch of 27.5 μm (110 μm); the opposite ohmic side, or n-side, has a coarser implantation (readout) pitch of 104 μm (208 μm). The finer pitch p-side strips measure the bending (y) coordinate, while the orthogonal n-side strips measure the non-bending (x) coordinate. Figure 2-5 shows a schematic view of the double-sided microstrip silicon sensor. One expects to achieve the best spatial resolution when every single implanted strip is directly read out by the electronics. In the AMS scheme of signal collection, however, only one in every four (two) implemented strips is effectively read out on the p(n)-side of the sensor, due to the size and power consumption requirements for the payload. Under this configuration, each ladder has 640 (192) readout strips on the p(n)-side for 2568 (384) implanted strips. Capacitive coupling and charge sharing between neighbouring strips is exploited in order to achieve a 10 μm (30 μm) spatial resolution in the y (x) coordinate for singly charged ionizing particles.

The ITk is held stable by a carbon fiber structure with negligible coefficient of thermal expansion. The stability of the ITk is monitored by the Tracker Alignment System (TAS) using 20 laser beams, wavelength 1082 nm (infrared bandwidth), which penetrate layers L2 through L8 and provide submicron measurements of relative position. The geometrical stability of the ITk is important in order to maintain the best

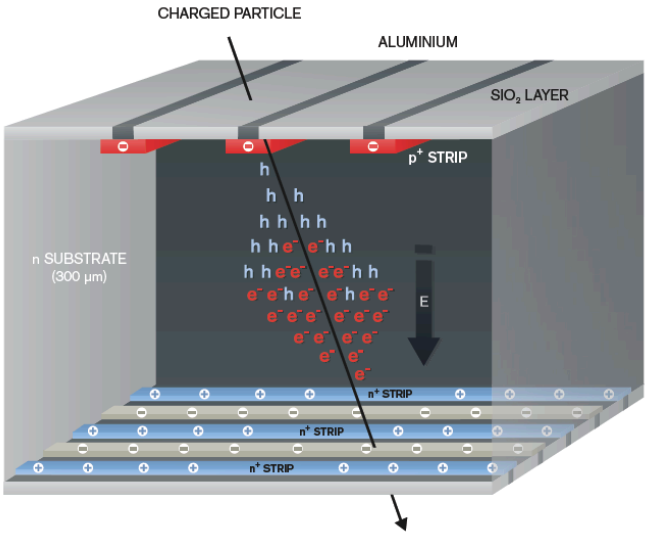

Figure 2-5: The double-sided microstrip silicon sensor and the position measurement principle. When a charged particle traverses the silicon sensor, e^--hole pairs are generated along its path. Due to the electric field in the depleted region, e^- and holes diffuse to opposite sides. Taken from Ref. [106].

performance of the rigidity measurement and charge sign determination. Dynamic alignment of outer layers is performed by using CRs (predominantly protons) in a two-minute window. The position of L1 is aligned with a precision of 5 μm with respect to the ITk and L9 with a precision of 6 μm. Details of the AMS tracker alignment are found in Ref. [107].

The tracker accurately determines the trajectory, momentum p, absolute charge $|Z|$, and charge sign of CRs by multiple measurements of the coordinates and energy loss. Together with the 0.14 T permanent magnet, the tracker measures the particle rigidity R of charged CRs with momentum p and charge Z: $R = p/Z$. Each layer of the tracker independently measures the x and y coordinates and also provides an independent measurement of the charge Z [106]. Talbe 2.1 summarizes for Z = 1, 2, 5, 6 particles 1) on average the spatial resolution in each tracker layer in the bending direction, 2) the resulting maximum detectable rigidities (MDRs) over the 3 m lever arm from L1 to L9[1], and 3) the charge resolution ($\Delta Z/Z$) of the combined

[1]With large samples of nuclei data (5 years of operation), AMS is now able to accurately account for non-linear saturation effects in the tracker electronics. This work [108] leads to a major improvement in the bending coordinate accuracy for nuclei (e.g., $\pm$5.1 μm for C and $\pm$6.3 μm for O), and therefore will increase the MDRs.

Table 2.1: The spatial resolution in each tracker layer in the bending direction, the MDR over the full lever arm from L1 to L9, and the overall charge resolution of the ITk for $Z = 1$, 2, 5, 6 particles.

CR nuclei	**Charge Z**	**Spatial resolution [μm]**	**MDR [TV]**	**Charge resolution $\Delta Z/Z$**
Proton	1	10	2	5%
Helium	2	7.5	3.2	3.5%
Boron	5	8	3	2%
Carbon	6	10	2.6	2%

ITk.

Due to the fact that the thermal environment on the ISS is constantly changing, components on the outside of AMS are subjected to temperatures ranging from $-25°$C to $+55°$C. Therefore, it is important to ensure that the components operate within their nondestructive thermal limits. AMS is equipped with a mechanically pumped two-phase CO_2 cooling loop system, called the tracker thermal control system (TTCS), to keep the ITk frontend electronics temperatures stable within 1°C to ensure its optimal performance.

2.1.4 Time of Flight Counters

The TOF counters measure the velocity ($\beta = v/c$) and $|Z|$ of CRs.

Two planes of TOF counters are located above L2 (upper TOF) and the other two planes are located below the magnet (lower TOF). Each plane contains eight or ten scintillating paddles. Each paddle is equipped with two or three photomultiplier tubes (PMTs) on each end for an efficient detection of traversing particles. Figure 2-6 shows the design of the upper TOF, lower TOF, and a TOF paddle. The coincidence of signals from all four planes provides a charged particle trigger. The anode signals from the PMTs are split into two parts: 95% of the signal goes to the time measurement unit and the rest 5% goes to the charge measurement unit. There are three thresholds for the anode signals in the time measurement unit: 1) the low threshold (LT), set at $\sim$ 20% of a minimum ionizing particle (MIP, $Z = 1$) signal, is used for time measurement; 2) the high threshold (HT), set at $\sim$ 50% of a MIP signal, is used for

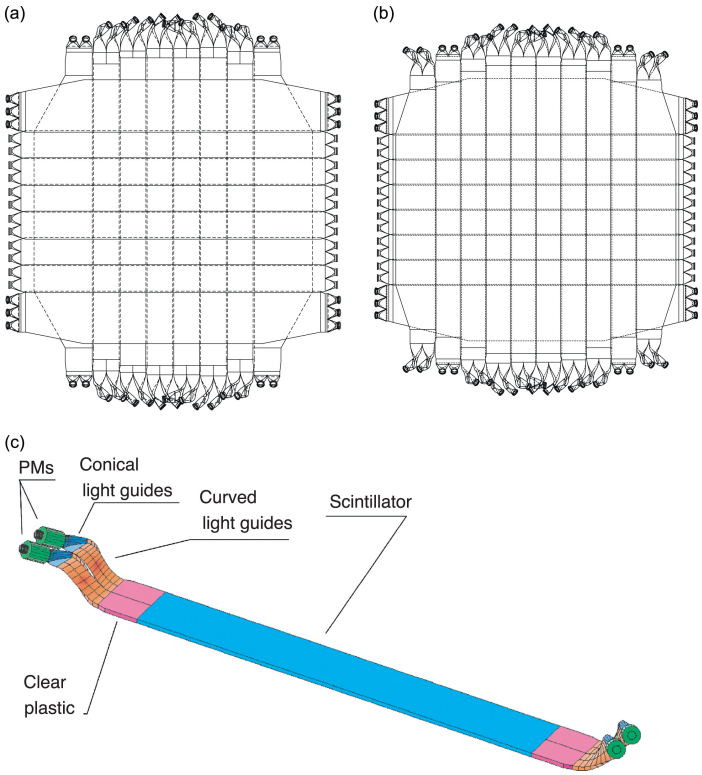

Figure 2-6: Top view of the design of the (a) upper TOF and (b) lower TOF. (c) The design of a TOF counter. The lower TOF has a larger active area than the upper TOF to increase the acceptance of charged particles deflected by the magnet. Taken from Ref. [109].

the trigger of $|Z| \geq 1$ particles; and 3) the super high threshold (SHT), set at ~ 3.5 times a MIP signal, is used for the trigger of $|Z| \geq 2$ particles.

The TOF charge resolution, obtained from multiple measurements of the ionization energy loss, is listed in Table 2.2 for $Z = 1, 2, 5, 6$ particles. Such an accuracy of the charge measurement is provided independently by 1) combining the pulse heights of the two upper planes and 2) combining the pulse heights from the two lower planes.

Table 2.2: TOF charge resolution (all 4 planes combined) for $Z = 1, 2, 5, 6$ particles.

CR nuclei	**Charge Z**	**Charge resolution $\Delta Z/Z$**
Proton	1	5%
Helium	2	4%
Boron	5	3%
Carbon	6	3%

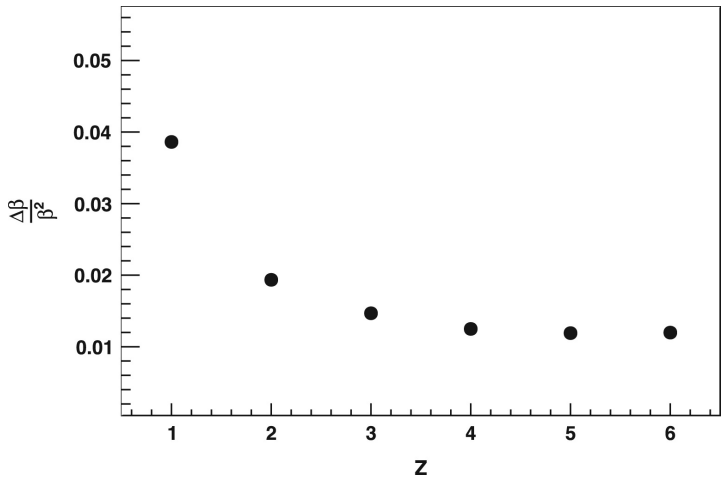

Figure 2-7: TOF velocity resolution $\Delta\beta/\beta^2$ as a function of the charge Z of CR nuclei. Taken from Ref. [109].

The average time resolution of each counter has been measured to be 160 ps, 80 ps, and 48 ps for $Z = 1, 2, 6$ particles, respectively. As shown in Figure 2-7, the overall velocity resolution of the TOF system ($\Delta\beta/\beta^2$) has been measured using in-flight data (e.g., $\Delta\beta/\beta^2 \approx 4\%, 2\%, 1\%, 1\%$ for $Z = 1, 2, 5, 6$ particles, respectively), which also discriminates between upward- and downward-going particles. The timing resolution improves with increasing magnitude of the charge to a limit of $\Delta t \sim 50$ ps and $\Delta\beta/\beta^2 \sim 1\%$ for $Z > 5$ particles.

Details of in-space calibration and performance of the TOF are found in Ref. [109].

2.1.5 Anticoincidence Counters

Particles with a large polar angle can not be measured well by AMS. One main purpose of the ACC counters is to veto undesired events with particles that enter or leave the ITk volume transversely.

The ACC counters form a cylindrical shell surrounding the ITk inside the magnet bore. As shown in Figure 2-8, the ACC consists of 16 curved scintillator panels of 0.8 m length, instrumented with wavelength-shifting fibers of 1 mm diameter to collect the ultraviolet scintillation light (wavelength $\lambda \approx 400$ nm), transform the wavelength of the light to $\lambda \approx 480$ nm, and guide the light to the PMTs [94]. For redundancy adjacent counters are combined to provide 8 readout sectors. The plastic

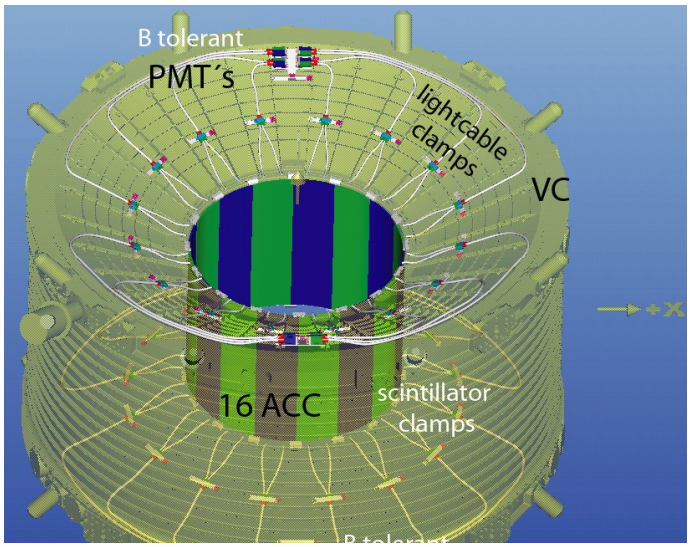

Figure 2-8: The arrangement of the ACC components.

scintillator panels are overlapping in order to maintain the hermiticity of the ACC cylinder. There is a tongue and a groove along the vertical edges of the counters such that particles crossing this area are detected simultaneously by two panels [103].

Long duration tests of the counters show the ACC has an efficiency of 99.999% to reject CRs which enter the ITk from the side.

2.1.6 Transition Radiation Detector

The TRD is designed to use 1) transition radiation to distinguish $e^{\pm}$ (signal) from protons (background) and 2) ionization energy loss dE/dx to independently identify nuclei. Transition radiation can be produced by a highly relativistic charged particle (with a large Lorentz factor, $\gamma \gtrsim 1000$) when it traverses the boundary of two materials with different dielectric constants, resulting in the emission of soft X-ray photons.

The TRD is located near the top of the AMS below tracker L1. It consists of 5248 proportional tubes of 6 mm diameter with a maximum (minimum) length of 2 m (0.8 m) arranged side by side in 16-tube modules. Figure 2-9 shows a TRD module of 16 proportional tubes. In total there are 328 modules. Since the probability of

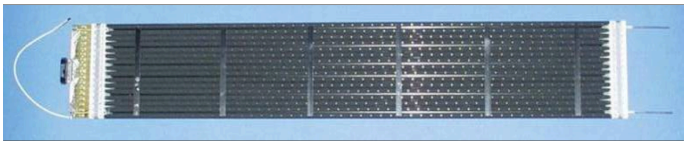

Figure 2-9: A 0.6 m long space-qualification TRD module of 16 proportional tubes.

Figure 2-10: The assembled TRD consists of 20 layers of fleece radiators and proportional tubes.

transition radiation emission increases with the number of boundaries crossed, the modules are mounted in 20 layers (see Figure 2-10) and each layer is interleaved with a 20 mm thick fiber fleece radiator (see Figure 2-11) with a density of 0.06 g/cm^3. Along the y-axis, there are 12 layers of proportional tubes located in the middle of the TRD and, along the x-axis, 4 layers located on top and 4 on the bottom. The proportional tubes are filled with a gas mixture of approximately 90:10 Xe:CO_2. Experience over the first 5 years of operations on the ISS shows, as expected, a very small, diffusion-dominated leak rate of $\sim$ 4.5 mbar/day. At launch, the onboard gas supplies contained 49 kg of Xe and 5 kg of CO_2 which ensures $\sim$ 30 years of steady TRD operations in space at the current loss rate.

In order to differentiate between $e^{\pm}$ and protons in the TRD, we combine signals from the 20 layers of proportional tubes to calculate a TRD estimator Λ_{TRD}, which is formed from the ratio of the log-likelihood probability of the $e^{\pm}$ hypothesis to that of the proton hypothesis in each layer [103, 111]. With this method, $e^{\pm}$, which have $\Lambda_{\mathrm{TRD}} \sim 0.5$, are efficiently separated from protons, which have $\Lambda_{\mathrm{TRD}} \sim 1$ [111]. This

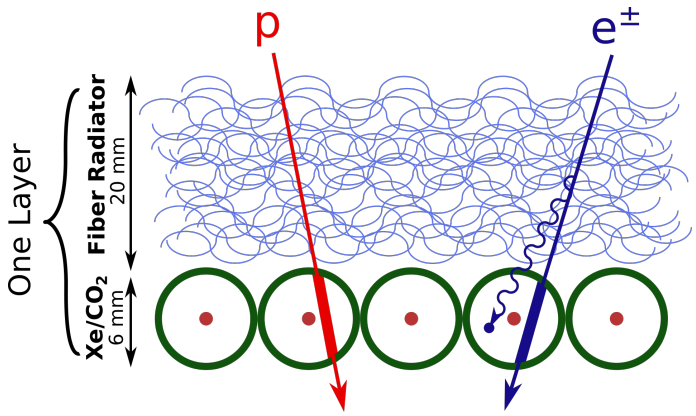

Figure 2-11: Diagram of one TRD layer and the TRD measurement principle. Taken from Ref. [110].

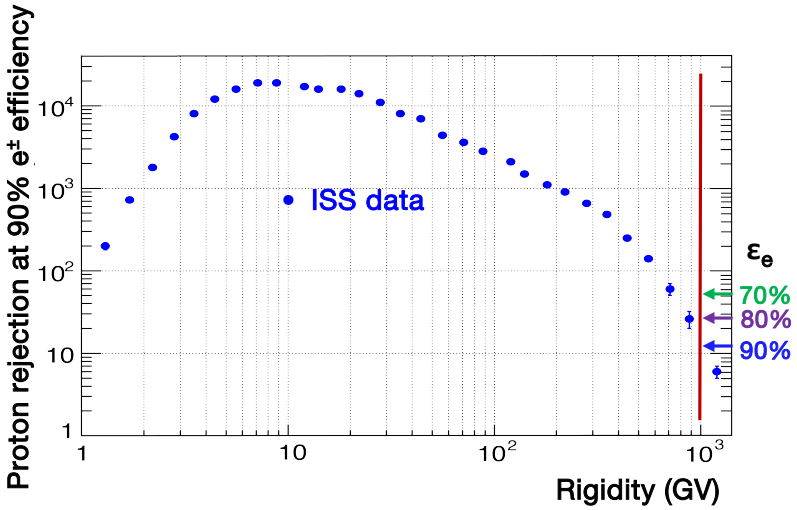

Figure 2-12: The TRD proton rejection power as a function of rigidity at 90% selection efficiency for $e^{\pm}$. At 10^3 GV, the proton rejection factors at 70%, 80%, and 90% $e^{\pm}$ efficiency are shown and indicated by the arrows.

discrimination ability can be quantified by the proton rejection power, defined as the number of protons which are rejected before a proton is misidentified as an electron or positron. On orbit, the proton rejection power of the TRD estimator at 90% $e^{\pm}$ selection efficiency has been measured to be 10^3–10^4 [103], as shown in Figure 2-12.

2.1.7 Ring Imaging Čerenkov Detector

The RICH is designed to measure the magnitude of the charge Z of CRs and their velocities with an accuracy of $\Delta\beta/\beta \sim \mathcal{O}(0.1\%)$.

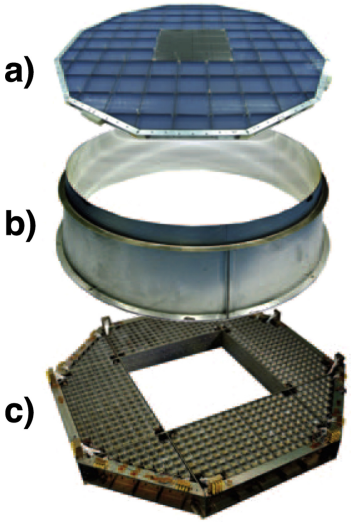

Figure 2-13: Components of the RICH: (a) the radiators, (b) the expansion volume and reflector, and (c) the photodetection plane. Taken from Ref. [112].

It consists of two nonoverlapping dielectric radiators, an expansion volume, and a photodetection plane, as shown in Figure 2-13. When a charged particle traverses the dielectric radiators with a velocity greater than the velocity of light in the material, $\beta > 1/n$ where n is the radiator refractive index, a cone of light is emitted. This process is called the Čerenkov effect. The Čerenkov photons are emitted along a characteristic cone whose angular aperture θ_a is directly related to the particle velocity and the refractive index of the material, $\cos\frac{\theta_a}{2} = 1/(n\beta)$. Thus, the opening angle of the Čerenkov radiation cone provides a measure of the velocity of the incoming charged particle. Figure 2-14 shows the velocity resolution $\Delta\beta/\beta$ of the RICH as a function of the particle charge Z.

The central radiator is formed by 16 sodium fluoride (NaF) tiles, each $85 \times 85 \times 5$ mm^3, with a refractive index of $n = 1.33$ corresponding to a Čerenkov threshold of $\beta > 0.75$. The NaF radiator is surrounded by a radiator consisting of 92 silica aerogel tiles, each $115 \times 115 \times 25$ mm^3, with $n = 1.05$ corresponding to a threshold of $\beta > 0.953$.

The expansion volume has a dimension along the z-axis of 470 mm. To reduce lateral losses and increase detection efficiency, the expansion volume is surrounded by a high reflectivity mirror with the shape of a truncated cone.

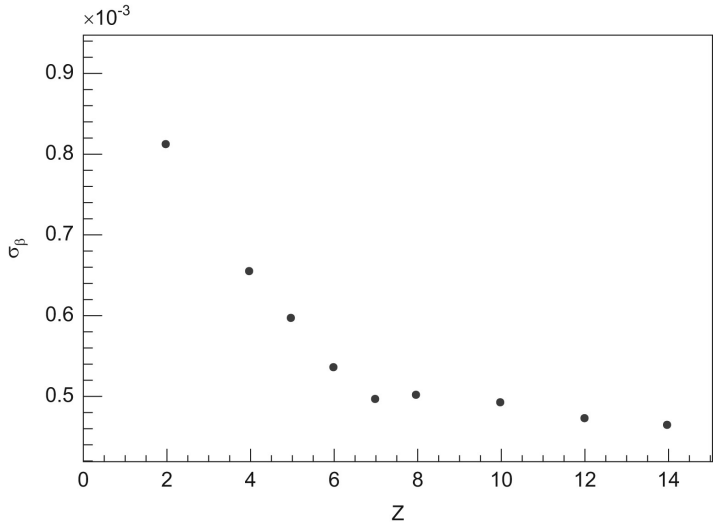

Figure 2-14: RICH velocity resolution as a function of the charge Z of CR nuclei. Taken from Ref. [95].

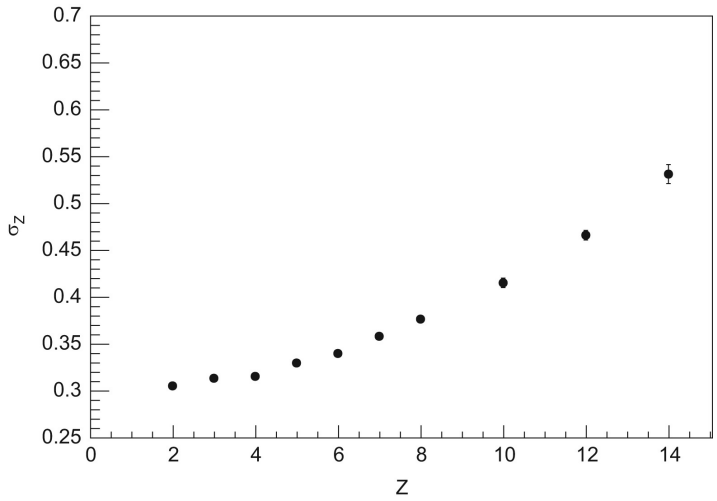

Figure 2-15: RICH charge resolution as a function of the charge Z of CR nuclei. Taken from Ref. [95].

The photodetection plane is a set of 680 multianode PMTs with 4×4 anodes each (an array of 10 880 photosensors in total) coupled to plastic light guides with an effective spatial granularity of 8.5×8.5 mm^2. Photon counting within a Čerenkov ring provides a measurement of the particle charge Z. The sum of the signal amplitudes is proportional to Z^2. Figure 2-15 shows the charge resolution $\Delta Z/Z$ for $1 \geq Z \leq 8$ particles.

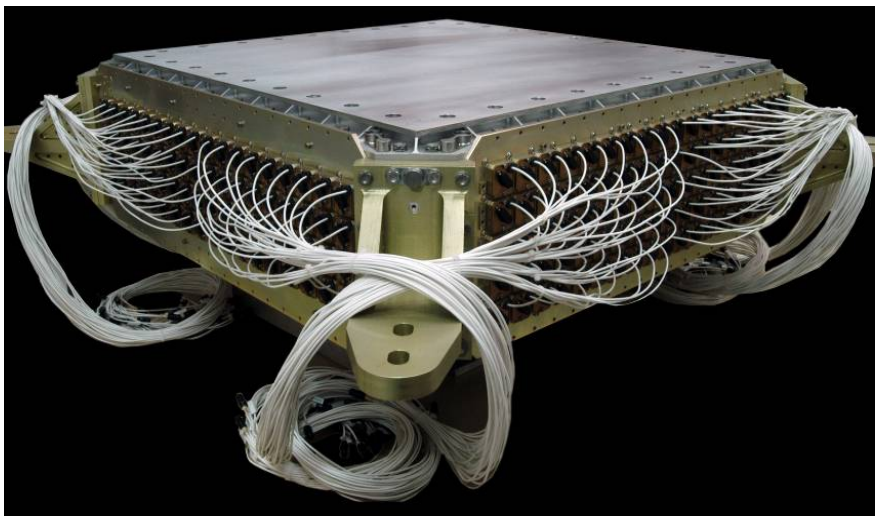

Figure 2-16: A photo of the completed ECAL before installed on AMS.

2.1.8 Electromagnetic Calorimeter

The ECAL measures the 3D shower profile and the electromagnetic shower energy. It separates $e^{\pm}$ from protons independently from the TRD by exploiting the different characteristic profiles of electromagnetic and hadronic showers.

The ECAL is a sampling calorimeter with 17 radiation length (X_0) and consists of a multilayer sandwich of 98 lead foils and 50 000 scintillating fibers [100–102]. It has an active area of 648×648 mm^2 and a thickness of 166.5 mm and is composed of nine *superlayers* along the z-axis. Each superlayer is 18.5 mm thick and made of 11 grooved, 1 mm thick lead foils interleaved with ten layers of 1 mm diameter scintillating fibers glued to the foils (the last foil of the last superlayer is made of aluminum), corresponding to 1.9 X_0. In each superlayer, the fibers run in one direction only. The 3D imaging capability of the ECAL is obtained by stacking superlayers with fibers oriented in alternating directions (five superlayers with fibers parallel to the x-axis and four parallel to the y-axis). The fibers are read out on one end by 1296 photosensors (324 PMTs each with 2×2 pixels) with a linearity of $1/10^5$ per sensor. A picture of the assembled ECAL is shown in Figure 2-16.

Signals from the 17 X_0 ECAL are scaled to the top of AMS to provide an accurate measurement of the incoming energy E of $e^{\pm}$. From the beam tests of the

complete AMS detector, the energy resolution of the ECAL has been measured and parametrized as a function of energy E (in GeV) [111]

$$\frac{\sigma(E)}{E} = \sqrt{\frac{(0.104)^2}{E} + (0.014)^2}.$$

In order to cleanly identify $e^{\pm}$ in the ECAL, a multivariate classifier, based on a boosted decision tree algorithm (BDT) [113–115], is constructed by using the 3D shower shape in the ECAL. This is used to further differentiate between $e^{\pm}$ and protons independently from the TRD.

2.1.9 Trigger and Data Acquisition

The AMS trigger is generated by the signals coming from the TOF, ACC and ECAL.

Three types of fast triggers are designed for different particles: 1) the FTC for charged particles, 2) the FTZ for slow and heavy charged particles (like strangelets), and 3) the FTE for neutral particles detected in ECAL (producing electromagnetic showers). These three triggers are combined by a logical OR to produce a general fast trigger (FT). After the FT is generated, a dedicated electronics board named JLV1 starts analyzing different trigger signals and enters the Level-1 logic evaluation.

Seven sub-triggers (five physics-related triggers and two unbiased triggers) were designed and implemented for data taking onboard the ISS:

(1) **single charged**: 4 out of 4 TOF planes above HT in coincidence together with an absence of signals from the ACC;

(2) **normal ions**: 4 out of 4 TOF plane above SHT in coincidence together with less than 5 signals from the ACC;

(3) **unbiased charged**: 3 out of the 4 TOF layers above HT in coincidence, prescaled by a factor of 100 to reduce the trigger rate;

(4) **slow ions**: similar to normal ions but with extended gate width to latch the signals, as a dedicated trigger for detecting potential strangelets;

(5) **electrons**: 4 out of 4 TOF planes above HT in coincidence together with both x- and y-projections of ECAL energy deposition above threshold.

(6) **photons**: both x- and y-projections of ECAL energy deposition above threshold together with the ECAL shower angle inside the detector geometrical acceptance.

(7) **unbiased EM**: ECAL signal above threshold, prescaled by a factor of 1000 to reduce the trigger rate.

Triggers (1)–(3) are the most important in the measurements of CR light nuclei ($2 \leq Z \leq 8$) fluxes. Details are described below using $Z = 2$ events as an example.

Helium traversing the AMS are triggered and flagged by the logical OR of any of three trigger conditions onboard the ISS, i.e., (i) OR (ii) OR (iii) [116] as follows:

(i) the coincidence, within 240 ns, of signals from all 4 TOF planes each with a pulse height above the HT together with an absence of signals from the ACC;

(ii) the coincidence, within 240 ns, of signals from all 4 TOF planes each with a pulse height above the SHT together with signals from no more than 4 out of the 8 ACC sectors;

(iii) the coincidence, within 240 ns, of signals from 3 out of the 4 TOF planes each with a pulse height above the HT and with no ACC requirement.

To reduce the trigger rate, condition (iii) is prescaled to 1%; i.e., only 1 event out of 100 which meet these conditions is passed on to the logic OR. The efficiency of trigger (iii) is estimated directly from the data using events in which 1 of the 4 TOF layers gives no signal. It is above 99.99% for $Z = 2$ events in the rigidity range of 1.9 GV to 3 TV. This allows the estimation of the efficiency of each TOF layer and, consequently, the efficiency of trigger (iii). Most importantly, trigger (iii) can be used to measure the efficiency of triggers (i) and (ii). Together, requiring triggers (i) and (ii), hereafter called *physics trigger*, ensures a high efficiency of detecting CR ions with AMS, while effectively rejecting CR events which enter the ITk from the side. The efficiency of the physics trigger in the carbon flux measurement is calculated in Chapter 3.

Onboard data processing reduces the raw data volume by a factor of 1000 without any physics information loss. The collected data are downlinked from the ISS to the ground at an average rate of 10 Mbit/s. Whenever the data are sent to the ground,

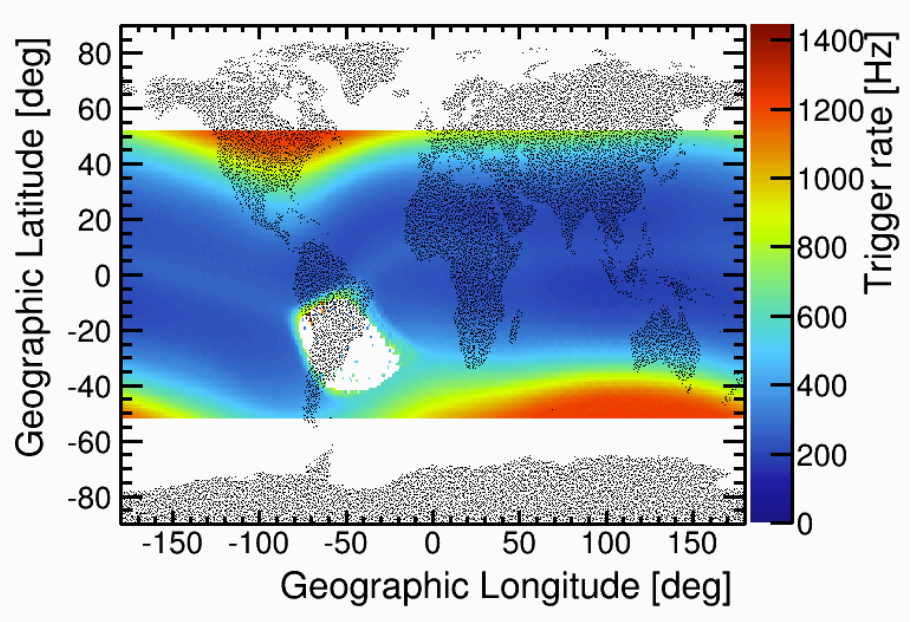

Figure 2-17: The AMS trigger rate as a function of the orbital position (in geographic latitude and longitude coordinates). Taken from Ref. [117].

they are also recorded in the AMS laptop onboard the ISS. The AMS laptop has a hard drive of 750 GB which can store up to about 6 days worth of AMS data, allowing one to retrieve the data lost on transmission to the ground. On the ISS, the CR particle rates in the detector acceptance vary from $\sim$ 200 Hz near the Equator to $\sim$ 2000 Hz near Earth's magnetic poles, as shown in Figure 2-17. The data acquisition (DAQ) efficiency of AMS is 86% on average, resulting in an average event acquisition rate of $\sim$ 600 Hz.

In Figure 2-17, there is a region, called South Atlantic Anomaly (SAA) [118], over the South Atlantic Ocean centered near the east coast of Brazil, where the Earth's magnetic field strength is the weakest (see Figure 2-18). This is due to the non-concentricity of the Earth and its magnetic dipole and the misalignment between the Earth's magnetic axis and rotation axis. This asymmetry leads to the inner Van Allen belt reaching low enough (200 km altitude) for AMS to pass through. In the SAA, the number of low-energy charged particles increases by at least two orders of magnitude [119], resulting in orbiting aircrafts and satellites exposed to a higher level of radiation. This also causes the *live time* of AMS, which is defined as the fraction

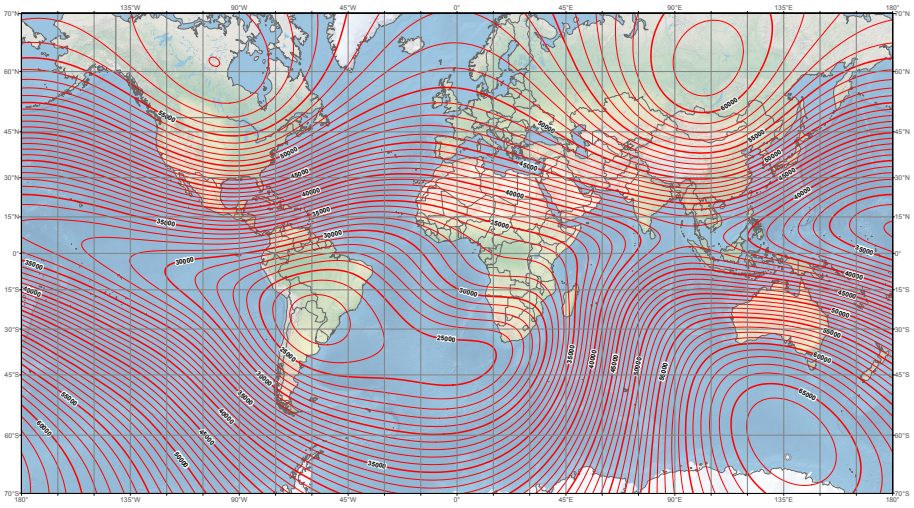

Figure 2-18: Contour map for the total intensity of the geomagnetic field [120] at the Earth's surface. Contour interval: 1000 nT.

of each second that AMS is ready to trigger (i.e., to record a new event), to drop to zero. Therefore, in the data analysis it is required that the ISS was outside of the SAA. The SAA effect can be effectively reduced by applying selection cuts on the orbital position (in latitude and longitude) and on the live time (live time > 0.5). This preserves most events collected in the geomagnetic polar regions where the live time decreases to about 0.8.

2.2 Data Corrections and Monte Carlo Simulation

Before launch, AMS was extensively calibrated at the CERN SPS. In the beam test, AMS was exposed to secondary beams of e^+ and e^- from 10 to 290 GeV, primary beams of protons at 180 and 400 GeV, and beams of $\pi^\pm$ from 10 to 290 GeV which produce transition radiation equivalent to protons up to 1.2 TeV. These test beam data have a crucial role in the data reconstruction and analysis, allowing the optimization of all reconstruction algorithms, the definition and verification of the absolute energy scale of the ECAL and the absolute rigidity scale of the tracker, and the high-precision determination of the tracker rigidity resolution function.

By using specific collected samples of CR particles, predominantly protons, several

corrections are applied to the in-flight data to ensure long-term stability of the absolute scales in the constantly varying thermal environment on orbit. These corrections include: 1) offline calibrations of the amplitude response (e.g., pedestal and noise values) of TRD, TOF, tracker, and ECAL electronic channels, which are performed four times during a $\sim$ 90 min orbit; 2) onboard calibrations of all channels to ensure the stability of the electronics response, which is performed every half-orbit ($\sim$ 46 min); 3) the alignment of the outer tracker layers (L1 and L9), which is performed every two minutes; 4) the alignment of all the other AMS detectors; and 5) the temperature correction of the magnetic field strength.

Monte Carlo (MC) simulation is a fundamental and necessary tool to understand and evaluate the detector responses based on Monte Carlo methods.

The AMS collaboration developed a dedicated program based on the GEANT-4.10.1 package [121, 122], which simulates physics processes and detector signals, to produce MC simulated events. The program simulates electromagnetic and hadronic interactions of particles in the material of AMS and generates detector responses. The Glauber-Gribov model [121,122] adjusted using the AMS helium data, see Figure 1(a) and (b) in the Supplemental Material of Ref. [116], was used for the description of the inelastic cross-sections. The INCL++ package [123, 124] was used to model nucleus-nucleus inelastic interactions below 5 GeV/n and the DPMJET-II.5 package [125] was used at higher energies. The nucleus-nucleus hadronic elastic and quasielastic scatterings were treated using the model developed for helium nuclei [116], in which the measurements from Ref. [126] were used. The MC predictions of the interactions and scatterings are validated by detailed comparisons between data and simulation (see Chapter 3). In the MC simulation, signals (including those of the AMS trigger) are digitized precisely according to the measured characteristics of the electronics and then undergo the same reconstruction algorithms as used for the data.

Chapter 3

Measurement of the Carbon and Oxygen Fluxes and their Ratio

Carbon and oxygen together with protons and helium are the most abundant nuclei in CRs. They are called primary CRs and are both thought to be mainly produced in, and accelerated by, astrophysical sources (e.g., SNRs). Precise knowledge of the their spectra in the GV–TV rigidity region provides important insights to the origin, acceleration, and subsequent propagation processes of galactic CRs [12, 59, 127, 128]. Previously, precision measurements of the proton [129] and helium spectra as well as the proton to helium flux (p/He) ratio [116] with AMS have been reported. At high rigidities, the carbon to oxygen flux (C/O) ratio directly measures the relative production and acceleration properties of carbon and oxygen. As with the B/C ratio reported by AMS [83], at low rigidities the C/O ratio also measures the average amount of ISM traversed by CRs, because a fraction of carbon nuclei (13% of its total flux at 10 GV and 3% at 2 TV) are expected to be produced by collisions of heavier nuclei in CRs, such as oxygen and nitrogen, with the ISM.

In this chapter, a cut-based analysis of the carbon flux in CRs is discussed. This procedure can be used in the measurements of other light nuclei fluxes. The description concentrates on the carbon flux analysis; the oxygen flux is obtained in an analogous procedure.

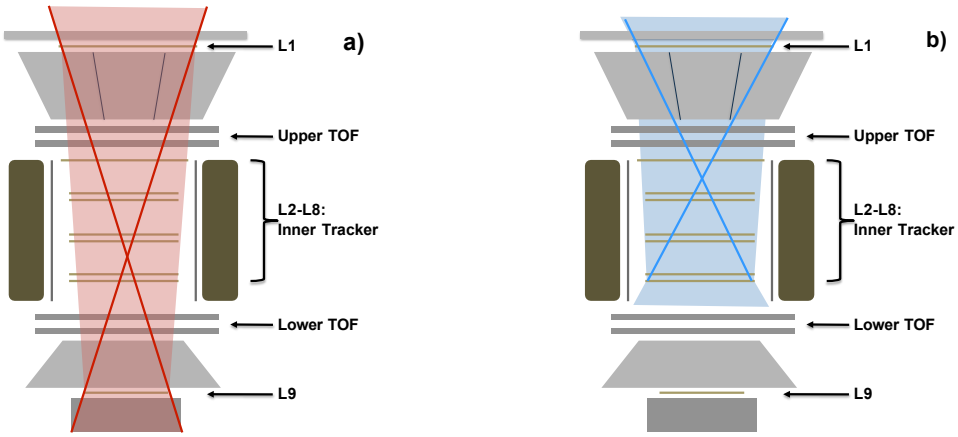

Figure 3-1: Schematic view of the geometric acceptance of a) FS (red shaded area) and b) IL1 (blue shaded area) analysis.

3.1 Event Selection and Data Samples

In the first 5 years AMS has collected 8.5×10^{10} CR events. The effective data collection time, or exposure time, used in this analysis includes only those during which the detector was in normal operating conditions and, in addition, the AMS z-axis was pointing within 40° of the local zenith, the data acquisition live time exceeded 50% (compared to its typical value of 90%), and the ISS was not in the SAA (as explained in Section 2.2).

Particles are required to be downward going and to have a reconstructed track in the ITk. In order to maximize the accuracy of the track reconstruction and to have the best resolution at the highest rigidities, further selections are made by requiring the track to pass through L1 and L9 and to satisfy additional track fitting quality criteria such as $\chi^2/\text{d.f.} < 10$ in the bending coordinate. In Section 3.4.1, we will discuss an analysis in the range of $R < 0.88$ TV which does not require the track to pass through L9. The analysis requiring the track to pass through L1 is hereafter referred to as *Inner L1 (IL1) analysis* (described in Section 3.4.1), while the one requiring both L1 and L9 is hereafter referred to as *Full Span (FS) analysis* (described in this section). Figure 3-1 shows a schematic view of the geometric acceptances of these two analyses.

The measured rigidity is required to be greater than a factor of 1.2 times the

maximum geomagnetic cutoff rigidity $R_c^{\max}$ within the AMS field of view. The field of view was restricted to 30° with respect to the detector axis due to the requirement of tracks passing through L1. The cutoff was calculated by backtracing [130] particles from the top of AMS out to 50 Earth's radii using the most recent geomagnetic model from International Geomagnetic Reference Field (IGRF) [131,132]. The safety factor of 1.2 was used to cover the uncertainties of the geomagnetic model, ensuring no residual contamination of particles which are trapped or have interacted with the Earth's atmosphere. An approximation of the cutoff rigidity is the Stömer approximation for a dipole field, in which R_c can be expressed as [133]

$$R_c = \frac{M \cos^4 \lambda}{r^2 \left(1 \pm \sqrt{1 - \sin\epsilon \sin\xi \cos^3 \lambda}\right)^2}, \tag{3.1}$$

where M is the magnitude of geomagnetic field dipole moment, λ is the latitude from the magnetic equator, ϵ is the zenith angle of the incident particle, ξ is the azimuthal angle to the north magnetic pole, r is the distance from the dipole center, and the $\pm$ sign refers to the particle charge sign. For vertically incident ($\epsilon = 0$) particles with positive charge sign, Eq. (3.1) reduces to $R_{cv} = M \cos^4 \lambda/(2r)^2$.

Charge measurements on the tracker L1, ITk, upper TOF, lower TOF, and tracker L9 are required to be compatible with charge $Z = 6$ for carbon and $Z = 8$ for oxygen, as shown in Figure 3-2 for the ITk. This selection of ITk charge yields purities of 99% for both carbon and oxygen. The charge measurement in each layer of the tracker is calibrated to be independent of rigidity using the method developed in Ref. [106].

The event selection used in this analysis is summarized as follows:

1) **Inner Tracker (L2 to L8)**

   1.1) at least five hits in the y coordinate, and, in addition, among these five hits, there is at least one hit on L2 and each of the three ITk planes, which is denoted as L2&(L3|L4)&(L5|L6)&(L7|L8);

   1.2) track fitting quality $\chi^2_{y,\,\text{inner}}/\text{d.f.} < 10$;

   1.3) consistency of the charge measurement $Z - 0.45 < Z_{\text{L2 to L8}} < Z + 0.45$,

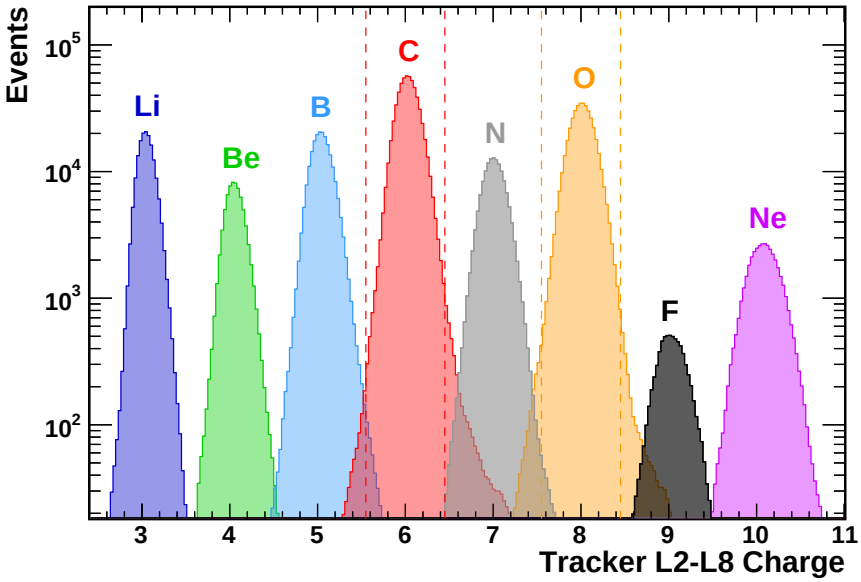

Figure 3-2: Distribution of the charge measured with the ITk (truncated mean of L2–L8 charge measurements) for samples from $Z = 3$ to $Z = 10$ selected by the combined charge measured with L1, the upper TOF, and the lower TOF over the rigidity range from 4 GV to 10 GV. The red vertical dashed lines correspond to the charge selection in the ITk for carbon and the orange dashed lines for oxygen.

and the RMS of the six (L2–L8) independent charge measurements less than 0.55 ($\mathrm{RMS}_{\mathrm{ITk\ Q}} < 0.55$).

Figure 3-3 shows the rigidity dependence of the charge measured by the ITk for carbon events selected by L1, the upper TOF, and the lower TOF, together with the charge selections applied on the ITk.

2) **Tracker L1 and L9**

2.1) tracker L1 hit (associated to the track) with well reconstructed clusters on both x and y coordinates and $Z - 0.46 - (Z-3) \times 0.16 < Z_{\mathrm{L1}}$;

2.2) purity cut (applied to the data only, not to the simulation):

$$Z_{\mathrm{L1}} < \begin{cases} Z + 0.65, & \text{for } Z \leq 5, \\ Z + 0.65 + (Z-5) \times 0.03, & \text{for } Z \geq 6; \end{cases}$$

2.3) tracker L9 hit (associated to the track) with clusters reconstructed on both x and y coordinates and $Z - 0.5 < Z_{\mathrm{L9}} < Z + 1.5 + (Z-3) \times 0.06$;

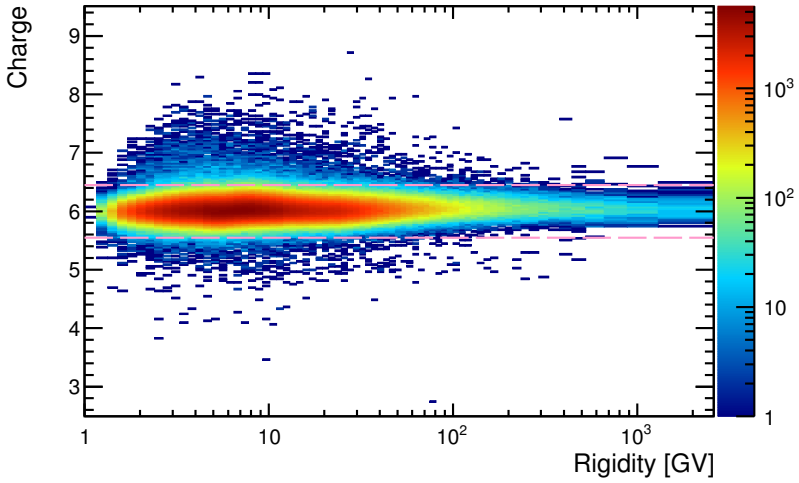

Figure 3-3: Rigidity dependence of the charge measured by the ITk for carbon events selected by L1, the upper TOF, and the lower TOF. The charge selections applied on the ITk are shown as horizontal dashed lines.

2.4) FS track fitting quality $\chi^2_{y,\,\mathrm{FS}}/\mathrm{d.f.} < 10$;

The selection ranges of L1 and L9 charge are chosen according to their charge resolution as a function of the nuclei charge Z. L1 selection criteria take into account the geometrical inefficiencies due to e.g., the gaps between silicon sensors and silicon ladders and potential dead areas in the silicon caused by malfunctioning electronics, by requiring the clusters possessing a good status of reconstruction. The requirement of Y-side hits ensures a good rigidity reconstruction; the requirement of X-side hits is needed due to the intrinsically better charge identification of the n-side strips.

Figures 3-4 and 3-5 show the rigidity dependence of the charge measured by L1 and L9, respectively, for carbon events selected by the ITk, together with the charge selections applied on L1 and L9.

3) **TOF**

3.1) β object is built using TOF signals plus tracker track information;

3.2) $\beta_{\mathrm{TOF}} > 0.4$ (particles should be downward going);

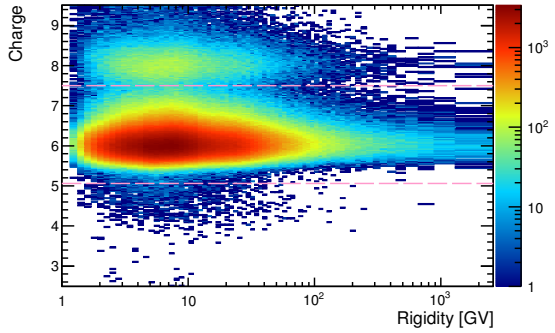

Figure 3-4: Rigidity dependence of the charge measured by L1 for carbon events selected by the ITk. The charge selections applied on L1 are shown as horizontal dashed lines.

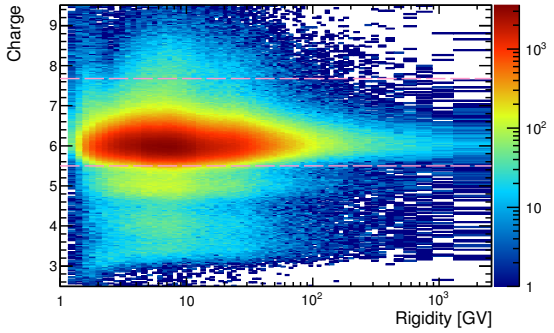

Figure 3-5: Rigidity dependence of the charge measured by L9 for carbon events selected by the ITk and L1. The charge selections applied on L9 are shown as horizontal dashed lines.

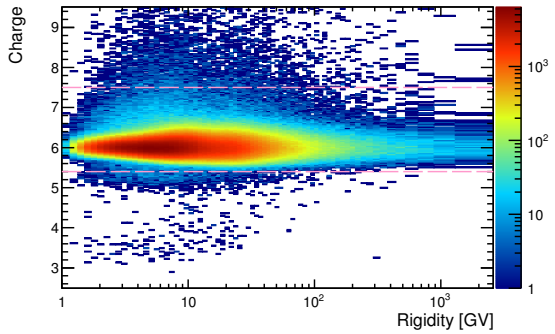

Figure 3-6: Rigidity dependence of the charge measured by the upper TOF for carbon events selected by the ITk, L1, and L9. The charge selections applied on the upper TOF are shown as horizontal dashed lines.

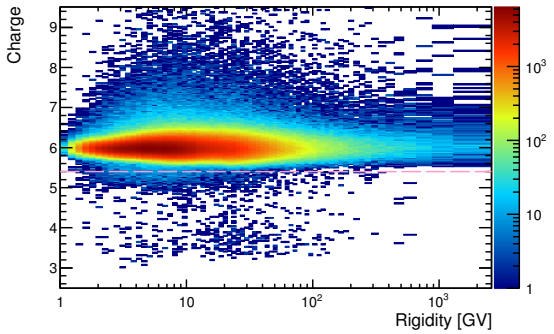

Figure 3-7: Rigidity dependence of the charge measured by the lower TOF for carbon events selected by the ITk, L1, and L9. The charge selection (only the lower limit) applied on the lower TOF is shown as horizontal dashed lines.

3.3) $Z - 0.6 < Z_{\text{upper TOF}} < Z + 1.5$;

3.4) $Z - 0.6 < Z_{\text{lower TOF}}$.

Figures 3-6 and 3-7 show the rigidity dependence of the charge measured by the upper TOF and lower TOF, respectively, for carbon events selected by the ITk, L1, and L9, together with the charge selections applied on the upper TOF and lower TOF.

4) **Physics Trigger** (see Section 2.1.9)

5) **Orbital Cuts**

5.1) AMS not in the SAA;

5.2) $R > 1.2 \times R_{\mathrm{c}}^{\mathrm{max}}$ within 30° field of view;

5.3) selection of good seconds in data collection time (see Section 3.2.1).

3.2 Flux Determination

The carbon and oxygen fluxes are determined in rigidity bins as measured with the tracker. Assuming the CR flux above the geomagnetic cutoff is isotropic (which only concerns the acceptance), the differential flux for nuclei of charge Z in the ith rigidity bin $(R_i,\ R_i + \Delta R_i)$, Φ_i^Z, is given by

$$\Phi_i^Z = \frac{N_i^Z}{A_i^Z\, \epsilon_{\mathrm{trg},i}^Z\, T_i\, \Delta R_i}, \tag{3.2}$$

where N_i^Z is the number of events of charge Z corrected for bin-to-bin migrations, A_i^Z is the effective acceptance, $\epsilon_{\mathrm{trg},i}^Z$ is the trigger efficiency, and T_i is the collection time. The determination of all ingredients is detailed in the following subsections. In this thesis, the carbon flux was measured in 67 bins, $i = 1$ to 67, from 1.9 GV to 2.6 TV, and the oxygen flux was measured in 66 bins from 2.2 GV to 2.6 TV with bin widths chosen according to the tracker rigidity resolution. The detailed definition of the bins is tabulated in Table A.1 in Appendix A.2. Since the measurement is binned, the exposure time is set constant in each rigidity bin. Therefore, for self-consistency we selected particles above $R_{\mathrm{c}}^{\mathrm{max}}$ not according to the measured rigidities but according to the lower edge of the bin they fell into. For a particle with rigidity R belonging to the ith rigidity bin $[R_i^{\mathrm{lo}},\ R_i^{\mathrm{up}})$, it was required in the flux analysis that $R_i^{\mathrm{lo}} > 1.2 \times R_{\mathrm{c}}^{\mathrm{max}}$. This requirement is more conservative (since $R \geq R_i^{\mathrm{lo}}$) and is referred to as *bin cutoff selection* in this flux analysis.

3.2.1 Data Collection Time

The exposure time is the effective amount of time that the detector was not busy with the electronics readout and consequently ready to start DAQ and trigger on an incoming event at a given rigidity. This is affected by the detector's average live time and the requirement of rigidity above geomagnetic cutoff, which introduces a rigidity dependence of the exposure time. The exposure time is calculated on a second-by-second basis using the Real Time Information (RTI) database in the AMS Offline Software, which stores the orbital and relevant DAQ information for each second of AMS data collection time on the ISS. A set of standard selection criteria has been studied by the AMS collaboration to remove bad seconds during data acquisition, as follows:

1) the ratio of the number of triggered events ($N_{\rm trig}$) over number of reconstructed events ($N_{\rm evt}$) greater than 0.98 ($N_{\rm trig}/N_{\rm evt} > 0.98$);
2) the data acquisition live time greater than 0.5;
3) the AMS z-axis pointing within 40° of the local zenith;
4) the ratio of the number of absent events ($N_{\rm err}$) over $N_{\rm evt}$ less than 0.1 ($N_{\rm err}/N_{\rm evt} < 0.1$);
5) the number of reconstructed particles ($N_{\rm par}$) greater than 0 and $N_{\rm evt} < 1800$;
6) $\dfrac{N_{\rm par}}{N_{\rm trig}} > \dfrac{0.07}{1600} \times N_{\rm trig}$ and $\dfrac{N_{\rm par}}{N_{\rm trig}} < 0.25$.

This set of cuts removes seconds when DAQ was close to saturation (e.g., in the SAA region) or when anomalous high trigger rates were observed but no or very few particles were reconstructed (e.g., in the polar regions).

Each second of the data collection was integrated to the total exposure time only in the rigidity bins where the bin cutoff selection and the good seconds selection were fulfilled. For each second the effective exposure time $\alpha(t)$ is the weighted live time l_f of the detector: $\alpha(t) = l_f \cdot N_{\rm evt}/(N_{\rm evt} + N_{\rm err})$. In the time period from t_0 to t_1, the exposure time in the ith rigidity bin is given by

$$T_i = \sum_{t=t_0}^{t_1} \alpha(t)\, \theta(t, R_i^{\rm lo}),$$

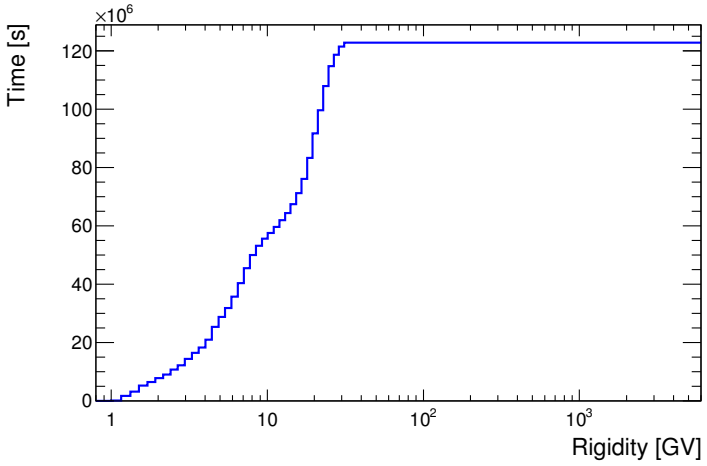

Figure 3-8: The AMS data collection time as a function of rigidity.

where $\theta(t, R_i^{\text{lo}})$ is a time-dependent function which takes the value 1 (0) for each second if passing (failing) the bin cutoff selection.

The rigidity dependence of the data collection time in the first 5 years is shown in Figure 3-8. Because of the influence of the geomagnetic field, this collection time for galactic CRs increases with increasing rigidity and becomes constant at 1.23×10^8 s above 30 GV.

3.2.2 Effective Acceptance

The normalization of the measured number of nuclei with charge Z (N_i^Z) to the flux (Φ_i^Z) is determined by the effective acceptance. The effective acceptances A_i^Z are calculated using MC simulation and then corrected for small differences δ between the data and MC simulated events related to a) the event reconstruction and selection, namely, in the efficiencies of the selection criteria (except the purity cut and orbital cuts) summarized in Section 3.1 and b) the inelastic interactions in the AMS materials.

The effective acceptance A^Z is the product of the geometric acceptance A_{geom}, the selection efficiency ϵ_{sel}^Z assuming no dependence on the incoming direction (θ, ϕ), and the minor correction factor δ described above. The product $A_{\text{geom}}\epsilon_{\text{sel}}^Z$ is determined from MC simulation [134] by calculating the number of events generated and detected in the rigidity interval $[R, R + \Delta R)$. Downward-going MC simulated events

are generated isotropically in the top plane of a $3.9 \times 3.9 \times 3.9$ m^3 concentric cube (i.e., the generation plane is at $z = 1.95$ m), which covers the entire AMS field of view, according to a generated rigidity $R_{\rm gen}$ spectrum $dN/dR_{\rm gen} \propto R_{\rm gen}^{-1}$. The value of the acceptance is representative only for a particular rigidity value $\tilde{R} \in [R, R + \Delta R]$ of the rigidity bin:

$$\begin{aligned} A(\tilde{R}) = A_{\rm geom} \cdot \epsilon^Z_{\rm sel}(R) \cdot [1 + \delta^Z(R)] &= A^Z_{\rm MC}(R)[1 + \delta^Z(R)] \\ &= A_0 \frac{N^Z_{\rm sel}(R)}{N^Z_{\rm gen}(R)}[1 + \delta_Z(R)] \\ &= A_0 \frac{N^Z_{\rm sel}(R)}{N^Z_{\rm gen}(R)}\kappa_Z(R), \end{aligned} \tag{3.3}$$

where $N^Z_{\rm gen}(R)$ and $N^Z_{\rm sel}(R)$ indicate the number of events generated and detected in the rigidity interval $[R, R + \Delta R)$ respectively, $\kappa_Z(R) = 1 + \delta_Z(R)$ represents the multiplicative scale factor used to correct the discrepancies between the simulation and data, and A_0 is the geometric factor for the event-generation plane. $\tilde{R}$ is calculated for a flux $\propto R^{-2.7}$ [135]; we have used Eq. (6) in Ref. [135] with $\tilde{R} \equiv x_{lw}$. For one side of the plane, the geometric factor A_0 is given by

$$\begin{aligned} A_0 = \int_S d\sigma \int_\Omega d\omega\, \hat{\boldsymbol{r}} = \int_S \int_\Omega \cos\theta\, d\omega\, d\sigma &= \int_S \int_0^{2\pi} \int_0^{\frac{\pi}{2}} \cos\theta \sin\theta\, d\theta\, d\phi\, d\sigma \\ &= \int_S \int_0^{2\pi} \int_0^{\frac{\pi}{2}} \frac{1}{2} d(\sin^2\theta)\, d\theta\, d\phi\, d\sigma \\ &= \int_S \pi\, d\sigma = \pi S = \pi \times 3.9 \times 3.9 \text{ m}^2\text{sr} \\ &\approx 47.78 \text{ m}^2\text{sr}, \end{aligned} \tag{3.4}$$

where $d\sigma$ is the element of surface area S and $d\omega = d\phi\, d\cos\theta$ is the element of solid angle Ω with θ and ϕ being the polar and azimuth angle respectively.

Figure 3-9 shows the acceptance for carbon as a function of MC generated rigidity $A^{Z=6}_{\rm MC}(R)$ before applying data-driven corrections, together with the parametrization using a spline function to smoothen out statistical fluctuations.

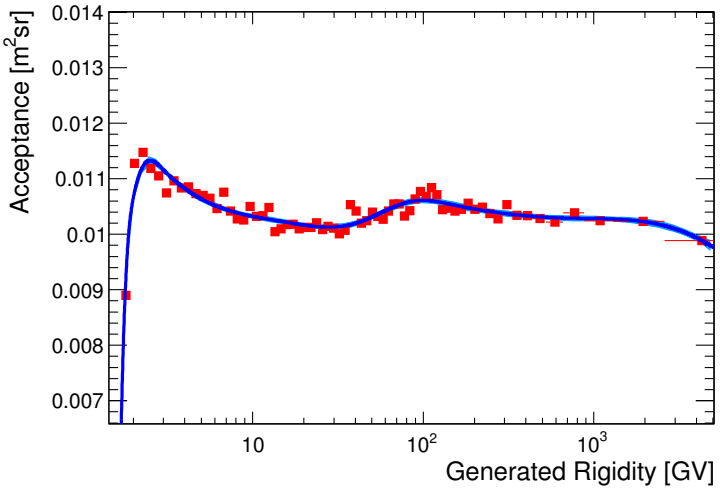

Figure 3-9: The effective acceptance for carbon as a function of generated rigidity before applying data-driven corrections (red squares). The blue curve shows the spline fit to the acceptance and the blue band represents the confidence interval of the fitted function at 68% confidence level (CL).

3.2.3 Data-Driven Corrections to the Effective Acceptance

The calculation of the acceptance $A^Z_{\rm MC}$ is completely based on MC simulation, which is, in fact, the only way to assess the absolute acceptance normalization. Due to the fact that the MC simulation may be imperfect (e.g., in describing the detector geometry and the interactions of particles in the AMS materials), any systematic discrepancy between the MC simulation and the data needs to be taken into account to correct $A^Z_{\rm MC}$.

In order to derive the data-driven scale factor κ_Z in Eq. (3.3), the selection criteria (except the purity cut and the orbital cuts) summarized in Section 3.1 are now re-grouped in five categories to define the samples and to determine corrections, which will be discussed in the next few sections. The efficiency and purity of the L1 charge cut is directly measured from data. The categories of efficiency are:

1) **ITk tracking efficiency $\epsilon^Z_{\rm ITk}$**:

   1.1) at least five hits in the y coordinate from L2 to L8 with the hit pattern of L2&(L3|L4)&(L5|L6)&(L7|L8);

1.2) track fit $\chi^2_{y,\,\mathrm{inner}}/\mathrm{d.f.} < 10$;

1.3) $Z - 0.45 < Z_{\mathrm{inner}} < Z + 0.45$ and $\mathrm{RMS}_{\mathrm{ITk\ Q}} < 0.55$;

1.4) β object is built using TOF signals plus tracker track information;

1.5) $\beta_{\mathrm{TOF}} > 0.4$.

2) **tracker L1 selection efficiency $\boldsymbol{\epsilon^Z_{\mathrm{L1}}}$**:

2.1) tracker L1 hit with good reconstructed clusters on both x and y coordinates and $Z - 0.46 - (Z-3) \times 0.16 < Z_{\mathrm{L1}}$;

2.2) track fit $\chi^2_{y,\,\mathrm{L1\ to\ L8}}/\mathrm{d.f.} < 10$.

3) **tracker L9 selection efficiency $\boldsymbol{\epsilon^Z_{\mathrm{L9}}}$**:

3.1) tracker L9 hit with clusters reconstructed on both x and y coordinates and $Z - 0.5 < Z_{\mathrm{L9}} < Z + 1.5 + (Z-3) \times 0.06$;

3.2) track fit $\chi^2_{y,\,\mathrm{L2\ to\ L9}}/\mathrm{d.f.} < 10$.

4) **TOF charge selection efficiency $\boldsymbol{\epsilon^Z_{\mathrm{TOF}}}$**:

4.1) $Z - 0.6 < Z_{\mathrm{upper\ TOF}} < Z + 1.5$ and $Z - 0.6 < Z_{\mathrm{lower\ TOF}}$.

5) **trigger efficiency $\boldsymbol{\epsilon^Z_{\mathrm{trg}}}$**.

5.1) physics trigger.

The scale factor as a function of rigidity R can be derived from:

$$\begin{aligned}\kappa_Z(R) &= \frac{\epsilon^Z_{\mathrm{ITk,data}}(R)}{\epsilon^Z_{\mathrm{ITk,MC}}(R)} \cdot \frac{\epsilon^Z_{\mathrm{L1,data}}(R)}{\epsilon^Z_{\mathrm{L1,MC}}(R)} \cdot \frac{\epsilon^Z_{\mathrm{L9,data}}(R)}{\epsilon^Z_{\mathrm{L9,MC}}(R)} \cdot \frac{\epsilon^Z_{\mathrm{TOF,data}}(R)}{\epsilon^Z_{\mathrm{TOF,MC}}(R)} \cdot \frac{\epsilon^Z_{\mathrm{trg,data}}(R)}{\epsilon^Z_{\mathrm{trg,MC}}(R)} \\ &= \kappa^Z_{\mathrm{ITk}}(R) \cdot \kappa^Z_{\mathrm{L1}}(R) \cdot \kappa^Z_{\mathrm{L9}}(R) \cdot \kappa^Z_{\mathrm{TOF}}(R) \cdot \kappa^Z_{\mathrm{trg}}(R). \end{aligned} \tag{3.5}$$

In this case, the trigger efficiency term in Eq. (3.2) is contained in the effective acceptance and the L1 purity cut efficiency term is taken out from the effective acceptance. Thus, Eq. (3.2) is expressed as

$$\Phi^Z_i = \frac{N^Z_i}{A^Z_{\mathrm{MC},i} \cdot \kappa_{Z,i} \cdot \epsilon^Z_{\mathrm{L1\ purity},i} \cdot T_i \cdot \Delta R_i}, \tag{3.6}$$

where $\epsilon^{Z}_{\text{L1 purity},i}$ is the L1 purity cut efficiency.

To study the efficiency of the selection cuts related to a given subdetector, we need an independent sample of clean events selected by other subdetectors. We present the analysis of carbon nuclei ($Z = 6$) as an example.

3.2.3.1 ITk Tracking Efficiency

Since the tracker track cannot be used for this study, a standalone reconstruction of the TOF β (called β_{s}) was performed using the signals from TOF and TRD. Then β_{s} was used to reconstruct other TOF-related variables such as the upper TOF charge and lower TOF charge. To study the rigidity dependence of the efficiency, in different rigidity ranges we used different variables as an alternative estimator of the particle rigidity.

1) Below 6 GV, β_{s} was converted to rigidity based on Eq. (3.7):

$$R = \frac{A\, m_{\text{n}} \beta}{Z\sqrt{1-\beta^2}} \tag{3.7}$$

where A is the particle mass number and m_{n} is the nucleon mass. This estimation is valid only up to ~ 5 GV limited by the TOF β resolution.

2) Between 6 GV and 20 GV, the geomagnetic cutoff rigidity R_{c} was used to estimate the particle rigidity, since the CR nuclei spectrum is falling steeply such that R_{c} can be used to represent the rigidity of the bulk of particles up to few tens of GV. For simulated events the MC generated rigidity was used.

3) The last estimator was the ECAL energy deposition E_{edep} which was only used as a cross-check of the previous estimators and provided a potential indication of the behavior of the efficiency at higher energies (from few tens of GV to few hundreds of GV).

Both R_{c} and E_{edep} were corrected using their observed correlations with the tracker rigidity R. For example, in different E_{edep} intervals we performed a gaussian fit to $\eta = E_{\text{edep}}/R$ to obtain the mean value $\hat{\eta}$ and then parameterized the E_{edep} dependence of $\hat{\eta}$ using a spline function (see Appendix A.1). This fitted function was used to

calibrate E_{edep} to R and R_{c} was corrected in a similar way. These corrections have been done individually for each nucleus sample and separately for the simulation and data.

The major cuts used to select a pure sample of unbiased carbon nuclei for this efficiency measurement (i.e., the denominator) include:

1) passing physics trigger;
2) TRD track extrapolation within the tracker L1–L9 fiducial volume;
3) the unbiased estimation of L1 charge reconstructed from the L1 hit associated to the TRD track extrapolation $Q_{\text{L1}}^{\text{unb}} \in (5.55, 6.5)$;
4) the unbiased estimation of L9 charge based on the ECAL shower axis extrapolation $Q_{\text{L9}}^{\text{unb}} \in (5.5, 7)$, which is used to prevent pre-shower in the tracker so as to ensure a clean sample of unfragmented carbon nuclei.

Figure 3-10 shows the ITk tracking efficiency for carbon data and simulation as a function of estimated rigidity. The parameterization of the data/MC efficiency ratio is assumed to be flat above few tens of GV, which is indicated by the efficiency trend in the E_{edep} estimator range. The flattening of the rigidity dependence of this efficiency is also predicted by MC simulation in generated rigidity as shown in Figure 3-10. Overall, a good agreement between data and simulation is found.

3.2.3.2 L1 Selection Efficiency

The L1 selection efficiency measurement includes two components:

1) L1 large-charge hit (both X- and Y-side) efficiency $\epsilon_{\text{L1}}^{\text{BZ hit}}$. This is the probability of having a hit on L1 with charge greater than 5.06 (called BZ hit). The selection cut under study is: $Z - 0.46 - (Z-3) \times 0.16 = 5.06 < Q_{\text{L1}}^{\text{max}}$ with good reconstructed X- and Y-side clusters, where $Q_{\text{L1}}^{\text{max}}$ is the charge with the largest amplitude reconstructed from the unbiased hit (not necessarily attached to the tracker track) on L1.
2) L1 BZ hit pick-up efficiency $\epsilon_{\text{L1}}^{\text{pick-up}}$. This is the probability that the BZ hit is associated to the ITk track extrapolated to L1. The selection cut under study is: $Z_{\text{L1}} > 5.06$ and track fit $\chi^2_{y,\,\text{L1 to L8}}/\text{d.f.} < 10$.

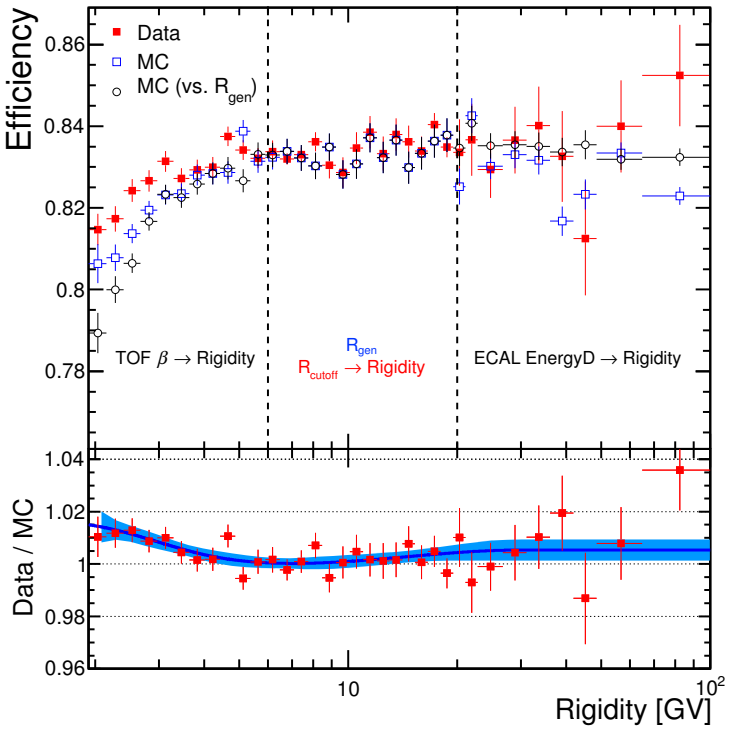

Figure 3-10: ITk tracking efficiency for carbon data (red filled squares) and simulation as a function of estimated rigidity (blue open squares) and for illustration MC generated rigidity (black open circles). The bottom panel shows the ratio of the efficiency measured in data to simulation. The blue curve and band represent the spline fit to the ratio and the 68% CL interval, respectively.

Therefore, $\epsilon_{\rm L1} = \epsilon_{\rm L1}^{\rm BZ\ hit} \cdot \epsilon_{\rm L1}^{\rm pick\text{-}up} \Rightarrow \kappa_{\rm L1} = \kappa_{\rm L1}^{\rm BZ\ hit} \cdot \kappa_{\rm L1}^{\rm pick\text{-}up}$. The estimation of $\epsilon_{\rm L1}$ is split into two steps so that we can verify the carbon-nuclear elastic scattering of the simulation by comparing its $\epsilon_{\rm L1}^{\rm pick\text{-}up}$ with the data. The L1 BZ hit pick-up efficiency reflects the elastic scattering effect on particles traversing the material between L1 and L2.

The major cuts used to select clean samples for $\epsilon_{\rm L1}^{\rm BZ\ hit}$ and $\epsilon_{\rm L1}^{\rm pick\text{-}up}$ measurements (the denominator) include:

1) passing physics trigger;

2) ITk track extrapolation within the L1–L9 fiducial volume;

3) the ITk selection criteria described in Section 3.1;

4) $5.5 < Z_{\rm L9} < 6.9$ with X- and Y-hit on L9;

5) L2–L9 track fit $\chi^2_{y,\,\rm L2\ to\ L9}/{\rm d.f.} < 10$;

6) $5.5 < Z_{\rm upper\ TOF} < 7$.

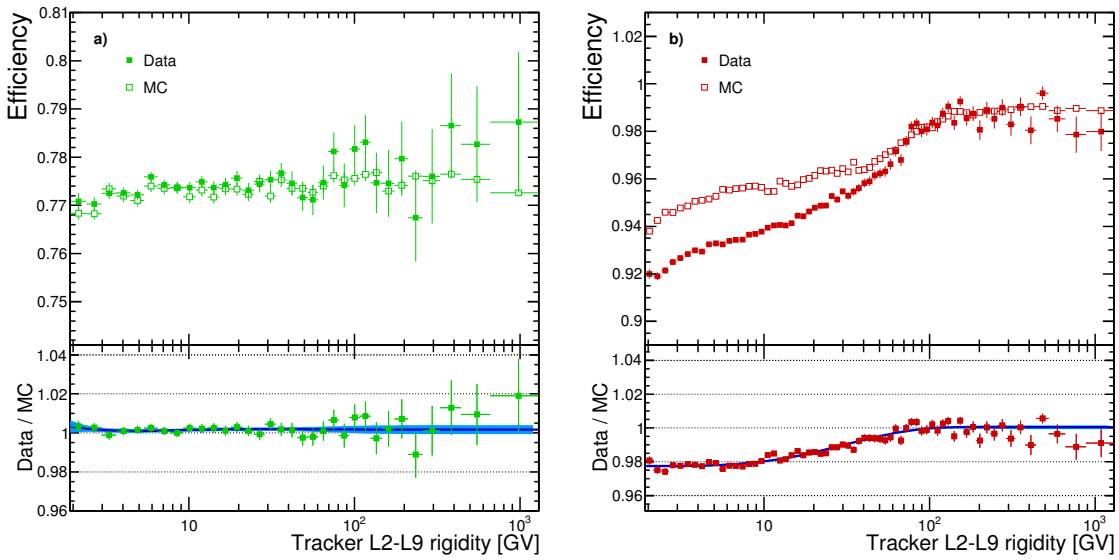

Figure 3-11: Tracker L1 selection efficiency: a) L1 BZ hit efficiency and b) L1 BZ hit pick-up efficiency for carbon data (filled squares) and simulation (open squares) as functions of rigidity. Each bottom panel shows the ratio of the efficiency measured in data to simulation, along with the spline fit to the ratio (blue curve) and the 68% CL interval (blue band).

In addition, for the sample of the $\epsilon_{\mathrm{L1}}^{\text{pick-up}}$ measurement, a tight cut on $Q_{\mathrm{L1}}^{\max}$ ($Q_{\mathrm{L1}}^{\max} < 6.5$) is applied in order to remove carbon events from spallation of heavier nuclei (mainly from oxygen); these background events have a charge compatible with $Z = 6$ in the ITk while compatible with $Z = 8$ on L1.

The rigidity measured using the information from L2 to L9, $R_{\mathrm{L2\ to\ L9}}$, provides the determination of the rigidity dependence of $\epsilon_{\mathrm{L1}}^{\text{BZ hit}}$ and $\epsilon_{\mathrm{L1}}^{\text{pick-up}}$. Figure 3-11 shows $\epsilon_{\mathrm{L1}}^{\text{BZ hit}}$ and $\epsilon_{\mathrm{L1}}^{\text{pick-up}}$ for carbon data and simulation as functions of rigidity. The pick-up efficiency increases with rigidity since the effect of elastic scattering becomes less significant with increasing rigidity, and reaches $\sim$ 99% at the plateau. The good agreement of $\epsilon_{\mathrm{L1}}^{\text{pick-up}}$ between the simulation and data verifies the elastic cross-sections of the model implemented in the simulation up to a residual 2% discrepancy below few tens of GV.

3.2.3.3 L9 Selection Efficiency

The L9 selection efficiency combines 1) the survival probability of carbon nuclei traversing materials between L8 and L9 (the thin aluminum and carbon fiber ITk enclosure, the lower TOF, and the RICH radiator), $P_{\text{L8–L9}}$, and 2) the L9 hit pick-up efficiency $\epsilon_{\text{L9}}^{\text{pick-up}}$. Thus, $\epsilon_{\text{L9}} = P_{\text{L8–L9}} \cdot \epsilon_{\text{L9}}^{\text{pick-up}}$ and $P_{\text{L8–L9}} = \epsilon_{\text{L9}}/\epsilon_{\text{L9}}^{\text{pick-up}}$.

First, we restrict the L9 selection efficiency measurement in both L9 and ECAL geometry by selecting event samples with extrapolated ITk tracks passing through both L9 and ECAL. This allows us to use the ECAL charge estimator [136] to select non-interacting carbon and oxygen samples below L9 for the measurement of $\epsilon_{\text{L9}}^{\text{pick-up}}$, so that we can derive $P_{\text{L8–L9}}$ from ϵ_{L9} and $\epsilon_{\text{L9}}^{\text{pick-up}}$ within L9 and ECAL geometry. Although the ECAL charge resolution ($\sim 30\%$ for carbon nuclei [136]) is not as good as the tracker, it is sufficient to select a relatively clean sample of carbon or oxygen events for $\epsilon_{\text{L9}}^{\text{pick-up}}$ measurement combining the charge ID ability of L1–L8 and ECAL. The material traversed by nuclei between L1 and L9 is composed primarily of carbon and aluminum [116]. The corresponding inelastic cross-sections for C+C and C+Al have only been measured below 10 GV and for O+C below 1 GV [137–145]. To verify the MC predictions, the survival probabilities of carbon and oxygen nuclei that traverse the material between L8 and L9 were measured in data and compared with simulations with the Glauber-Gribov inelastic cross-sections [121, 122] varied within $\pm 10\%$. The resulting cross-sections with the best agreement with data above 30 GV were chosen. Figure 3-12 shows the measured carbon survival probability between L8 and L9 compared with the simulation. A good agreement between data and simulation has been achieved.

Second, we calculate the number of events that pass L9 selection in full L9 geometry and in ECAL geometry, $N_{\text{L9-geom}}^{\text{sel}}$ and $N_{\text{ECAL-geom}}^{\text{sel}}$, respectively, and then obtain their ratio. This ratio is used as a multiplicative scale factor to extrapolate the L9 selection efficiency measured in ECAL geometry to full L9 geometry. Thus, we have $\kappa_{\text{L9}} \equiv \kappa_{\text{L9}}^{\text{L9-geom}} = \kappa_{\text{L9}}^{\text{ECAL-geom}} \cdot (N_{\text{L9-geom}}^{\text{sel}}/N_{\text{ECAL-geom}}^{\text{sel}})$.

The selection of clean samples (the denominator) for ϵ_{L9} measurement is mainly

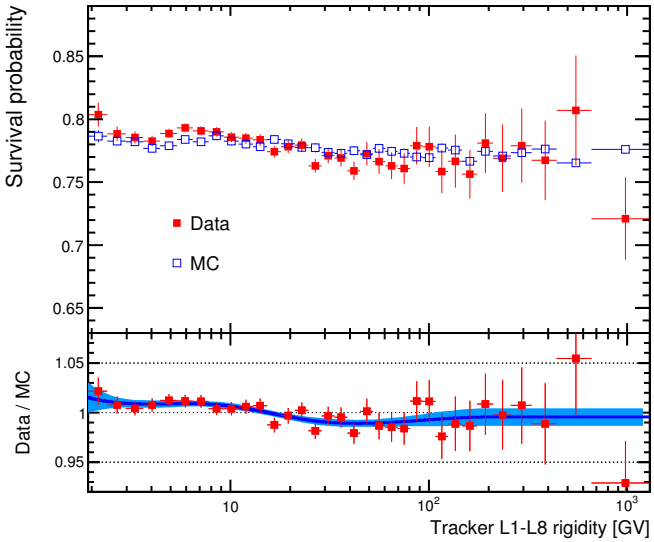

Figure 3-12: Carbon survival probability between tracker L8 and L9 as a function of rigidity. The bottom panel shows the data/MC ratio of the survival probability. The shaded area represents the 68% CL interval obtained from the spline fit to the ratio.

based on L1–L8, such as $Z-0.3 < Z_{\mathrm{L1}} < Z+0.5$ and $Z-0.45 < Z_{\mathrm{L2\ to\ L8}} < Z+0.45$. The rigidity measured using the information from L1 to L8, $R_{\mathrm{L1\ to\ L8}}$, provides the determination of the rigidity dependence of $P_{\mathrm{L8–L9}}$ and other L9-related efficiencies. Figures 3-13(a) and 3-13(b) show the rigidity dependence of $\epsilon_{\mathrm{L9}}^{\mathrm{ECAL\text{-}geom}}$ (along with $\kappa_{\mathrm{L9}}^{\mathrm{ECAL\text{-}geom}}$) and $N_{\mathrm{ECAL\text{-}geom}}^{\mathrm{sel}}/N_{\mathrm{L9\text{-}geom}}^{\mathrm{sel}}$, respectively.

3.2.3.4 TOF Charge Selection Efficiency

The selection of clean samples (the denominator) for the measurement of the upper and lower TOF charge selection efficiency is mainly based on the tracker charge ID, i.e., by applying a tight cut on the ITk charge $Z-0.2 < Z_{\mathrm{L2\ to\ L8}} < Z+0.3$. The rigidity dependence of the efficiency is also determined by the tracker (L1–L9). Figure 3-14 shows the TOF charge selection efficiency as a function of rigidity for carbon. The agreement between data and simulation is better than 1% over the entire rigidity range.

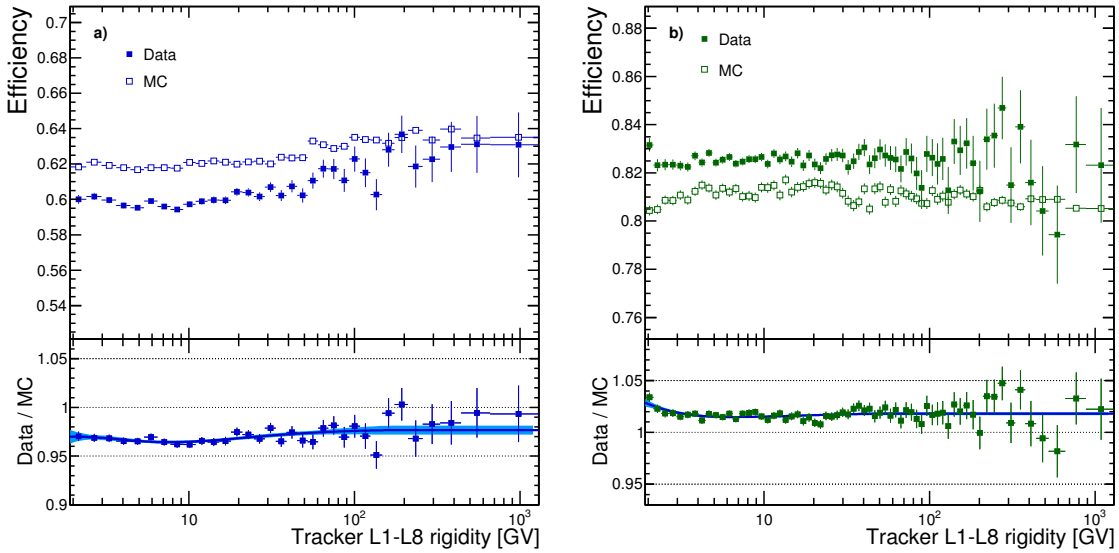

Figure 3-13: a) Tracker L9 selection efficiency measured in both L9 and ECAL geometry, and b) the ratio of the number of events that pass L9 selection in ECAL geometry over that in full L9 geometry, for carbon data and simulation as functions of rigidity. Each bottom panel shows the data/MC ratio and the spline fit to the ratio (blue curve) with the 68% CL interval (blue band).

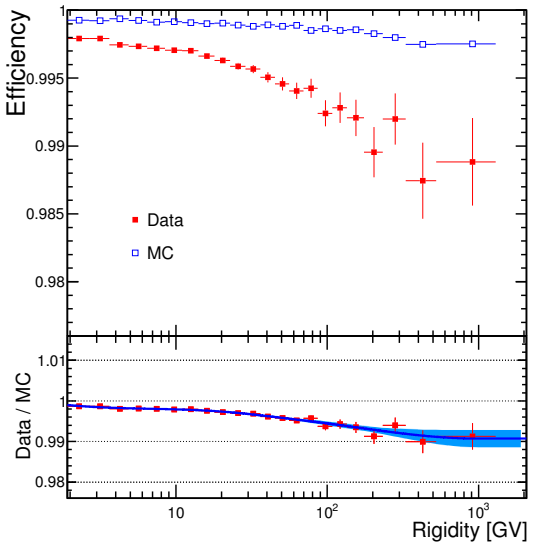

Figure 3-14: TOF charge selection efficiency for carbon data and simulation as a function of rigidity. The bottom panel shows the data/MC ratio of the efficiency. The blue shaded area represents the 68% CL interval obtained from the spline fit to the ratio (blue curve).

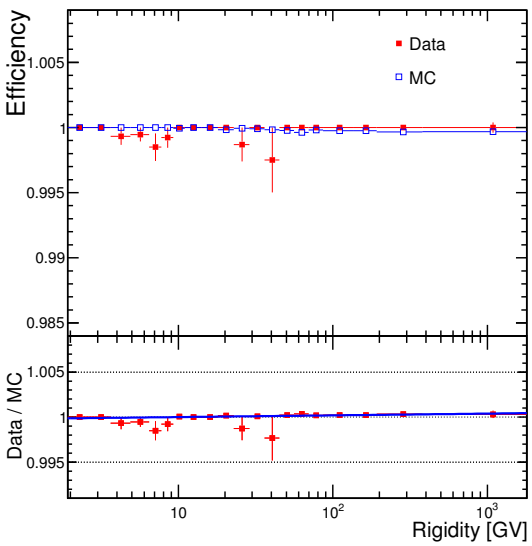

Figure 3-15: Trigger efficiency for carbon data and simulation as a function of rigidity in the FS analysis. The bottom panel shows the data/MC ratio of the efficiency. The blue shaded area represents the 68% CL interval obtained from the spline fit to the ratio (blue curve).

3.2.3.5 Trigger Efficiency

The trigger conditions and logic used in light nuclei fluxes analysis have been described in Section 2.1.9. The physics trigger efficiency $\epsilon_{\rm trg}$ is measured with the unbiased trigger (see trigger (iii) in Section 2.1.9) events and is given by

$$\epsilon_{\rm trg} = \frac{N_{\rm trg}^{\rm physics}}{N_{\rm trg}^{\rm physics} + f_{\rm prescale} \times N_{\rm trg}^{\rm unbiased}},$$

where $f_{\rm prescale}$ is the prescale factor that takes the value of 100 (1) in data (simulation). The selection of the sample (the denominator) relies on all the other cuts used in the flux analysis; I.e., the trigger cut is treated as the last cut in this efficiency measurement. Figure 3-15 shows the measured trigger efficiency as a function of rigidity for carbon in the FS analysis.

3.2.4 Total Correction to the Effective Acceptance

According to Eq. (3.5) we obtain the scale factor κ multiplying the effective acceptance obtained from MC simulation, which quantizes the difference in efficiencies between data and simulation. Because the MC samples are generated with a single power law rigidity spectrum $dN/dR_{\rm gen} \propto R_{\rm gen}^{-1}$, in order to represent the spectral shape of the incident CR flux these MC samples have been reweighted event-by-event according to the preliminary spectrum measured in data when we compare the efficiencies between data and simulation as functions of reconstructed rigidity. For data, events in the sample for each efficiency measurement are also required to pass the bin cutoff selection.

The rigidity dependence of the scale factor for carbon MC acceptance, $\kappa_{Z=6}(R)$, and its breakdown (i.e., $\kappa_{\rm ITk}^{Z=6}(R)$, $\kappa_{\rm ITk}^{Z=6}(R)$, $\kappa_{\rm L1}^{Z=6}(R)$, $\kappa_{\rm L9}^{Z=6}(R)$, $\kappa_{\rm TOF}^{Z=6}(R)$, and $\kappa_{\rm trg}^{Z=6}(R)$) are shown in Figure 3-16(a) and 3-16(b), respectively. The excursion of the correction factor below $\sim$ 100 GV is basically due to the corrections of the hit pick-up efficiencies in the outer most tracker layers (L1 and L9). These are most influenced by uncertainties in the nuclear cross-sections.

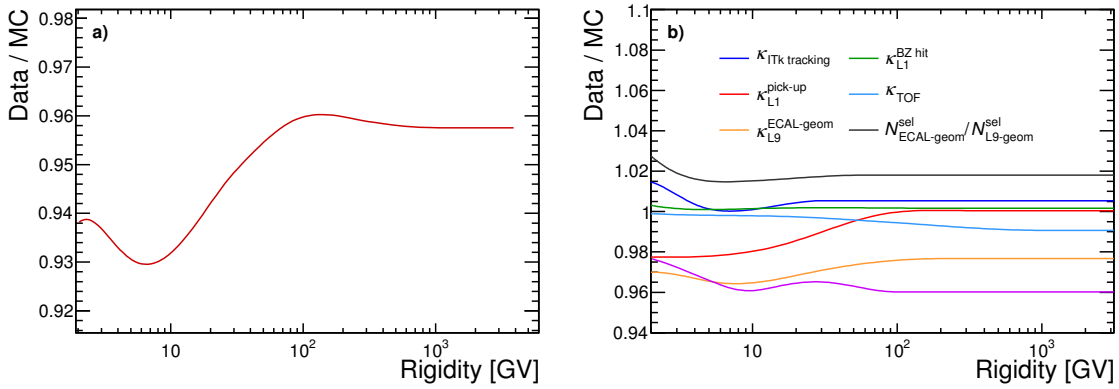

Figure 3-16: a) The data-driven scale factor for the carbon MC effective acceptance as a function of rigidity, $\kappa_{Z=6}(R)$, which has been parameterized by a spline function. b) The breakdown of $\kappa_{Z=6}(R)$.

3.2.5 Background Contamination

After applying charge selections on the L1, ITk, upper TOF, and lower TOF, the impurities of the carbon and oxygen samples come from two sources.

First is the residual background to carbon and oxygen events which results from the interactions of heavier nuclei such as N, O, F, and Ne in the material between L1 and L2 (the TRD and upper TOF). Applying a cut on the L1 charge measurement, $Z_{\text{L1}} < Z+0.65+(Z-5)\times 0.03$, is an important method to remove background events in data. The background to carbon events is evaluated using a data-driven method, i.e., by fitting the charge distribution from L1 with charge distribution templates of C, N, and O as shown in Figure 3-17. The charge distribution templates are obtained from a selection of non-interacting samples at L2 by the use of the charge measurements with L1 and L3–L8. The charge distributions should be nearly identical for L1 and L2, since the layout and electronics are the same and the full tracker (all electronic components) has been calibrated.

The resulting purity of the sample is calculated by integrating the charge templates distribution in the selection range, and found to be $> 99.5\%$ for carbon (as shown in Figure 3-18(a)) and compatible with 1 for oxygen over the entire rigidity range. The efficiency corresponding to this purity cut is also estimated from the non-interacting samples on L2 and its rigidity dependence is shown in Figure 3-18(b).

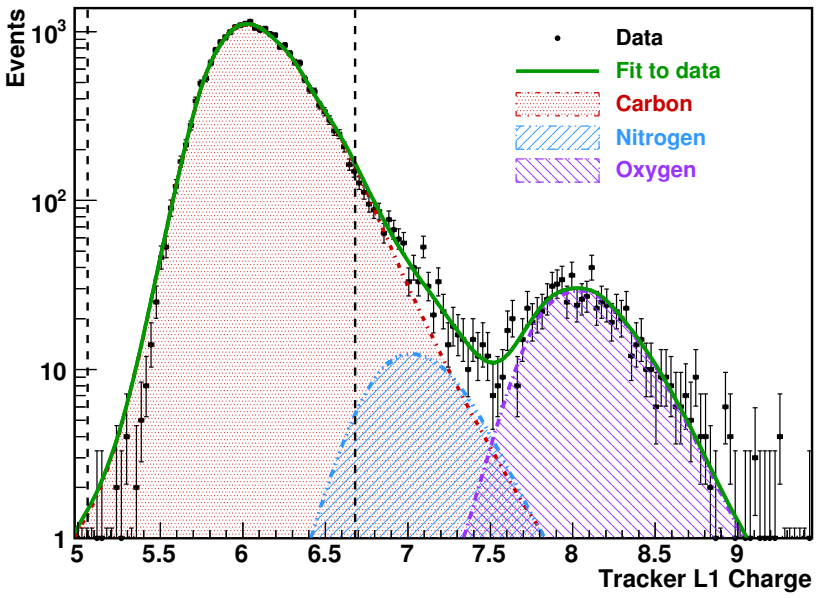

Figure 3-17: Charge distributions measured by tracker L1 for carbon events selected by the ITk in the rigidity range from 9 GV to 11 GV (circles). The solid green curve shows the fit to the data of the C, N, and O charge distribution templates. The templates are obtained from selected samples of non-interacting nuclei at L2 by the use of the charge measurement with L1 and L3–L8. The charge selections applied to L1 hits are shown as vertical dashed lines.

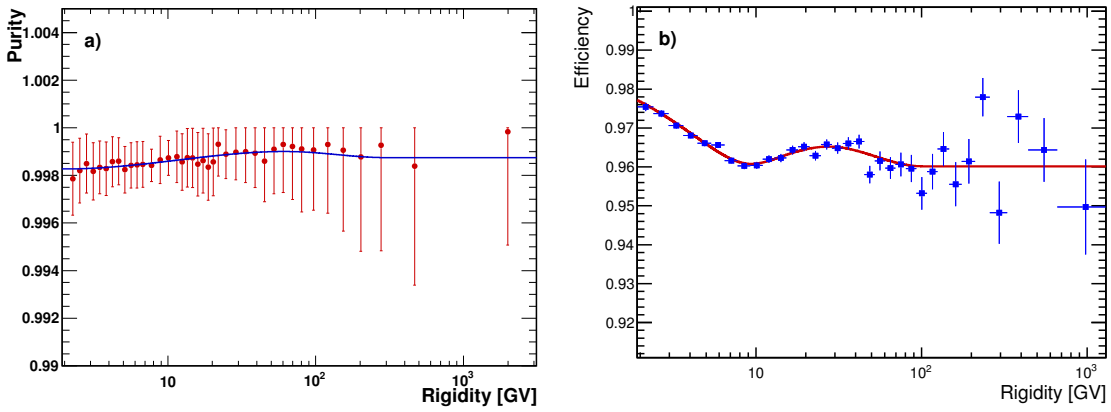

Figure 3-18: a) Purity of the carbon sample after applying charge selections on the L1, ITk, upper TOF, and lower TOF, parameterized by a spline function (blue curve). b) Efficiency of the charge selections on L1 for carbon, estimated from the non-interacting samples on L2 and parameterized by a spline function (red curve).

Second is the background from N, O, F, and Ne interacting in materials above L1 (thin support structures made of carbon fiber and aluminum honeycomb). This correction is called the Top-Of-Instrument (TOI) correction. It has been estimated from simulation, using MC samples reweighted according to AMS flux measurements (e.g., MC oxygen samples are reweighted to the oxygen flux from this analysis). Due to their abundance in CRs, only nuclei with $6 < Z \leq 8$ play a significant role in the background from interactions above L1 in the carbon sample ($< 0.5\%$ over the entire rigidity range) and this background contamination is negligible in the oxygen sample.

Since only the background from oxygen flux is non-negligible, the carbon flux with the TOI correction can be expressed as

$$\begin{aligned}\Phi_{Z=6} \equiv \Phi_{\mathrm{C}} = \frac{N_{\mathrm{C}}}{A_{\mathrm{C}}\,T\,\Delta R} = \frac{N'_{\mathrm{C}} - N_{\mathrm{O}\to\mathrm{C}}}{A_{\mathrm{C}\to\mathrm{C}}\,T\,\Delta R} &= \frac{N'_{\mathrm{C}} - \Phi_{\mathrm{O}}\,A_{\mathrm{O}\to\mathrm{C}}\,T\,\Delta R}{A_{\mathrm{C}\to\mathrm{C}}\,T\,\Delta R} \\ &= \Phi'_{\mathrm{C}}\left(1 - \frac{A_{\mathrm{O}\to\mathrm{C}}}{A_{\mathrm{C}\to\mathrm{C}}} \cdot \frac{\Phi_{\mathrm{O}}}{\Phi'_{\mathrm{C}}}\right) \\ &= \Phi'_{\mathrm{C}}(1 - \delta_{\mathrm{O}}), \end{aligned} \tag{3.8}$$

where Φ'_{C} is the carbon flux without the TOI correction and $A_{\mathrm{O}\to\mathrm{C}}$ ($A_{\mathrm{C}\to\mathrm{C}}$) is the carbon acceptance obtained from MC oxygen (carbon) samples. When calculating $A_{\mathrm{O}\to\mathrm{C}}$ and $A_{\mathrm{C}\to\mathrm{C}}$, the L1 purity cut $Z_{\mathrm{L1}} < Z + 0.65 + (Z-5) \times 0.03$ for carbon ($Z = 6$) is included in the numerator so that the TOI correction only deals with the background from interactions *above L1*.

The MC oxygen (carbon) samples have been reweighted to the measured oxygen (carbon) flux Φ_{O} (Φ'_{C}) and the MC acceptance $A_{\mathrm{O}\to\mathrm{C}}$ ($A_{\mathrm{C}\to\mathrm{C}}$) is expressed in reconstructed rigidity phase space (called the folded acceptance), to account for the bin-to-bin migration effect due to the finite tracker rigidity resolution. Figure 3-19 shows the acceptance ratio $A_{\mathrm{O}\to\mathrm{C}}/A_{\mathrm{C}\to\mathrm{C}}$ as a function of reconstructed rigidity. Then we can obtain the TOI correction factor for the carbon flux, i.e., $(1-\delta_{\mathrm{O}})$ in Eq. (3.8), once Φ_{O} and Φ'_{C} are determined. As the C/O ratio is ~ 1, this background is expected to be $< 0.5\%$ over the entire rigidity range for carbon. More importantly, the partial fragmentation cross-sections in the MC simulation have been validated using data;

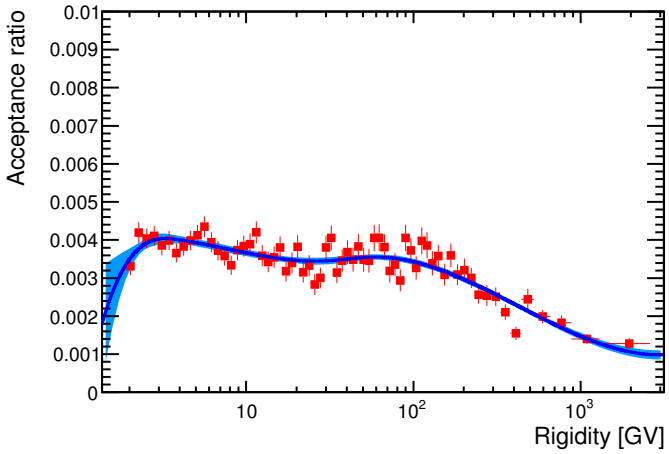

Figure 3-19: The acceptance ratio $A_{O\to C}/A_{C\to C}$ as a function of reconstructed rigidity (red squares). The blue curve shows the spline fit to the ratio and the blue band represents the 68% CL interval.

e.g., the validation of simulated partial cross-sections C + C, Al $\to$ B + X is shown in Figure 3 of the Supplemental Material of Ref. [83].

3.2.6 Unfolding

The migration of events from one rigidity bin to another causes a distortion of the measured CR particle flux and especially modifies the spectral index. This bin-to-bin migration effect is mainly due to 1) that the particle loses energy when traversing the detector (e.g., by ionization or, for electrons and positrons, bremsstrahlung) and 2) that the measurement of rigidity is blurred by the finite resolution of the tracker. At high rigidities, the resolution effect plays an important role because of the sharply falling power-law spectrum of CRs—there are relatively more particles migrating to a higher rigidity bin than the other way around.

The bin-to-bin migration of events is corrected using unfolding procedures, in which the rigidity resolution function is obtained from the MC simulation and verified with the data. Among many unfolding procedures, we select the two that have been used in previous AMS publications [83,116,129] for this analysis. The validity of both has6 been verified by our MC simulations. The unfolding procedure is performed after

the background subtraction.

In the first procedure, hereafter called the Folded Acceptance Method (FAM), the flux is obtained iteratively [146–148]. Initially, the flux is evaluated using Eq (3.6) without taking the rigidity resolution function into account. Subsequently, at each iteration, the folded acceptance A' is calculated for each bin, $A' = (1/\Phi_i) \sum_j \Phi_j \, A_j \, M_{ij}$, where M_{ij} is the element of the migration matrix which connects true bin j to observed bin i and is obtained from the rigidity resolution function. The folded acceptance reflects both the detector acceptance and the detector resolution and depends therefore on the flux shape. A' (A) is expressed in reconstructed (generated) rigidity phase space. Next, A'/A is parametrized using a spline function. Finally, the number of observed events is corrected bin by bin by a factor $C = A'/A$ and the flux is reevaluated using Eq (3.6). Now with the unfolding factor C the number of events in bin i can be obtained: $N_i = \aleph_i / C_i$, where $\aleph_i$ is the number of observed events in bin i. The reweighting of the MC simulated events is also updated at each iteration, i.e., the MC reconstructed rigidity spectrum is reweighted to the measured flux obtained from the previous iteration. The iteration proceeds until the fluxes between two successive steps agree within $\sim \mathcal{O}(0.1\%)$. In this work, the convergence of the iterative procedure is reached when $\chi^2_{\text{unf}}/n_{\text{bins}} \sim 10^{-3}$, where n_{bins} is the number of bins in the flux measurement and

$$\chi^2_{\text{unf}} = \sum_{k=1}^{n_{\text{bins}}} \left(\frac{N_k^{\text{now}} - N_k^{\text{before}}}{\sqrt{N_k^{\text{before}}}} \right)^2 .$$

In this unfolding procedure, the regularization steps to reduce statistical fluctuations in data include the parameterization of:

1) the measured data event rate as a functon of rigidity, which is subsequently used to reweight the simulated events;
2) the multiplicative correction factors as a functon of rigidity (i.e., the data/MC ratio of the reconstructed rigidity spectrum) that are applied to the weights of the simulated events in the next iteration;
3) the unfolding factor $C = A'/A$ as a functon of rigidity.

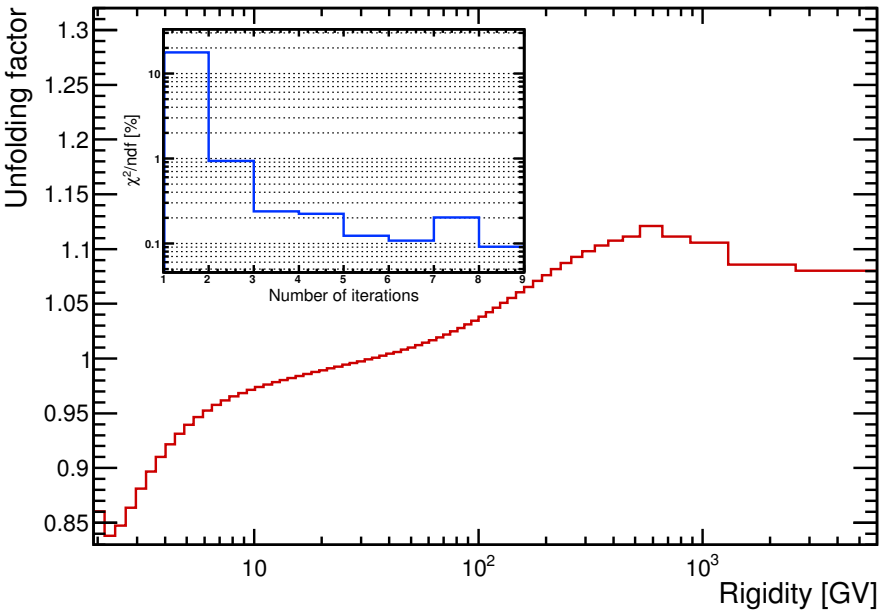

Figure 3-20: The parameterized ratio of the folded acceptance to unfolded acceptance (A'/A) after eight iterations. The inset shows the convergence of the iterative procedure.

Each of them is parameterized using a spline function to smooth out fluctuations.

Figure 3-20 shows the rigidity dependence of the parameterized unfolding factor for the carbon flux along with the convergence of the iterative procedure. As seen, this correction, $(N_i - \aleph_i)/\aleph_i = 1/C_i - 1$, is +16% at 2 GV, +5% at 6 GV decreasing smoothly to −7% at 200 GV, and reaches −11% at 600 GV and −8% at 2 TV.

The second procedure is based on a forward unfolding technique [149], hereafter called the Forward Unfolding Method (FUM). A set of spline functions (in log-log scale) with different node positions is used to parametrize the corrected number of events per bin, such that a "true" flux model $\Phi_{\rm t}$ is established. The spline functions are folded with the migration matrix M_{ij} (i.e., the unfolded flux model becomes a folded flux model) and then fit to the data. The average of those spline functions compatible with data is used to obtain N_i.

With the initial true flux model $\Phi_{\rm t}$, this folded event rate corrected with the scale

factor in inverse rigidity bin i (bin width $\Delta\frac{1}{R_{\rm m}}$) is given by

$$f_i \cdot \kappa_i = \int_{\frac{1}{R_{\rm m}}}^{\frac{1}{R_{\rm m}}+\Delta\frac{1}{R_{\rm m}}} \int_0^{\infty} \Phi_{\rm t}\left(\frac{1}{R_{\rm t}}\right) A\left(\frac{1}{R_{\rm t}}\right) \mathrm{Res}\left(\frac{1}{R_{\rm m}}-\frac{1}{R_{\rm t}}\right) d\frac{1}{R_{\rm t}}\, d\frac{1}{R_{\rm m}}, \tag{3.9}$$

where $R_{\rm m}$ and $R_{\rm t}$ are the measured rigidity and true rigidity, respectively, and $\mathrm{Res}(1/R_{\rm m}-1/R_{\rm t})$ is the rigidity resolution function. The scale factor κ is a function of measured rigidity and is put on the left hand side of Eq.(3.9), so that the terms on the right (left) hand side of Eq.(3.9) are in true (measured) rigidity phase space.

The goal is to obtain $\Phi_{\rm t}$ by minimizing

$$\chi^2 = \sum_{i=1}^{n_{\rm bins}} \left(\frac{\aleph_i/T_i - f_i}{\varsigma_i}\right)^2$$

where ς_i is the statistical error of the observed event rate $\aleph_i/T_i$. This is performed based on a least squares minimization. Hence, the unfolding factor in bin i can be obtained:

$$C_i = \frac{\hat{\aleph}_i}{\hat{N}_i} = \frac{\int_{\frac{1}{R_{\rm m}}}^{\frac{1}{R_{\rm m}}+\Delta\frac{1}{R_{\rm m}}} \int_0^{\infty} \Phi_{\rm t}\left(\frac{1}{R_{\rm t}}\right) A\left(\frac{1}{R_{\rm t}}\right) \mathrm{Res}\left(\frac{1}{R_{\rm m}}-\frac{1}{R_{\rm t}}\right) d\frac{1}{R_{\rm t}}\, d\frac{1}{R_{\rm m}}}{\int_0^{\infty} \Phi_{\rm t}\left(\frac{1}{R_{\rm t}}\right) A\left(\frac{1}{R_{\rm t}}\right) d\frac{1}{R_{\rm t}}}.$$

The small differences between the two unfolding procedures are accounted for as a systematic error.

3.2.6.1 Verification of the Rigidity Resolution Function

The rigidity resolution functions $\Delta(1/R)$ for carbon and oxygen have a dominant Gaussian core characterized by width σ and non-Gaussian tails more than 2.5σ away from the center [83,116]. The resolution functions are obtained from MC simulations.

In this work, the rigidity resolution is parameterized by a "stretched" Gaussian distribution:

$$f(x) = C_0 \exp\left[-\frac{(x-\mu)^2}{2\sigma^2}\right],$$

where σ is a spline function of x: $\sigma = \sigma(|x-\mu|)$. The free parameters of the

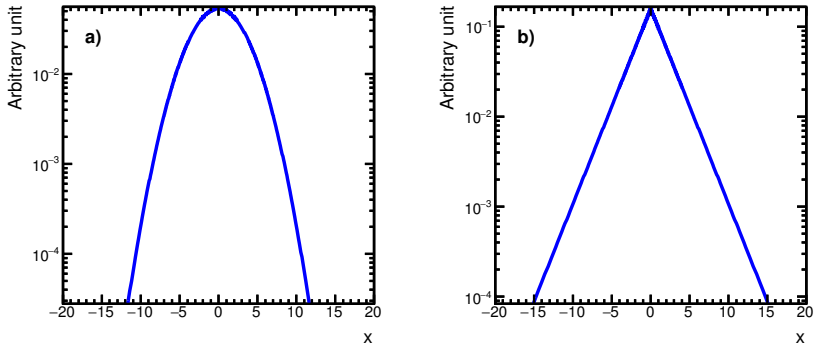

Figure 3-21: a) Gaussian PDF $g(x;\mu,\sigma)$ with $\mu = 0$ and $\sigma = 3$. b) Stretched Gaussian PDF $g(x;\mu,\sigma(|x-\mu|))$ with $\mu = 0$ and $\sigma(|x-\mu|) = \sqrt{|x-\mu|} = \sqrt{|x|}$.

rigidity resolution function are the normalization factor C_0, peak position μ, spline node positions of $\sigma^2(|x-\mu|)$ on the y-axis (8 nodes), and the derivatives (dy/dx) at the lower and upper boundaries. For illustration, Figure 3-21 (a) shows a Gaussian Probability Density Function (PDF) with $\mu = 0$ and $\sigma = 3$, and Figure 3-21 (b) shows a stretched Gaussian PDF with $\mu = 0$ and $\sigma(|x-\mu|) = \sqrt{|x-\mu|} = \sqrt{|x|}$.

As an example, Figure 3-22 shows the parameterization of the rigidity resolution for carbon in four different rigidity ranges. The rigidity dependence of each fitted parameter of the resolution function is then parameterized by a spline function. In this way, a continuous rigidity-dependent modelling of the resolution function is obtained.

The rigidity resolution functions have been extensively verified with the data (e.g., see Ref. [129] for protons, Ref. [116] for helium, and Ref. [83] for boron and carbon). As an example we list four verifications mainly for carbon.

1) The differences of the coordinates measured in L3 or L5 to those obtained from the track fit using the measurements from L1, L2, L4, L6, L7, and L8 (i.e., the unbiased residual distribution) were compared between data and simulation. This procedure directly measures the tracker bending coordinate accuracies of ± 10 μm for carbon and ± 11 μm for oxygen, as shown in Figure 3-23(a) and Figure 3-23(b), respectively. Similar results were obtained for the rest of the ITk layers.

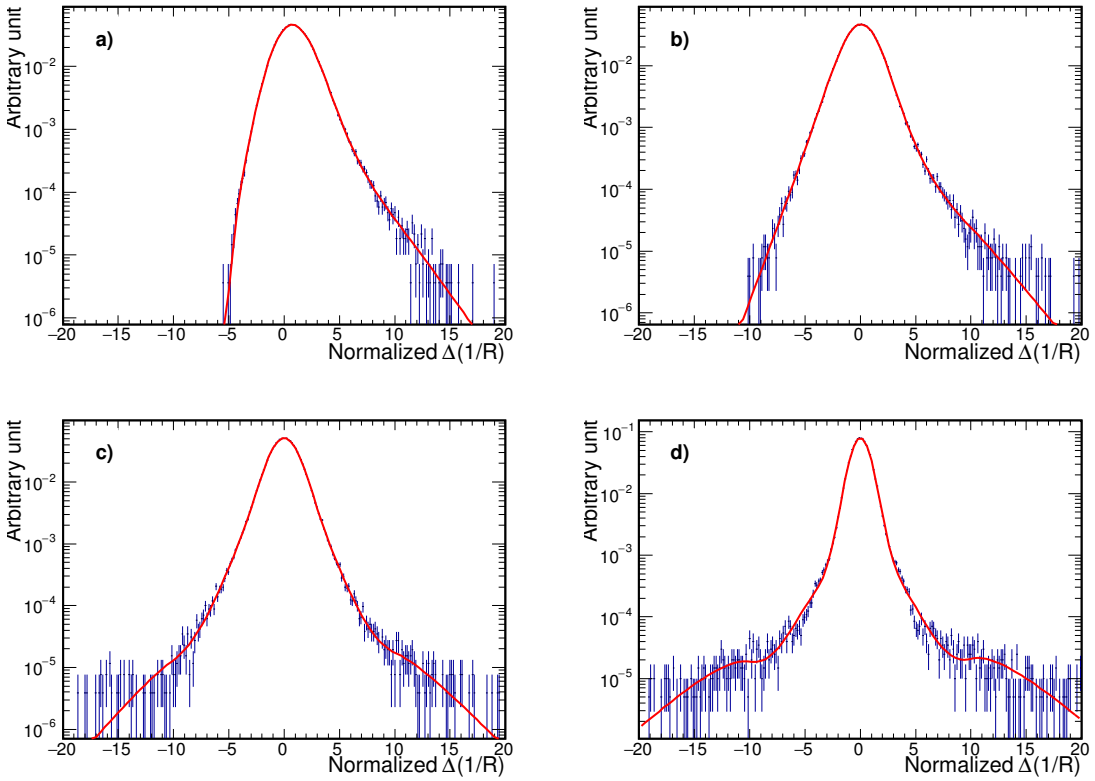

Figure 3-22: Parameterization of the rigidity resolution for carbon in four different rigidity ranges: a) 2.2–4.0 GV, b) 35–63 GV, c) 224–398 GV, and d) 1.4–2.5 TV. The observable $\Delta(1/R) = 1/R_{\mathrm{m}} - 1/R_{\mathrm{t}}$ has been normalized to a resolution scaling factor $\sqrt{p_0^2 + (p_1/R_{\mathrm{t}})^2}$ where $p_0 = 1/2000$ and $p_1 = 1/10$.

2) The unbiased residual distributions on L1 and L9 (from ITk track extrapolation) were compared between data and simulation. This comparison verifies the multiple, nucleus-nucleus elastic, and quasielastic scatterings.

3) The difference between the rigidities measured by L1–L8 and by L2–L9 was compared between data and the simulation, in order to validate the alignment of the external layers L1 and L9.

4) Along with charge identification, the velocity and rigidity give a measurement of particle mass, according to Eq. (3.7). In this work, the velocity is measured by the RICH (aerogel radiator) and the rigidity is measured by L1–L8. The

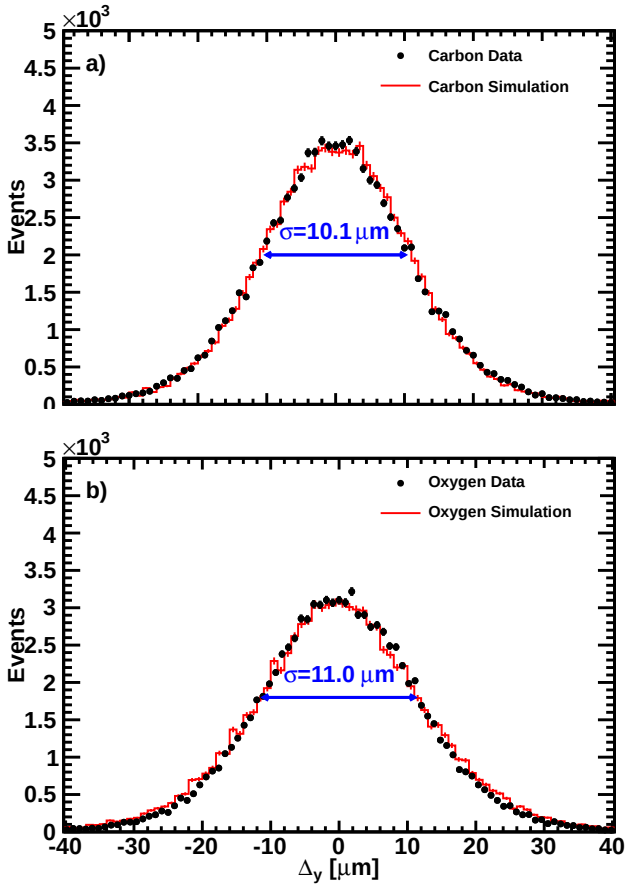

Figure 3-23: The unbiased (Y-side) residual distribution in L3 or L5 (obtained from the track fit using the measurements from L1, L2, L4, L6, L7, and L8) for data and simulation in the rigidity range 40 GV$<R<$47 GV for a) a carbon and b) an oxygen sample. The measured bending coordinate accuracy is ± 10 μm for carbon and ± 11 μm for oxygen. Courtesy of Q. Yan.

mass resolution is approximately given by:

$$\left(\frac{\Delta A}{A}\right)^2 \simeq \left(\frac{\Delta R}{R}\right)^2_{\rm MS} + \left(\frac{\Delta R}{R}\right)^2_{\rm Spec} + \left(\gamma^2 \frac{\Delta \beta}{\beta}\right)^2,$$

where the three independent contributions to the mass resolution $\Delta A/A$ are:

i) the multiple scattering of the particle along its path in the ITk,

ii) the contribution solely given by the magnetic spectrometer (i.e., the bending power of the magnet coupled with the intrinsic limits of the tracker spatial resolution),

iii) the precision of the RICH velocity measurement.

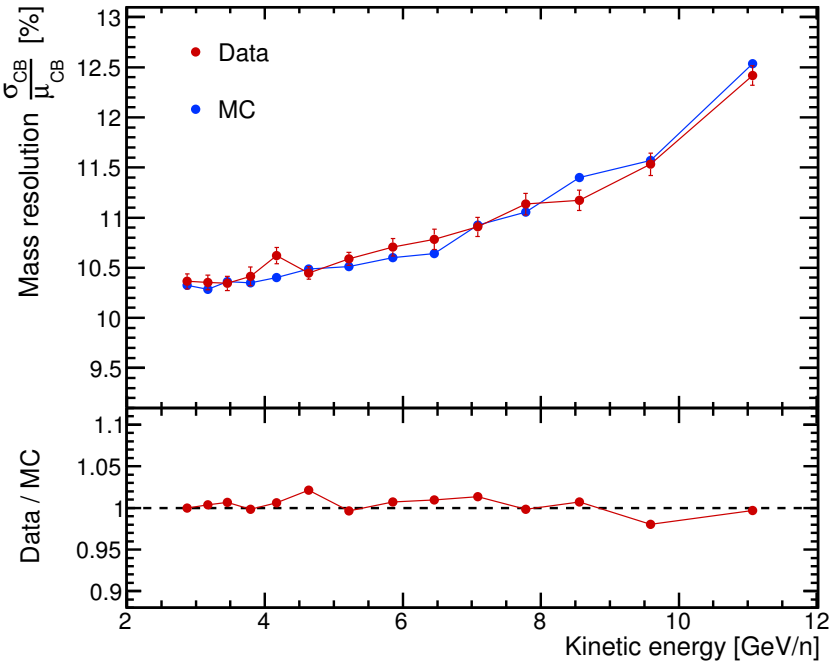

Figure 3-24: Mass resolution comparison between data and simulation for carbon in the kinetic energy per nucleon (rigidity) range from $\sim$ 3 GeV/n to $\sim$ 11 GeV/n ($\sim$ 7 GV to $\sim$ 24 GV). The mass resolution is obtained from the Gaussian width and peak of a Crystal Ball (CB) function fit, σ_{CB} and μ_{CB}. The bottom panel shows the data/MC ratio of the mass resolution. As seen the ratio is centered at 1.

The RICH velocity resolution is $\Delta\beta/\beta = 5 \times 10^{-4}$ for carbon [95]. Therefore, the mass resolution is predominantly limited by multiple scattering (affecting $\Delta R/R \sim 10\%$) up to $\sim$20 GV. Figure 3-24 shows the comparison of the mass resolution between data and simulation and a good agreement is found. This validates the multiple-scattering model in the MC simulation.

Procedures 1), 2), and 3) yield MDRs of 2.7 TV for carbon and 2.6 TV for oxygen with 5% uncertainty for this analysis; 1) and 3) verify the nucleus-nucleus elastic and quasielastic scattering in the AMS materials; 2) and 4) provide an uncertainty of 10% on the amplitudes of the non-Gaussian tails in the rigidity resolution functions.

3.3 Systematic Errors

The contributions to the systematic errors on the flux come from:

1) the trigger efficiency and the acceptance calculation,

2) the background estimation,

3) the unfolding procedure and the rigidity resolution function,

4) the absolute rigidity scale,

5) the geomagnetic cutoff factor.

3.3.1 Trigger and Acceptance

The MC samples used in this analysis have sufficient statistics (e.g., $\sim$ 17.9 billion events generated for carbon samples) such that they do not contribute to the errors. The systematic error on the effective acceptance calculation is given by the uncertainties on

1) the event reconstruction and selection (i.e., the uncertainty in the scale factor κ for each selection efficiency);

2) the inelastic cross-sections.

The uncertainty from source 1) is estimated by performing a spline fit to the pull distribution for each scale factor (summarized in Section 3.2.4). The pull in rigidity bin i is defined as

$$\frac{\kappa_{i,\text{data}} - \kappa_{i,\text{fit}}}{\sqrt{\sigma^2_{i,\text{data}} + \sigma^2_{i,\text{fit}}}},$$

where σ_{data} is the statistical uncertainty on the measured κ and σ_{fit} is the 68% CL interval of the fit to κ. As an example, Figure 3-25 shows the systematic error as a function of rigidity on the scale factor calculation for L1 hit pick-up efficiency. The same procedure is followed for the rest of the scale factors and the MC acceptance (A_0) calculations.

The uncertainty from source 2) is also estimated. We selected different samples to measure the survival probability between L8 and L9 by varying the number of ECAL layers used for the charge measurement (e.g., varying from using the first three layers to the first five). The differences between these measured survival probabilities are accounted for as a systematic error. It is then propagated to a systematic error corresponding to the survival probability between L1 and L9. The survival probability between L1 and L2 has been calculated using data collected when AMS was horizontal,

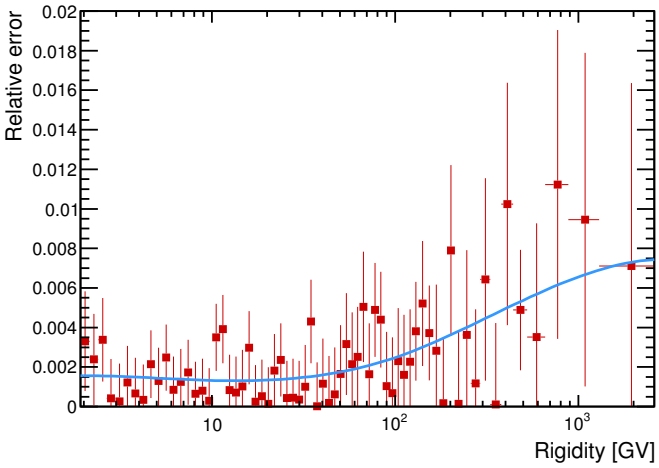

Figure 3-25: Rigidity dependence of the systematic error on the scale factor calculation for L1 hit pick-up efficiency. The blue curve shows the spline fit to the pull (red points) and represents the estimated systematic error, which reaches 0.8% at 2 TV.

i.e., $\sim 90°$ with respect to the local zenith [116]. This independently verifies the inelastic cross-sections. The systematic errors on the fluxes due to uncertainties of inelastic cross-sections were evaluated to be $< 2.2\%$ for carbon and $< 2.7\%$ for oxygen up to 100 GV. At higher rigidities, the small rigidity dependencies of the cross-sections from the Glauber-Gribov model were treated as an uncertainty and added in quadrature to the uncertainties from the measured survival probabilities. The resulting systematic errors on the fluxes were evaluated to be 3% for carbon and 3.5% for oxygen at 2.6 TV.

The contribution of individual sources are added in quadrature to arrive at the total systematic uncertainty in the acceptance calculation.

As shown in Figure 3-15, in FS analysis the trigger efficiency is practically 100% in both data and simulation, and the efficiency ratio is compatible with 1 with negligible errors from the fit. Therefore, no systematic error is assigned to the trigger efficiency due to the fact that the carbon sample is well determined and has such high efficiency in both data and simulation.

3.3.2 Background Estimation

3.3.2.1 Below L1

As discussed in Section 3.2.5, the background from interactions between L1 and L2 is evaluated by the template-fit technique with charge distribution templates obtained from non-interacting samples at L2. We perform the same procedures by using samples at L1 to evaluate the background contamination and the efficiency of the L1 purity cut, in order to estimate the systematic error associated with the uncertainty of the template shapes.

Since the charge measurement with L1 cannot be used, a selection of non-interacting samples on L1 is more challenging than that on L2. Instead of applying various tight cuts in the downstream part of the detector, a multivariate discriminant was used, in order to exploit at best the shape and correlation between the variables used to identify interactions between L1 and L2. In particular, the BDT algorithm (implementation in TMVA [150]) was used to combine all the information. The training samples, input variables, and performance in data of the fragmentation identification BDT are described in Appendix B. We selected non-interacting samples on L1 by cutting at a working point of the BDT output that gives best increase in significance $S/\sqrt{S+B}$.

Figure 3-26 shows the efficiency of L1 purity cut obtained from non-interacting samples on L1 (multivariate analysis) compared with L2 (cut-based analysis). The two measurements agree within 0.8% over the entire rigidity range.

3.3.2.2 Above L1

The systematic error associated with the background subtraction for the carbon sample is dominated by the uncertainties in the background estimation for interactions above L1, i.e., the TOI correction factor δ_{O} in Eq. (3.8). This is due to

1) the uncertainty of the fragmentation partial cross-sections $\mathrm{O}+\mathrm{C},\mathrm{Al}\rightarrow\mathrm{C}+\mathrm{X}$ used in the simulation;
2) the uncertainty of the $\Phi_{\mathrm{O}}/\Phi'_{\mathrm{C}}$ ratio.

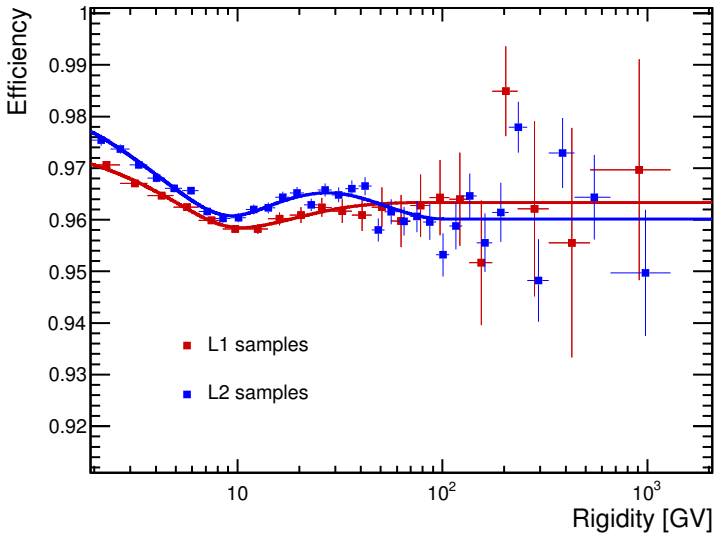

Figure 3-26: Efficiency of the charge selections on L1 for carbon, estimated from non-interacting samples on L1 (red squares) compared with L2 (blue squares) and parameterized by a spline function (red curve for L1 and blue curve for L2).

The first one is estimated by comparing the difference between two ratios, i.e., the data-to-simulation ratios of the probability of oxygen fragmenting to carbon between a) L8 and L9 and b) L1 and L2 (which has a similar amount of material as between L8 and L9). This comparison also takes into account the uncertainty due to the different kinematics in these two samples. The rigidities of particles in sample 1) are measured before spallations by L1–L8 (MDR $\sim$ 1.2 TV) and in sample 2) after spallations by the ITk (L2–L8, MDR $\sim$ 550 GV). Figure 3-27 shows the TOI correction factor δ_{O} with its systematic uncertainty as a function of rigidity.

The total background subtraction error on the carbon flux is $< 0.5\%$ over the entire rigidity range.

3.3.3 Unfolding

The two main sources of systematic uncertainty on the unfolding are the unfolding procedure and the rigidity resolution function.

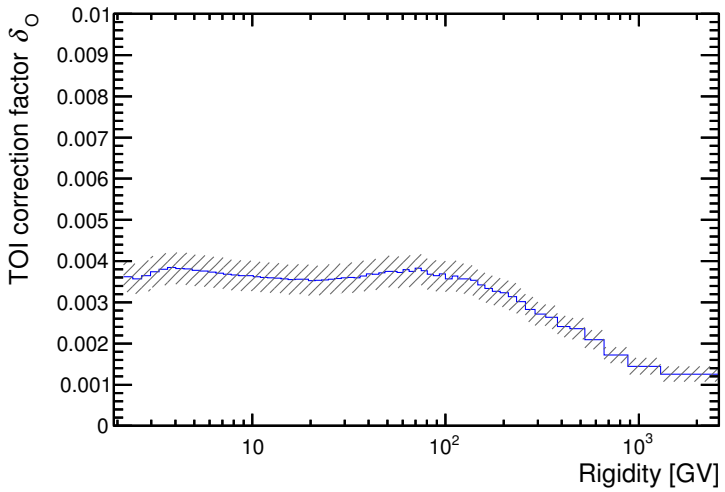

Figure 3-27: The TOI correction factor for the carbon flux as a function of rigidity. The hatched bands represent the corresponding systematic uncertainty.

3.3.3.1 Unfolding Procedure

As discussed in Section 3.2.6, we used two different unfolding procedures (FAM and FUM) in this analysis. The differences of the unfolding factors between these two methods are accounted for as a systematic error, as shown in Figure 3-28(a).

3.3.3.2 Rigidity Resolution Function

The systematic error on the fluxes due to the rigidity resolution functions is obtained by repeating the unfolding procedure for both carbon and oxygen while varying the widths of the Gaussian core of the resolution functions by 5% and by independently varying the amplitudes of the non-Gaussian tails by 10%. Figure 3-28(b) shows the ratios of fluxes obtained by varying the resolution function of carbon.

The contributions of the two sources discussed above are added in quadrature and the resulting systematic error on the fluxes is less than 1% below 300 GV and is 4% at 2.6 TV for both carbon and oxygen.

3.3.4 Absolute Rigidity Scale

There are two sources of systematic uncertainty on the rigidity scale [83, 116, 129].

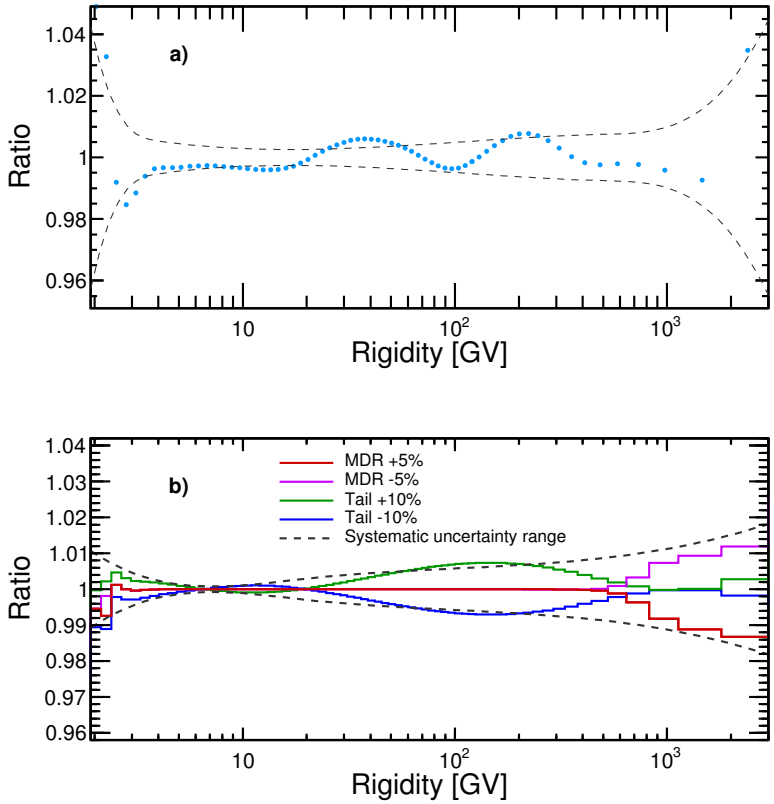

Figure 3-28: a) Ratio of the unfolding factors obtained from FUM over FAM for carbon (blue circles). b) Ratios of the fluxes obtained by varying the resolution function of carbon (red and magenta: ±5% width of the Gaussian core; green and blue: ±10% amplitudes of the non-Gaussian tails). The dashed curves indicate the corresponding systematic errors.

The first is due to residual tracker misalignment. This error is estimated from the ISS data by comparing the $1/|R| - 1/E$ distribution for positrons and electrons, where E is the energy measured by the ECAL and R is the rigidity measured by the tracker. It is found to be $\pm 30^{-1}$ TV^{-1} [152] based on the data collected during the first 5 years of operation[1], still limited by the current high-energy positron statistics. Figure 3-29 shows the measured $\delta_s^{e^+}$ as a function of data collection time. $\delta_s^{e^+}$ is

[1]With 5 years of data we are able to improve the estimation of residual time dependent tracker misalignment and the tracker rigidity scale estimation, compared to rigidity scale uncertainty quoted in the previous AMS publications [116, 129, 151]. The details of these improvements are published in Ref. [152].

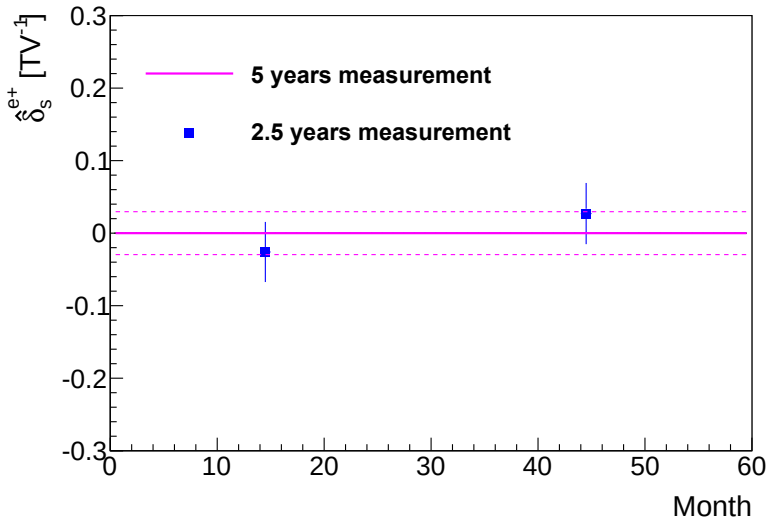

Figure 3-29: Residual tracker misalignment estimate as a funciton of data collection time. The solid line represents the measurement based on 5 years e^+ and e^- data. The two squares represent the measurement based on the first and the second 2.5 years data, respectively. The dashed lines indicate the corresponding systematic error. Courtesy of Q. Yan [152].

defined as [152]

$$2\,\delta_{\rm s}^{e^+} = \delta_{\rm s}^{e^+} - \delta_{\rm s}^{e^-} = \left\langle \frac{1}{|R_{\rm s}^{e^+}|} - \frac{1}{E^{e^+}} \right\rangle - \left\langle \frac{1}{|R_{\rm s}^{e^-}|} - \frac{1}{E^{e^-}} \right\rangle,$$

where $R_{\rm s}^{e^+}$ and E^{e^+} are the rigidity measured with the tracker and the energy measured with the ECAL for positrons, respectively; $R_{\rm s}^{e^-}$ and E^{e^-} for electrons; $\delta_{\rm s}^{e^+} = 1/|R_{\rm s}^{e^+}| - 1/E^{e^+}$ is the absolute rigidity scale bias for positrons; $\delta_{\rm s}^{e^-} = 1/|R_{\rm s}^{e^-}| - 1/E^{e^-}$ for electrons. The second systematic error arises from the uncertainties on the mapping of the magnetic field (0.25%) and its temperature corrections (0.1%) [129].

The error on the carbon and oxygen fluxes due to uncertainty on the rigidity scale is derived by modifying the carbon and oxygen rigidity scales for alignment and magnetic field estimated uncertainties, i.e., $R^{-1} \pm 30^{-1}$ TV^{-1} and $R \cdot (1 \pm 0.27\%)$, and is found to be $< 0.6\%$ up to 100 GV and reaching 6% at 2.6 TV.

3.3.4.1 Geomagnetic Cutoff Factor

The geomagnetic cutoff factor was varied from 1.0 to 1.4, resulting in a negligible systematic uncertainty ($< 0.1\%$) in the relevant rigidity range (< 30 GV).

3.4 Verification of Systematic Errors

An additional verification, i.e., the IL1 analysis, was performed from 2.2 GV to 0.88 TV (MDR for tracker L1 to L8) to ensure that the treatment of systematic errors is correct.

3.4.1 Flux Measurement Using L1 to L8

In the IL1 analysis, the event selections are different from those in the FS analysis:

1) events are required to pass through L1 to L8 (instead of L1 to L9);
2) no cut on the lower TOF charge;
3) no L9-related cut;
4) an additional track fitting quality criterion to remove hard-scattered (between L1 and L2) events, $\chi^2_{y,\mathrm{L1}}/\mathrm{d.f.} < 10$ where $\chi^2_{y,\mathrm{L1}} \equiv \chi^2_{y,\mathrm{L1–L8}} - \chi^2_{y,\mathrm{L2–L8}}$.

The resulting acceptance in the IL1 analysis, as shown in Figure 3-30, is about five times larger than that in the FS analysis due to the larger geometric acceptance and the higher survival probability (less amount of material traversed).

The same procedures as in the FS analysis are followed for the IL1 analysis in the acceptance calculation, the efficiency scale factors calculations, the background subtractions (below and above L1), and the unfolding. The estimations of systematic errors are also performed for the IL1 analysis in the same procedure.

Figure 3-31 shows the ratio of two measurements of the carbon flux from 2.2 GV to 0.88 TV performed using events passing through L1 to L9 (FS analysis) and using events passing through L1 to L8 (IL1 analysis). The statistical uncertainties are the quadratic sum of the statistical uncertainties of the L1–L9 and L1–L8 fluxes. There ought to be correlation between the L1–L9 and L1–8 samples because the events se-

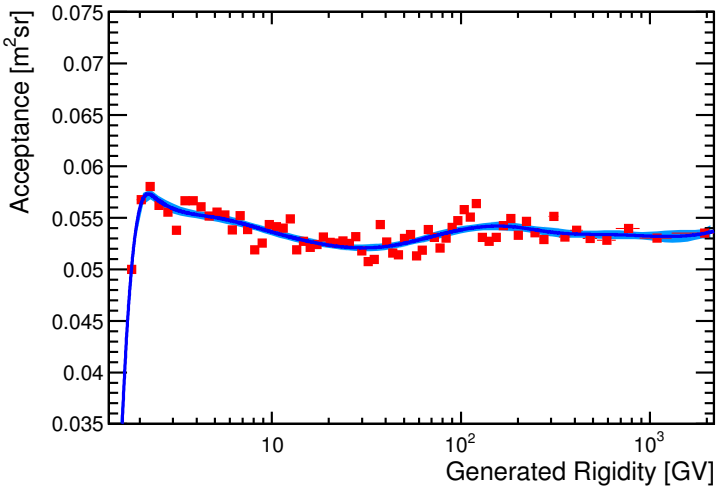

Figure 3-30: The carbon acceptance in the IL1 analysis as a function of generated rigidity before applying data-driven corrections (red squares). The blue curve shows the spline fit to the acceptance and the blue band represents the confidence interval of the fitted function at 68% CL.

lected in the FS analysis also pass the selections of the IL1 analysis. This overlap is negligible since the effective acceptance in the FS analysis is about five times larger than that in the IL1 analysis. The systematic uncertainties from the background subtraction, the trigger, and the event reconstruction and selection are also added in quadrature. The correlations in the systematic uncertainties from the nuclear interaction cross-sections (due to the grammage of detector material in the simulation), the unfolding (due to the resolution functions), and the absolute rigidity scale between the two measurements have been accounted in calculating the corresponding systematic uncertainties.

The good agreement between the two measurements verifies the systematic errors on a) the unfolding, due to the difference in the rigidity resolution functions and b) the acceptance, due to the differences in the geometric factor and the amount of material traversed.

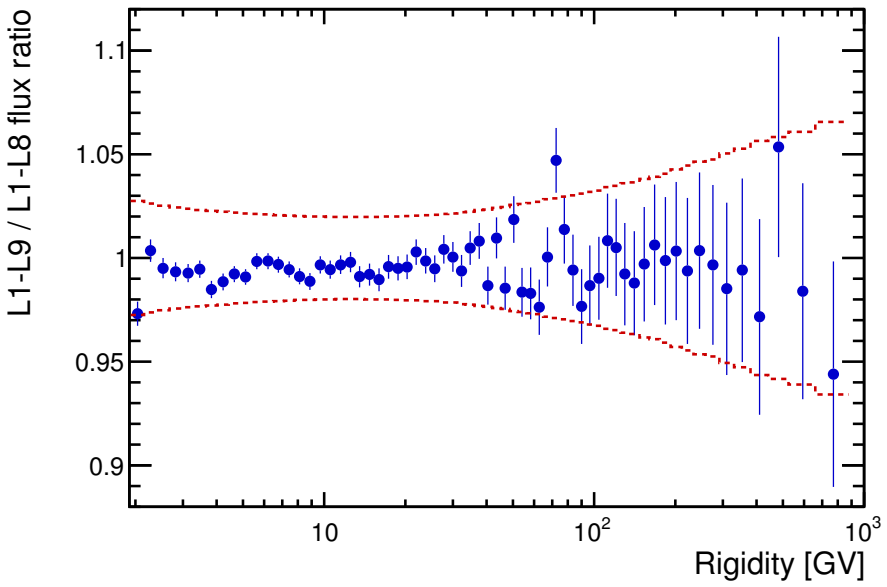

Figure 3-31: The ratio of the carbon flux measured using events passing through L1 to L9 over the flux using events passing through L1 to L8. The error bars show the statistical uncertainty, and the dashed lines show the sum in quadrature of statistical and systematic uncertainties.

3.5 Results

We use the result from the IL1 analysis up to 0.88 TV (the MDR for tracker L1–L8). In the highest rigidity region, $R \geq 1.2$ TV, the result from the FS analysis is used.

The measured carbon and oxygen fluxes including statistical and systematic errors are shown in Figures 3-32 and 3-34, respectively, as functions of the rigidity at the top of the AMS detector. In these figures, the points are placed along the abscissa at $\tilde{R}$ calculated for a flux $\propto R^{-2.7}$ [135]. Figure 3-33 shows the breakdown of the total errors for the carbon flux. The statistical errors on the flux, $\sigma_{\text{stat}} = \sqrt{\aleph}/N$, are conservative at high rigidities where $\aleph > N$.

To examine the rigidity dependence of the fluxes, detailed variation of the fluxes spectral indices (γ) with rigidity is obtained in a model independent way. The fluxes spectral indices are calculated from

$$\gamma = d[\log(\Phi)]/d[\log(R)]$$

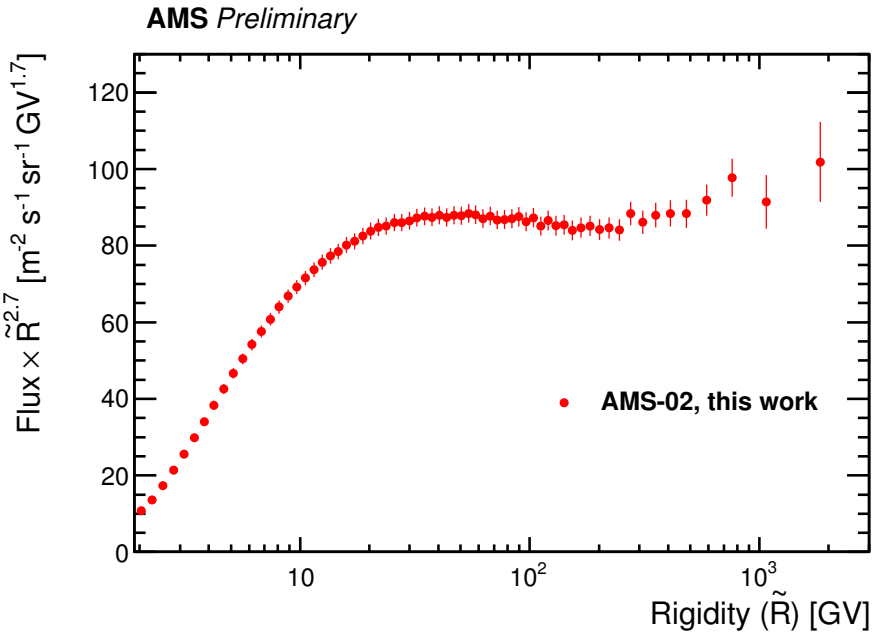

Figure 3-32: The AMS carbon flux multiplied by $\tilde{R}^{2.7}$ with the total errors as a function of rigidity from 1.9 GV to 2.6 TV based on 8.3 million carbon nuclei. The indicated error is the quadratic sum of the statistical and systematic errors.

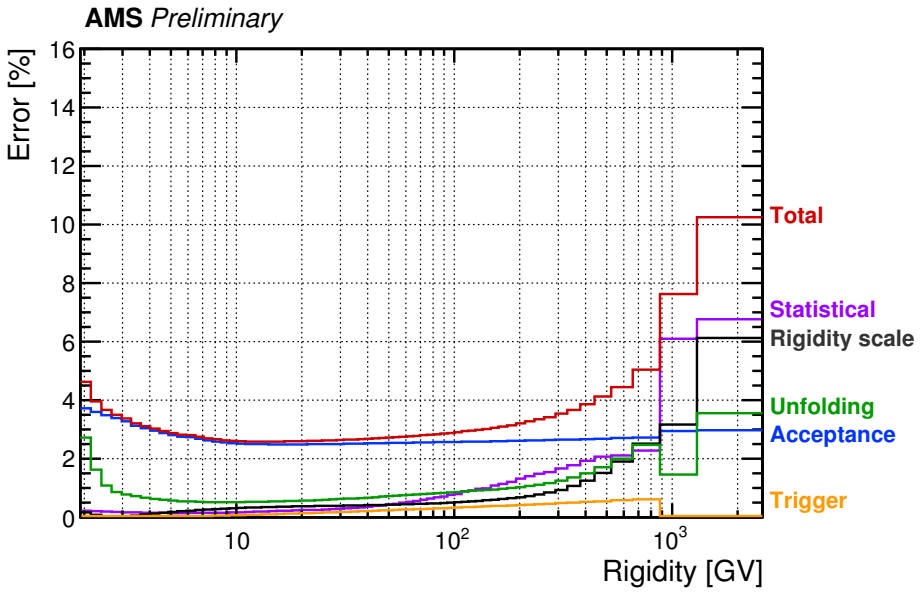

Figure 3-33: Breakdown of the total errors on the carbon flux. The text on the right margin indicates the corresponding error category. The error from the geomagnetic cutoff factor is small ($< 0.1\%$) and not shown in this figure. The errors from background subtractions are included in the acceptance category in this figure.

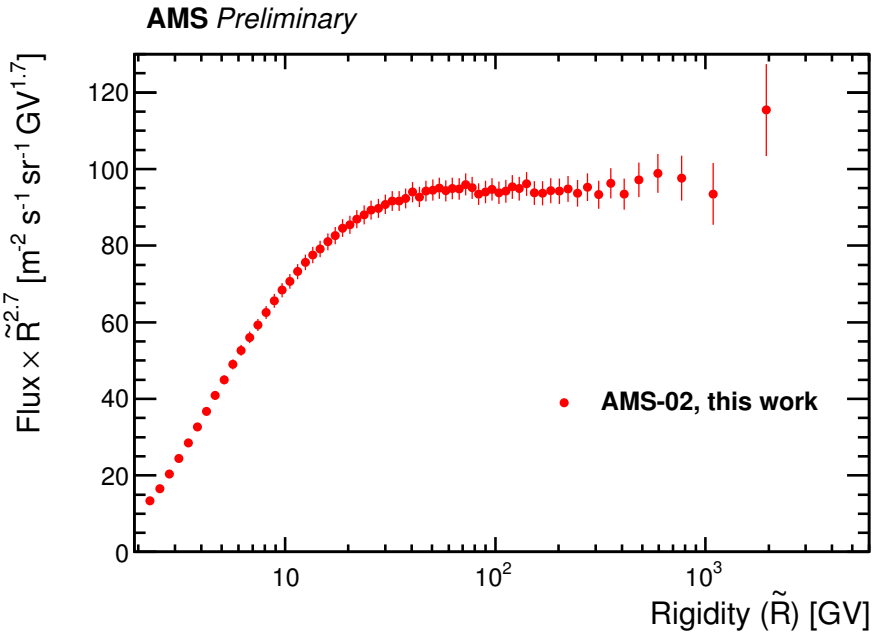

Figure 3-34: The AMS oxygen flux multiplied by $\tilde{R}^{2.7}$ with the total errors as a function of rigidity from 2.2 GV to 2.6 TV based on 7.4 million oxygen nuclei. The indicated error is the quadratic sum of the statistical and systematic errors.

over non-overlapping rigidity intervals above 8.48 GV, with a variable width to have sufficient sensitivity to determine γ. The results of this fitting procedure on the carbon and oxygen fluxes are shown in Figure 3-35. The indicated error of each spectral index is the quadratic sum of two components. First, in the fitting procedure we take into account the statistical and uncorrelated systematic errors from the flux. Second, we repeat the fitting procedure by varying the flux by $\pm\sigma_{\text{corr.}}$ where $\sigma_{\text{corr.}}$ is the error from the remaining systematic uncertainties whose bin-to-bin correlations need to be properly accounted; namely, from the uncertainties in the inelastic cross-sections, the rigidity resolution function and unfolding, and the absolute rigidity scale.

As seen in Figure 3-35, the *magnitude* and *rigidity dependence* of the carbon and oxygen fluxes spectral indices are very similar:

1) their spectral indices are identical within the measurement errors above 60 GV;
2) the fluxes deviate from a single power law and their spectral indices progressively harden at high rigidities (above $\sim$ 200 GV).

To examine the difference between the rigidity dependence of the carbon and oxy-

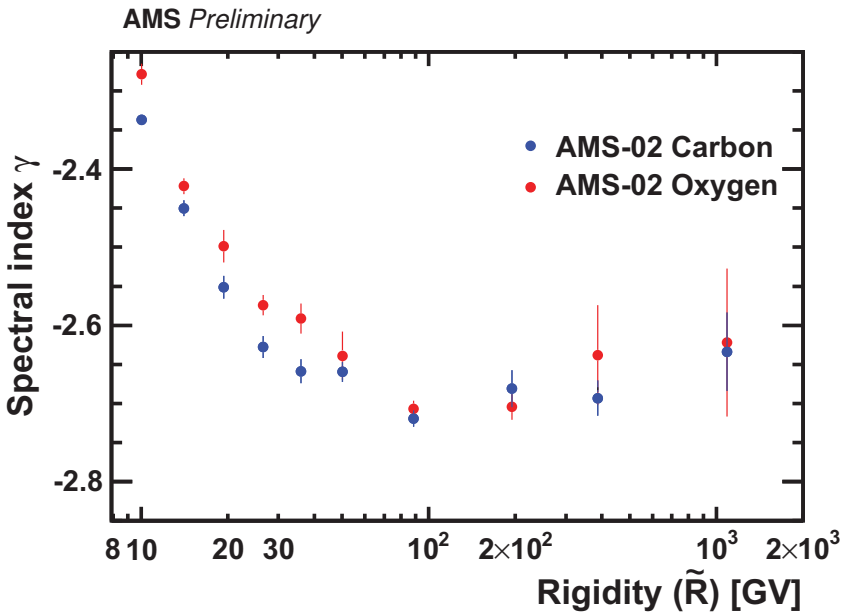

Figure 3-35: The rigidity dependence of the carbon (blue circles) and oxygen (red circles) fluxes spectral indices. As seen, above 60 GV the spectral indices are identical.

gen fluxes in detail, the C/O ratio was computed. Figure 3-36 shows the C/O ratio with total errors, the quadratic sum of statistical and systematic errors. The statistical errors are the quadratic sum of the statistical errors of the carbon and oxygen fluxes. The systematic errors from the background estimation, the trigger efficiency, and the event reconstruction and selection are also added in quadrature. The correlations in the systematic errors from the uncertainties in the inelastic cross-secitons, the rigidity resolution function and unfolding, and the absolute rigidity scale between the carbon and oxygen fluxes have been accounted for in calculating the corresponding systematic errors of the C/O ratio. The contribution of individual sources to the systematic error are added in quadrature to arrive at the total systematic uncertainty on the C/O ratio.

As seen in Figure 3-36, above 60 GV the C/O ratio measured by AMS is well described by a zeroth-order polynomial, which yields a constant value of 0.93 ± 0.02 with $\chi^2/\text{d.f.} = 13/26$.

Whereas protons, helium, carbon, and oxygen are all considered primary cosmic rays, the rigidity independence of the measured C/O ratio is completely different from

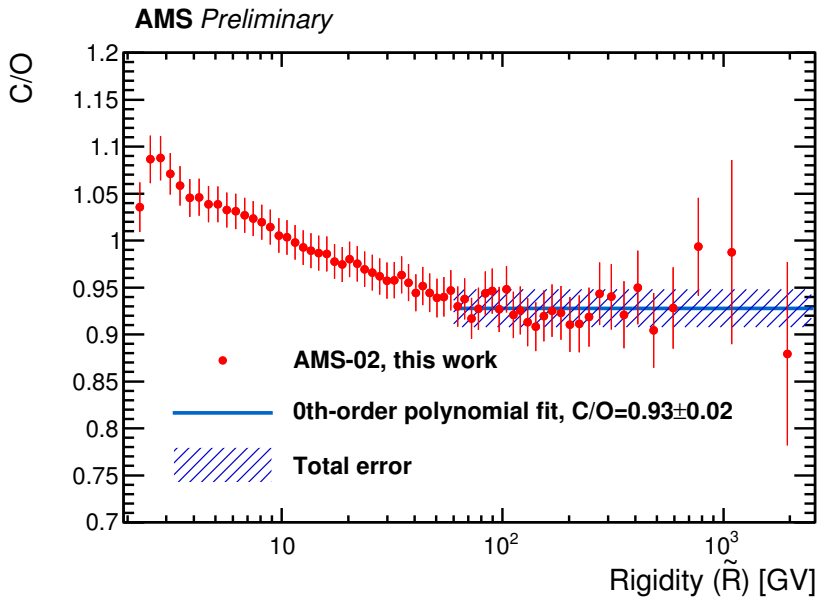

Figure 3-36: The AMS C/O ratio as a function of rigidity. The error bars on the data points indicate the quadratic sum of the statistical and systematic errors. The solid line indicates a fit of a zeroth-order polynomial to the C/O ratio above 60 GV with the hatched area its total error, which yields a constant value of 0.93 ± 0.02 with $\chi^2/\text{d.f.} = 13/26$.

p/He ratio rigidity dependence (the p/He ratio is well described by a single power law above 45 GV), see Figure 2(b) of Ref. [116].

Chapter 4

Measurement of the Helium Isotopic Composition

The isotopic compositions of light nuclei in CRs directly reflect processes related to the propagation of CRs in the galaxy. The measurement of the isotopic compositions of CR nuclei is one of the alternatives to the B/C ratio [153]. Helium nuclei are the second most abundant elements in CRs and their isotopic composition has a better statistics compared to the B/C ratio, though the mass separation power required for isotopes identification is experimentally difficult to achieve for energies above 10 GeV/n. As ^{3}He is assumed to be produced by interactions of heavier nuclei with the ISM, the ^{3}He to ^{4}He flux (^{3}He/^{4}He) ratio, is a powerful tool for determining the amount of ISM traversed by CRs. Therefore, knowledge of the energy dependence of the ^{3}He/^{4}He ratio is important in understanding the propagation of galactic CRs. This chapter discusses a preliminary analysis of the AMS ^{3}He/^{4}He ratio.

4.1 Event Selection and Data Samples

Data collected by AMS in the first 5 years of operation onboard the ISS are used for this measurement, the same sample as for the carbon and oxygen fluxes measurements discussed in Chapter 3. The measurement of the ^{3}He/^{4}He ratio discussed in this chapter is based on 9 million ^{3}He events and 56 million ^{4}He events from 0.7 GeV/n

to 10 GeV/n.

The event selection mainly refers to the AMS helium flux analysis [116]. The major differences of the selection in this analysis include:

1) the track is required to pass through L1 and L8 (i.e., IL1 geometry), to increase the acceptance;

2) RICH β reconstruction quality cuts are required. For example, at least 5 (4) hits on the photodetection plane are required for the reconstruction of the Čerenkov ring produced through the aerogel (NaF) radiator.

4.2 ^{3}He to ^{4}He Flux Ratio

The ^{3}He/^{4}He ratio in each kinetic energy per nucleon bin is given by

$$\left(\frac{^3\mathrm{He}}{^4\mathrm{He}}\right)_i = \frac{\Phi_i^{^3\mathrm{He}}}{\Phi_i^{^4\mathrm{He}}} = \frac{N_i^{^3\mathrm{He}}}{N_i^{^4\mathrm{He}}}\left(\frac{A_i^{^3\mathrm{He}}}{A_i^{^4\mathrm{He}}}\right)^{-1} = \frac{N_i^{^3\mathrm{He}}}{N_i^{^4\mathrm{He}}}\left(\frac{A_{i,\mathrm{MC}}^{^3\mathrm{He}}}{A_{i,\mathrm{MC}}^{^4\mathrm{He}}}\frac{\kappa_i^{^3\mathrm{He}}}{\kappa_i^{^4\mathrm{He}}}\right)^{-1}. \tag{4.1}$$

The determinations of the ^{3}He/^{4}He event counts ratio ($N_i^{^3\mathrm{He}}/N_i^{^4\mathrm{He}}$) and the MC acceptance asymmetry ($A_{i,\mathrm{MC}}^{^3\mathrm{He}}/A_{i,\mathrm{MC}}^{^4\mathrm{He}}$) are discussed in this section. The data-driven determination of the scale factor ratio on the MC acceptance ($\kappa_i^{^3\mathrm{He}}/\kappa_i^{^4\mathrm{He}}$) is missing in this preliminary analysis, i.e., the discrepancies between data and simulation in efficiencies are assumed to be the same for ^{3}He and ^{4}He.

4.2.1 Measurement Strategy

The RICH provides particle velocity measurements with a resolution better than 0.1% as described in Section 2.1.7. The silicon tracker provides rigidity determination through the measurement of the charged particle trajectory in the magnetic field. Along with the charge identification, the velocity and rigidity give a measurement of the particle mass, as already given by Eq. (3.7). We rearrange Eq. (3.7) so that the mass is on the left hand side:

$$A = \frac{RZ}{m_\mathrm{n}\beta}\sqrt{1-\beta^2} \tag{4.2}$$

The mass is reconstructed by the measurements of the rigidity and charge with the tracker L1–L8, the velocity with the RICH. Limited by the mass resolution, this measurement is only up to $\sim$ 10 GeV/n. In this energy range, L9 is not needed for the rigidity measurement. The ^{3}He/^{4}He ratio can be measured by fitting the mass distribution after selecting events with charge compatible with $Z = 2$.

Distributions for A were obtained from data for different β_{RICH} bins. The β_{RICH} bins were then converted to kinetic energy per nucleon E_{k} bins according to Eq. (4.3):

$$E_{\mathrm{k}} = \left(\frac{1}{\sqrt{1-\beta_{\mathrm{RICH}}^2}} - 1 \right) m_{\mathrm{n}}. \tag{4.3}$$

To select only primary CRs, the measured β is required to be greater than the maximum β cutoff, $\beta_{\mathrm{c,max}}$, which is converted from the maximum geomagnetic rigidity cutoff (within the AMS field of view) times a safety factor of 1.2. According to Eq.(4.2), the cutoff rigidity can be converted to the β threshold which is inversely proportional to the particle mass, and $\beta_{\mathrm{c,max}}$ is different for ^{3}He and ^{4}He ($\beta_{\mathrm{c,max}}^{^3\mathrm{He}} > \beta_{\mathrm{c,max}}^{^4\mathrm{He}}$) due to the different masses of these two isotopes. Therefore, we require the measured $\beta > \max\left(\beta_{\mathrm{c,max}}^{^3\mathrm{He}}, \beta_{\mathrm{c,max}}^{^4\mathrm{He}}\right) = \beta_{\mathrm{c,max}}^{^3\mathrm{He}}$ to ensure that both ^{3}He and ^{4}He are above the geomagnetic cutoff.

4.2.2 Extraction of ^{3}He/^{4}He Event Counts Ratio

The determination of the helium isotopic composition is based on a template fit to the mass distribution in data. The mass distributions were obtained separately for ^{3}He and ^{4}He from MC simulations and were used to perform a template fit to the mass distributions in data. Specifically, a hypothetical probability density distribution for the mass , dP/dA, is formed assuming that a fraction, f_3 (f_4), of the measured $Z = 2$ particles is ^{3}He (^{4}He). The probability density distribution for the mass is formed

$$\frac{dP}{dA} = f_3 \left.\frac{dP}{dA}\right|_{^3\mathrm{He}} + f_4 \left.\frac{dP}{dA}\right|_{^4\mathrm{He}},$$

where $f_3 + f_4 = 1$.

The fits allow for limited adaptation of the MC templates to the data [154], in order to account for possible differences in the mass distribution between data and simulation due to e.g., inaccuracies in the MC description of multiple scattering or absolute β scale. In particular, the fit allows a shift and re-scaling of the mass distribution, $A' = a + \langle A \rangle + b(A - \langle A \rangle)$, where $\langle A \rangle$ is the mean of the mass distribution. In addition, a Gaussian smearing of the MC mass distribution was included such that the data mass distribution was fit to

$$\frac{dP'}{dA'} \equiv \left[f_3 \left. \frac{dP}{dA'} \right|_{^3\mathrm{He}} + (1 - f_3) \left. \frac{dP}{dA'} \right|_{^4\mathrm{He}} \right] \otimes \frac{e^{-A'^2/2\sigma^2}}{\sqrt{2\pi}\sigma}. \tag{4.4}$$

The shift, re-scaling, and smearing parameters for the ^{3}He template are assumed to be the same as those for ^{4}He template.

The ^{3}He fraction, f_3, was then evaluated for each β_{RICH} bin using binned maximum likelihood fits with four free parameters, f_3, a, b, and σ. The fits were performed using MINUIT [155] as implemented in `RooFit` [156]. Figure 4-1(a) and 4-1(b) show examples of the resulting template fits in kinetic energy per nucleon intervals for the aerogel and NaF radiator, respectively. The combination of the MC ^{3}He and ^{4}He mass distributions are found to describe well the measured mass distributions. The ^{3}He/^{4}He event counts ratio is then given by $N_i^{^3\mathrm{He}}/N_i^{^4\mathrm{He}} = f_3/(1 - f_3)$. Typical fitted values for the a, b, and σ parameters in Eq.(4.4) are, $a \sim 0$ to 0.4, $b \sim 1$ to 1.01, and $\sigma \sim 0.04$ to 0.08, as shown in Figures C-1, C-2, and C-3, respectively.

4.2.3 Statistical Errors

The statistical uncertainties on $N_i^{^3\mathrm{He}}/N_i^{^4\mathrm{He}} = f_3/(1 - f_3)$ from the fits represent 1σ confidence intervals that account for limited statistics in data mass distributions and correlations between the fit parameters.

The uncertainties in the fit results due to the finite statistics in the MC simulations were evaluated by re-sampling the MC mass distributions. The resulting pseudo-MC distributions were then used to perform template fits. This procedure was repeated eight times for each E_{k} bin. The standard deviation of the resulting $N_i^{^3\mathrm{He}}/N_i^{^4\mathrm{He}}$ ratio

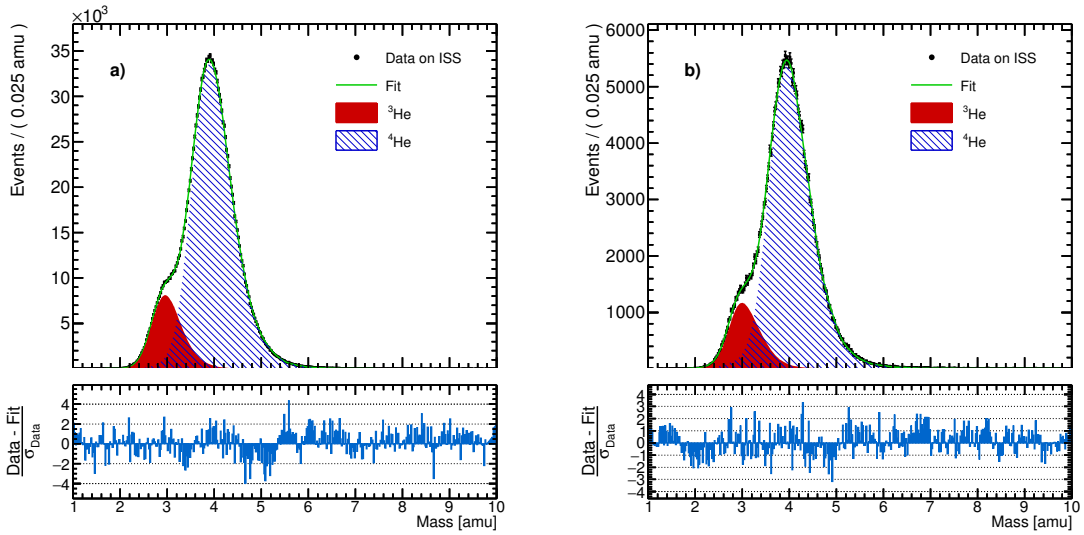

Figure 4-1: Examples of the template fits (solid green lines) to the measured mass distributions (solid circles) in the kinetic energy per nucleon intervals of a) 5.6–6.0 GeV/n for the aerogel radiator and b) 0.9–1.0 GeV/n for the NaF radiator. The filled (hatched) areas show the contributions of the ^{3}He (^{4}He) based on the corresponding mass distributions obtained from MC simulations including the shift, re-scaling, and smearing modifications. Each lower panel shows the significance per bin of the data with respect to the fit, in terms of the number of standard deviations, considering only the statistical fluctuations.

values in each bin was combined in quadrature with the statistical uncertainty from the original fit to produce a combined statistical uncertainty on the $N_i^{^3\mathrm{He}}/N_i^{^4\mathrm{He}}$ ratio.

The fractional uncertainties on the ^{3}He/^{4}He ratio due to the finite statistics of the MC samples are found to be below 1% (2%) for the aerogel (NaF) radiator.

4.2.4 Systematic Errors

There are five sources of systematic uncertainties:

1) template fitting procedure;

2) potential data-MC mismatches in the template;

3) effective acceptance (i.e., efficiencies and interactions) correction;

4) bin-to-bin migration;

5) absolute β (or E_k) scale.

In this stage of the analysis, only the contributions from sources 1) and 2) have been studied, as discussed below.

4.2.4.1 Systematic Uncertainty on the Fitting Procedure

Potential systematic uncertainties resulting from the template fitting procedure were evaluated using a simple cut procedure applied to the mass distributions. For a given E_{k} bin, a cut was applied at a chosen value of the mass, A_{cut}, and the fraction of helium nuclei in the data (after selecting particles with charge compatible with $Z = 2$) above the cut, $f^{>}$, was calculated: $f^{>} = N^{>}_{\mathrm{cut}}/N_{\mathrm{total}}$, where $N^{>}_{\mathrm{total}}$ is the total number of $Z = 2$ particles and $N^{>}_{\mathrm{cut}}$ is the number of $Z = 2$ particles with measured masses above A_{cut}.

The ^{4}He and ^{3}He mass distributions obtained from MC simulations were used to evaluate the fraction of the ^{4}He and ^{3}He above the cut, $f^{>}_{^4\mathrm{He}}$ and $f^{>}_{^3\mathrm{He}}$. Then, the event counts ratio $N_{^3\mathrm{He}}/N_{^4\mathrm{He}}$ evaluated using this cut method was estimated:

$$\left.\begin{aligned} N_{\mathrm{total}} &= N_{^4\mathrm{He}} + N_{^3\mathrm{He}}, \\ N^{>}_{\mathrm{cut}} &= f^{>}_{^4\mathrm{He}} \cdot N_{^4\mathrm{He}} + f^{>}_{^3\mathrm{He}} \cdot N_{^3\mathrm{He}}, \\ f^{>} &= N^{>}_{\mathrm{cut}}/N_{\mathrm{total}}, \end{aligned}\right\} \Rightarrow \frac{N_{^3\mathrm{He}}}{N_{^4\mathrm{He}}} = \frac{f^{>}_{^4\mathrm{He}} - f^{>}}{f^{>} - f^{>}_{^3\mathrm{He}}}. \tag{4.5}$$

The relative differences of these two different estimates (fit- and cut-based) of the $N_{^3\mathrm{He}}/N_{^4\mathrm{He}}$ ratio were used to establish systematic uncertainties associated with the template fitting procedure, as shown in Figure 4-2.

4.2.4.2 Systematic Uncertainty on Data-MC Template Mismatches

Clean ^{4}He event samples can be obtained directly from data in the Earth's penumbral region where the criteria $\beta^{^4\mathrm{He}}_{\mathrm{c,max}} < \beta < \beta^{^3\mathrm{He}}_{\mathrm{c,min}}$ is fulfilled. The geomagnetic field has been used to filter the heavier isotope in data [157]. When two isotopes impinge the geomagnetic field at the same velocity, the heavier isotope has a higher rigidity and thus penetrates deeper into the geomagnetic cavity and reaches the AMS detector. In this penumbral region, most of the $Z = 2$ particles are primary ^{4}He, as primary

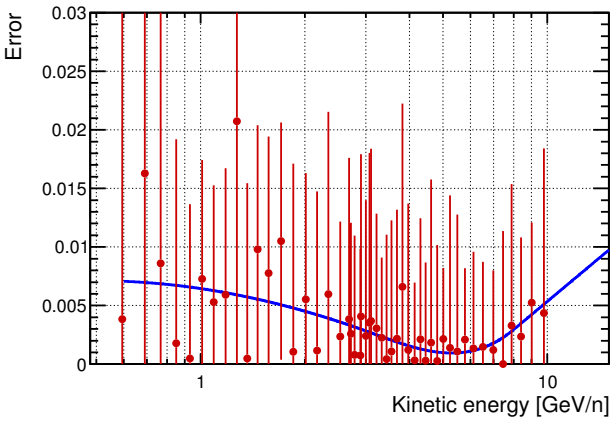

Figure 4-2: Systematic errors from the fitting procedure as a function of kinetic energy per nucleon. The solid circles show the relative differences between the results of the fit- and cut-based approaches. Error bars are statistical. The blue curve shows the spline fit to the relative errors.

^{3}He are suppressed by the cutoff, plus a small amount of secondary ^{3}He. This allows us to obtain relatively clean ^{4}He mass templates. A safety factor, or SF, of 1.1 (0.9) on the maximum (minimum) geomagnetic rigidity cutoff was used when calculating the lower (upper) β threshold of the penumbral region $\beta^{^4\mathrm{He}}_{\mathrm{c,max}}$ ($\beta^{^3\mathrm{He}}_{\mathrm{c,min}}$). That is,

$$\beta^{^4\mathrm{He}}_{\mathrm{c,max}} = \left[\left(\frac{A_{^4\mathrm{He}} \cdot m_{\mathrm{n}}}{SF_{^4\mathrm{He}} \cdot R_{\mathrm{c,max}} \cdot Z} \right)^2 + 1 \right]^{-\frac{1}{2}}, \tag{4.6}$$

$$\beta^{^3\mathrm{He}}_{\mathrm{c,min}} = \left[\left(\frac{A_{^3\mathrm{He}} \cdot m_{\mathrm{n}}}{SF_{^3\mathrm{He}} \cdot R_{\mathrm{c,min}} \cdot Z} \right)^2 + 1 \right]^{-\frac{1}{2}}, \tag{4.7}$$

where $SF_{^4\mathrm{He}} = 1.1$ and $SF_{^3\mathrm{He}} = 0.9$.

The comparisons of ^{4}He mass templates between data and simulation are shown in Figures 4-3(a) and 4-3(b) for the aerogel and NaF radiator, respectively. The contamination from primary and secondary ^{3}He (due to the limited accuracy of determining the thresholds for the penumbral region) in the ^{4}He samples can also be seen in Figure 4-3(b). This impurity was estimated by using ^{3}He and ^{4}He mass distributions obtained from MC simulations. Figures 4-4(a) and 4-4(b) show the purities of the ^{4}He data samples as a function of kinetic energy per nucleon for the aerogel and NaF radiator, respectively.

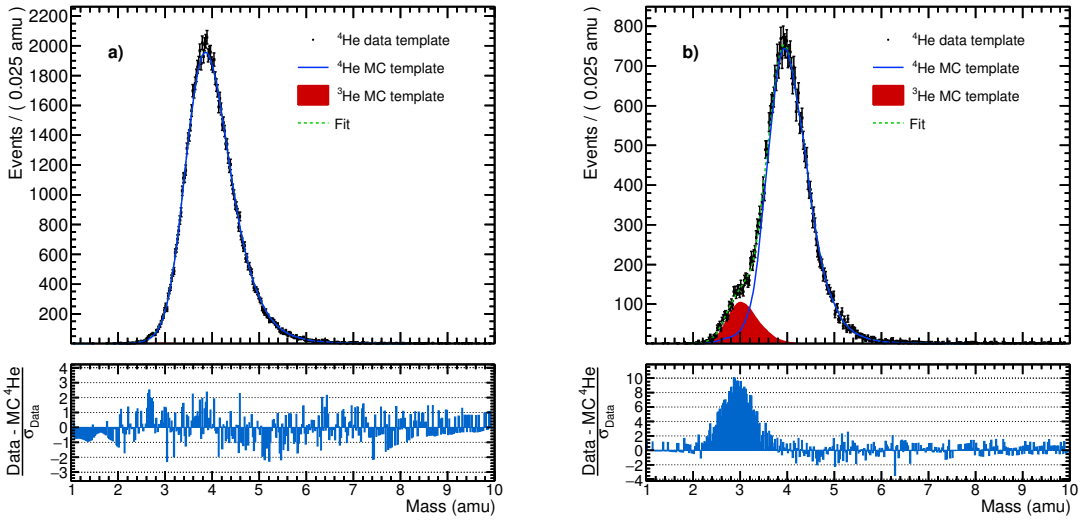

Figure 4-3: Comparisons of ^{4}He mass templates between data and simulation in the kinetic energy per nucleon interval of a) 7.66–8.13 GeV/n (aerogel radiator) and b) 0.97–1.05 GeV/n (NaF radiator). MC ^{4}He (blue solid curve) and ^{3}He (red shaded area) mass distributions were used to performed the template fit to the selected ^{4}He mass distribution (black solid circles) obtained directly from data (Earth's penumbral region). Each lower panel shows the significance per bin of the data with respect to the fit, in terms of the number of standard deviations, considering only the statistical fluctuations.

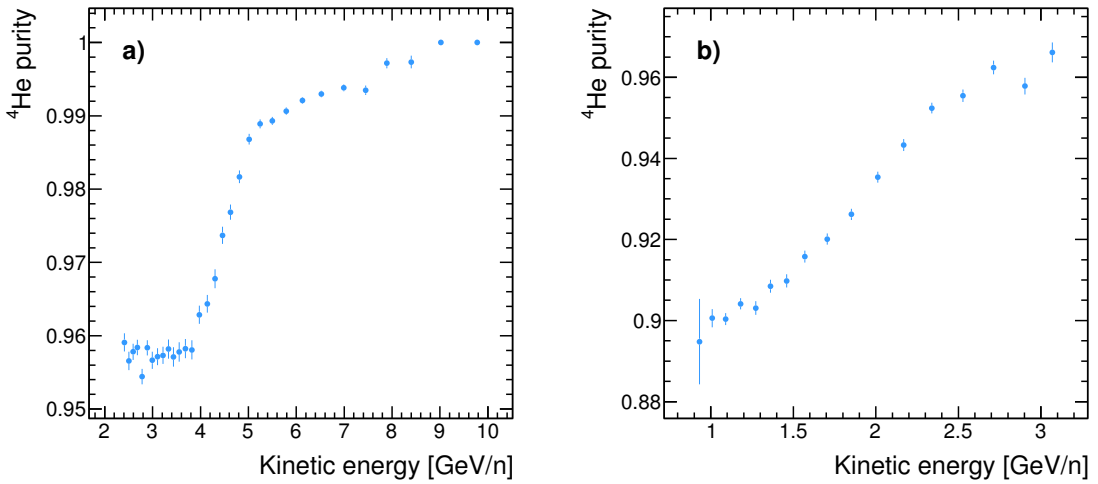

Figure 4-4: Purities of the ^{4}He data samples as functions of kinetic energy per nucleon for the a) aerogel and b) NaF radiator.

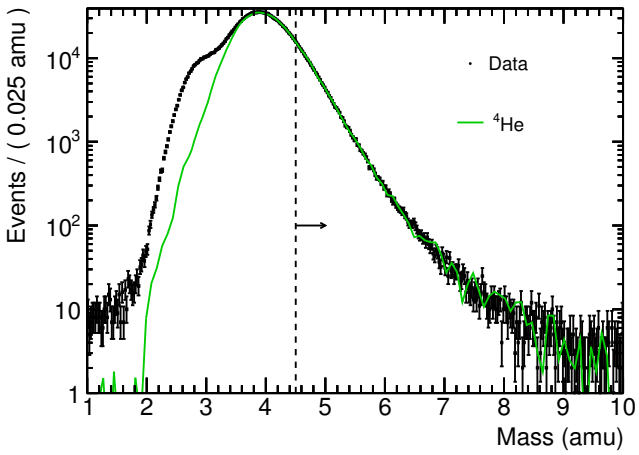

Figure 4-5: Example of using the ^{4}He mass template (green solid curve) obtained from data to extract the ^{3}He/^{4}He event counts ratio in the kinetic energy per nucleon interval from 6.3 GeV/n to 6.7 GeV/n. The vertical dash line represents the mass cut value of 4.5. The arrow indicates the right tail of the ^{4}He mass template is used to extract the fraction of ^{4}He above this cut.

Then, we used the ^{4}He mass templates obtained from data in the penumbral region to determine the ^{3}He/^{4}He event counts ratio. The cut and count method was employed because in the penumbra we can only obtain the template of the heavier isotope (i.e., ^{4}He). For an appropriate choice of the cut, $f^{>}_{^3\mathrm{He}} \approx 0$, so that the ^{3}He/^{4}He event counts ratio can be obtained from Eq. (4.5):

$$\frac{N_{^3\mathrm{He}}}{N_{^4\mathrm{He}}} \approx \frac{f^{>}_{^4\mathrm{He}}/\mathrm{purity} - f^{>}}{f^{>}}.$$

Mass cut values of 4, 4.2, and 4.5 were used. Figure 4-5 shows an example of the cut and count method to extract the ^{3}He/^{4}He event counts ratio using the ^{4}He mass template obtained from data (exploiting the ^{4}He-enriched region, i.e., the right tail of the mass template).

We varied the safety factors on geomagnetic rigidity cutoffs when calculating the upper and lower β thresholds for the penumbral region according to Eqs.(4.6) and (4.7): $\mathbb{SF}_{^4\mathrm{He}} = \{1.00, 1.05, 1.10, 1.12\}$ and $\mathbb{SF}_{^3\mathrm{He}} = \{1.00, 0.95, 0.90, 0.88\}$, which led to $4 \times 4 = 16$ combinations of the penumbral region thresholds.

The averages of the ^{3}He/^{4}He ratio obtained using different $SF_{^4\mathrm{He}}$, $SF_{^3\mathrm{He}}$, and

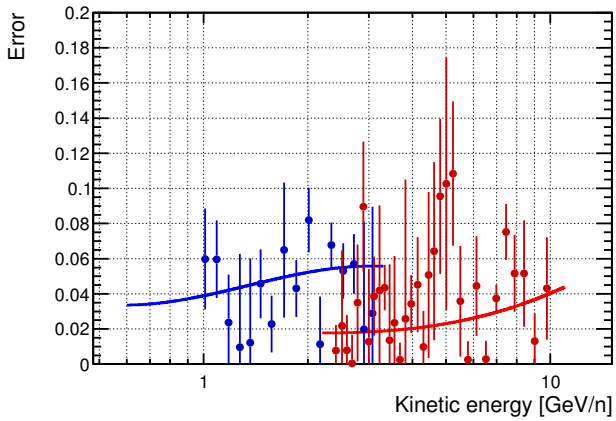

Figure 4-6: Systematic errors from the potential data-MC mismatches in the mass template for the aerogel (red) and NaF (blue) radiator. The curves show the spline fit to the relative errors.

A_{cut} values for each kinetic energy per nucleon bin were compared to the results of the template fit, to establish systematic uncertainties associated with the potential data-MC mismatches in the mass template, as shown in Figure 4-6.

4.2.5 MC Acceptance Ratio

The acceptance term $A^{^4\text{He}}_{i,\text{MC}}/A^{^3\text{He}}_{i,\text{MC}}$ in Eq. (4.1) was calculated from the ^{4}He/^{3}He folded acceptance ratio using MC simulations. To account for the bin-to-bin migration, the MC generated rigidity spectra of both ^{4}He and ^{3}He were reweighted to the AMS helium spectrum [116]. These reweighted MC samples were then used to calculate the folded acceptances of ^{4}He and ^{3}He. Figure 4-7 shows the ^{4}He/^{3}He acceptance ratio as a function of measured kinetic energy per nucleon.

4.3 Preliminary Result

Figure 4-8 shows the ^{3}He/^{4}He ratio as a function of kinetic energy per nucleon with the total errors, the sum in quadrature of statistical and current systematic errors. In this stage of the analysis, the contributions to the systematic uncertainties only come from 1) the template fitting procedure and 2) potent data-MC mismatches in the

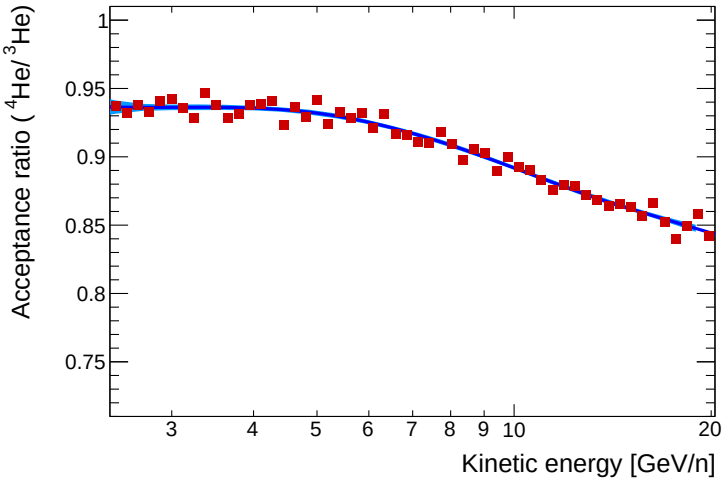

Figure 4-7: ^{4}He/^{3}He folded acceptance ratio as a function of kinetic energy per nucleon. The curve shows the spline fit to the acceptance ratio.

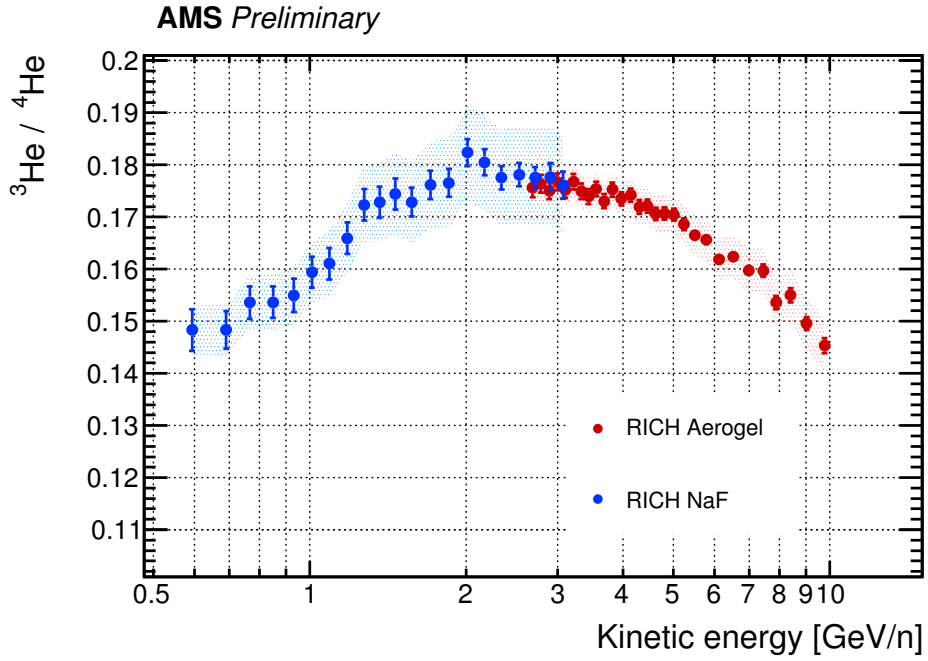

Figure 4-8: The ^{3}He to ^{4}He flux ratio as a function of kinetic energy per nucleon from 0.6 GeV/n to 10 GeV/n. The red (blue) solid circles with error bars indicate results of the RICH aerogel (NaF) radiator measurements with statistical uncertainties while shaded areas correspond to current systematic uncertainties.

template. They are added in quadrature to arrive at the total systematic uncertainty on the ^{3}He/^{4}He ratio.

Conclusions and Outlook

Because of the importance of the carbon and oxygen fluxes and their ratio to the understanding of the origin, acceleration, and subsequent propagation of cosmic rays, over the last 30 years there have been many measurements by balloon and satellite experiments [72, 73, 75, 76, 78–80, 82, 158–162]. Different variations of the carbon and oxygen fluxes with energy (or rigidity) have been reported by these previous measurements. Typically, these measurements have errors larger than 15% at 100 GV. In this thesis, we discuss a measurement of the carbon and oxygen fluxes from 2 GV to 2.6 TV based on high statistics (8.3 million carbon and 7.4 million oxygen events) with the AMS experiment. Very detailed studies of the systematic errors have been made. The AMS carbon flux as a function of rigidity multiplied by $\tilde{R}^{2.7}$ is presented in Figures 4-9 together with the earlier measurement by PAMELA [82] (the only available experimental data measured in rigidity before AMS). Figures 4-10, 4-11, and 4-12 show the AMS carbon flux, oxygen flux, and carbon to oxygen flux ratio, respectively, as functions of kinetic energy per nucleon $E_{\rm k}$ multiplied by $E_{\rm k}^{2.7}$ together with the results of previous experiments [72, 73, 75, 76, 78–80, 82] extracted using Ref. [163]. For the AMS measurement, $E_{\rm k} = \left(\sqrt{Z^2\tilde{R}^2 + M^2} - M\right)/A$, where Z, M, and A are the charge, mass, and atomic mass number, respectively, of ^{12}C or ^{16}O, as the AMS flux was treated as containing only ^{12}C or ^{16}O. The systematic error due to the conversion procedure is negligible over the entire energy range. As seen

1) in Figure 4-9, the AMS measurement of the carbon flux is different from the results of Ref. [82] which are 20%–25% lower above 20 GV;
2) in Figures 4-10 and 4-11, the AMS measurements of the carbon and oxygen fluxes at high energies are also very different from previous measurements, being

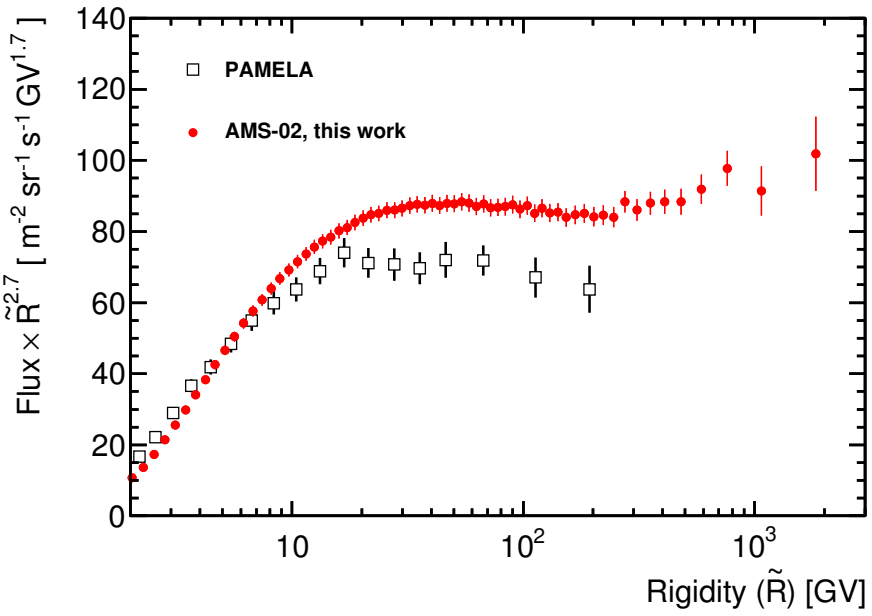

Figure 4-9: The AMS carbon flux with the total errors as a function of rigidity multiplied by $\tilde{R}^{2.7}$ compared with the earlier measurement by PAMELA [82].

about 20%–40% higher above 10 GeV/n;

3) in Figure 4-12, the C/O ratio measured by AMS is within 10% of unity.

The magnitude and rigidity dependence of the carbon and oxygen fluxes spectral indices are very similar. Their spectral indices are identical within the measurement errors above 60 GV. The fluxes deviate from a single power law and their spectral indices progressively harden at high rigidities (above $\sim$ 200 GV). The carbon to oxygen flux ratio above 60 GV has no rigidity dependence, well described by a constant value of 0.93 ± 0.02.

A preliminary analysis of the ^{3}He/^{4}He ratio as a function of kinetic energy per nucleon from 0.6 GeV/n to 10 GeV/n is described, with partial account of the systematic uncertainties. The dominant systematic errors, i.e., from the template fitting procedure and potential data-simulation mismatches in the template, have been studied. The evaluation of the remaining systematic errors arising from the other sources, e.g., the nuclear interaction cross-sections and RICH β scale, needs further study.

These results will feed into the numerical codes (e.g., GALPROP and DRAGON) describing the propagation process, modification of the spectra, and chemical com-

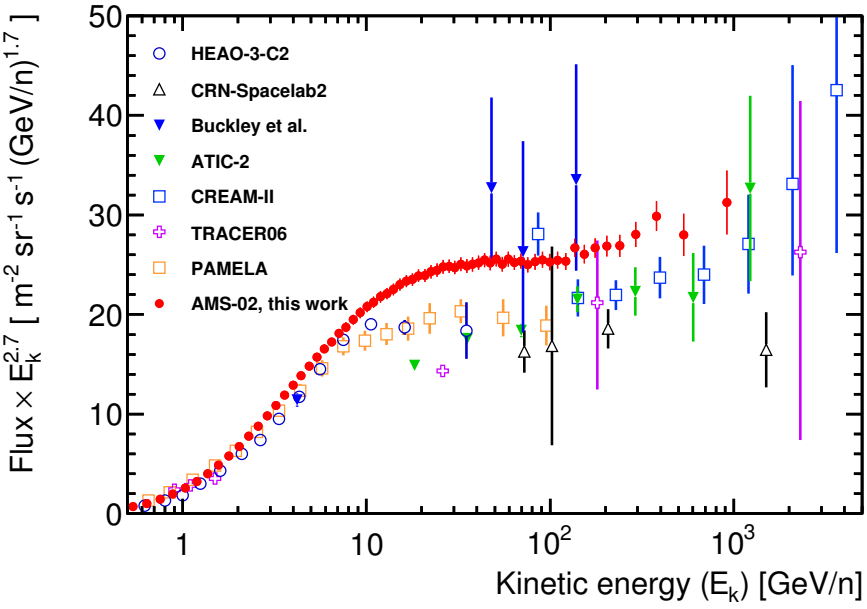

Figure 4-10: The AMS carbon flux with the total errors as a function of kinetic energy per nucleon E_{k} multiplied by $E_{\mathrm{k}}^{2.7}$ compared with previous measurements since the year 1980 [72, 73, 75, 76, 79, 80, 82].

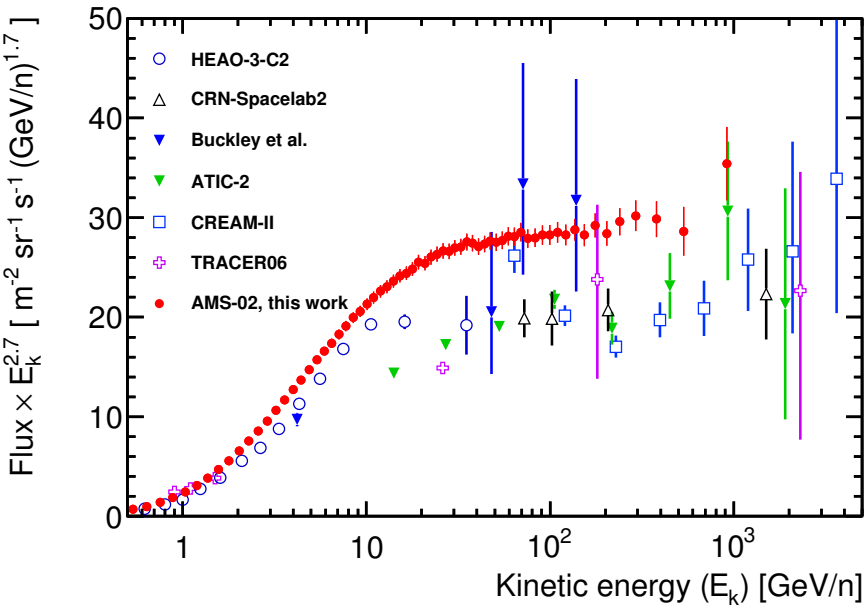

Figure 4-11: The AMS oxygen flux with the total errors as a function of kinetic energy per nucleon E_{k} multiplied by $E_{\mathrm{k}}^{2.7}$ compared with previous measurements since the year 1980 [72, 73, 75, 76, 79, 80].

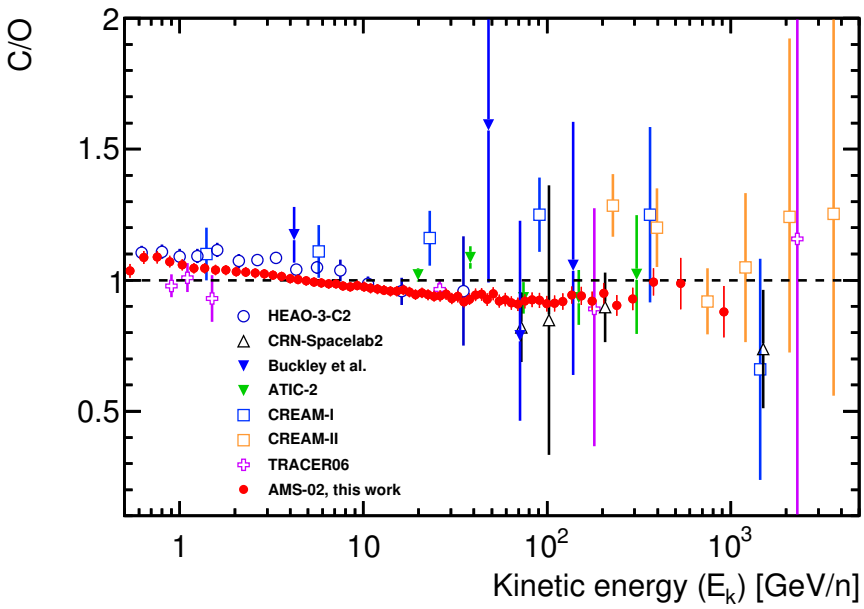

Figure 4-12: The AMS carbon to oxygen flux ratio with the total errors as a function of kinetic energy per nucleon E_{k} compared with previous measurements since the year 1980 [72, 73, 75, 76, 78–80]. As seen, the C/O ratio measured by AMS is within 10% of unity (dashed line).

position of galactic cosmic rays.

It is important to note that these are AMS preliminary results. Please refer to the AMS forthcoming publication in *Physical Review Letters*.

Appendix A

Flux Analysis

A.1 ECAL Energy Deposition Calibrated to Tracker Rigidity

In the determination of the rigidity dependence of the ITk tracking efficiency, the ECAL energy deposition E_{edep} was used as a cross-check of the other rigidity estimators (converted from TOF β and geomagnetic cutoff rigidity) and provided a potential indication of the behavior of the efficiency at higher energies (from few tens of GV to few hundreds of GV). E_{edep} was corrected using its observed correlation with the tracker rigidity R. In different E_{edep} intervals, we performed a gaussian fit to $\eta = E_{\text{edep}}/R$ to obtain the mean value $\hat{\eta}$ and then parameterized the E_{edep} dependence of $\hat{\eta}$ using a spline function, as shown in Figure A-1 for carbon events in data. This fitted function was used to calibrate E_{edep} to R. Analogously, this correction was done for the simulation.

A.2 Rigidity Binning

When we plot the flux result, the point for each bin is placed along the abscissa at $\tilde{R}$ calculated for a flux $\propto R^{-2.7}$ [135]; we have used Eq. (6) in Ref. [135] with $\tilde{R} \equiv x_{lw}$. The rigidity binning is tabulated in Table A.1.

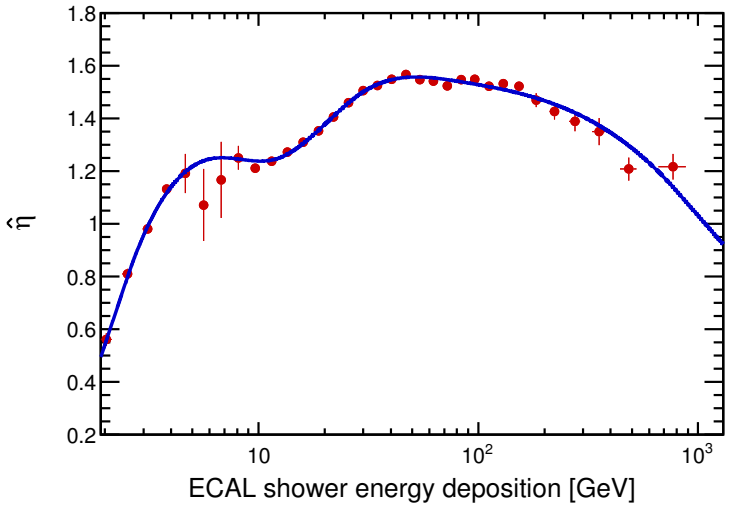

Figure A-1: Gaussian mean of the $\eta = E_{\mathrm{edep}}/R$ distribution as a function of ECAL energy deposition. The curve shows a spline fit to the mean values.

Table A.1: Rigidity bins of the carbon and oxygen fluxes measurement.

Bin ID	1	2	3	4	5	6
Rigidity (GV)	2.15 – 2.40	2.40 – 2.67	2.67 – 2.97	2.97 – 3.29	3.29 – 3.64	3.64 – 4.02
Bin ID	7	8	9	10	11	12
Rigidity (GV)	4.02 – 4.43	4.43 – 4.88	4.88 – 5.37	5.37 – 5.90	5.90 – 6.47	6.47 – 7.09
Bin ID	13	14	15	16	17	18
Rigidity (GV)	7.09 – 7.76	7.76 – 8.48	8.48 – 9.26	9.26 – 10.1	10.1 – 11.0	11.0 – 12.0
Bin ID	19	20	21	22	23	24
Rigidity (GV)	12.0 – 13.0	13.0 – 14.1	14.1 – 15.3	15.3 – 16.6	16.6 – 18.0	18.0 – 19.5
Bin ID	25	26	27	28	29	30
Rigidity (GV)	19.5 – 21.1	21.1 – 22.8	22.8 – 24.7	24.7 – 26.7	26.7 – 28.8	28.8 – 31.1
Bin ID	31	32	33	34	35	36
Rigidity (GV)	31.1 – 33.5	33.5 – 36.1	36.1 – 38.9	38.9 – 41.9	41.9 – 45.1	45.1 – 48.5
Bin ID	37	38	39	40	41	42
Rigidity (GV)	48.5 – 52.2	52.2 – 56.1	56.1 – 60.3	60.3 – 64.8	64.8 – 69.7	69.7 – 74.9
Bin ID	43	44	45	46	47	48
Rigidity (GV)	74.9 – 80.5	80.5 – 86.5	86.5 – 93.0	93.0 – 100	100 – 108	108 – 116
Bin ID	49	50	51	52	53	54
Rigidity (GV)	116 – 125	125 – 135	135 – 147	147 – 160	160 – 175	175 – 192
Bin ID	55	56	57	58	59	60
Rigidity (GV)	192 – 211	211 – 233	233 – 259	259 – 291	291 – 330	330 – 379
Bin ID	61	62	63	64	65	66
Rigidity (GV)	379 – 441	441 – 525	525 – 660	660 – 880	880 – 1300	1300 – 2600

Appendix B

Fragmentation Identification MVA

To select non-interacting samples on L1 for the L1 charge selection efficiency measurement, the rejection of fragmentations between L1 and L2 is important. Boosted Decision Trees (BDT), a multivariate analysis method provided by TMVA [150], are applied improve the fragmentation identification ability.

B.1 Training Samples

Training samples for signal and background are directly obtained from data. We select unfragmented (fragmented) events to be the signal (background) sample. They are tagged by the charge measurements with L1 and ITk as shown in Table B.1.

Table B.1: Training samples for signal and background.

	Signal	Background
Q_{ITk}	$Z - 0.45 < Q_{\mathrm{ITk}} < Z + 0.45$	$Z - 0.45 < Q_{\mathrm{ITk}} < Z + 0.45$
Q_{L1}	$Q_{\mathrm{L1}} < Z + 0.5$	$Q_{\mathrm{L1}} \geq Z + 2$

B.2 Input Variables

The input variables are listed as follows.

a) Number of reconstructed tracker tracks

b) Number of hits on the ITk

c) Number of clusters on the ACC

d) Number of hits on the TRD

e) Number of clusters on each of the 4 TOF layers

f) Sum of the charge measurements on each of the 4 TOF layers (in total 4 variables)

g) Maximum charge on each of the 4 TOF layers (in total 4 variables)

h) χ^2 of the 4 TOF layers coordinate measurements

i) χ^2 of the 4 TOF layers time (or velocity) measurements

j) Rigidity

The rigidity distribution of the signal is reweighted to match the one of the background, in order to make the BDT training as independent as possible from the carbon nuclei kinematics. For the rigidity, it is the correlations with other variables that are used in distinguishing signal from background, rather than the distribution itself.

B.3 BDT Output and Fragmentation Identification Performance

The output BDT variable for carbon data is shown in Figure B-1, where the signal events are in blue and the background events are in red. The training events are shown in solid circles and the testing events are in filled histograms. As seen, the distribution of testing events agrees well with that of the training events. The background rejection versus signal efficiency curve for the O $\rightarrow$ C (between L1 and L2) fragmentation ID MVA is shown in Figure B-2. In the MVA analysis, a cut at a selected working point ($BDT > 0.6$) is applied.

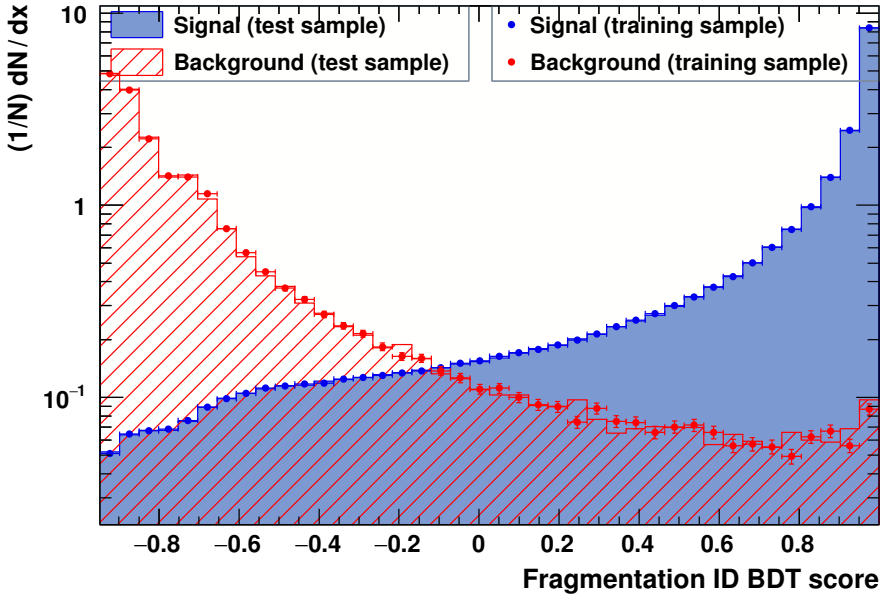

Figure B-1: Response of the BDT discriminant on the unfragmented (signal) and fragmented (background) events for the carbon samples.

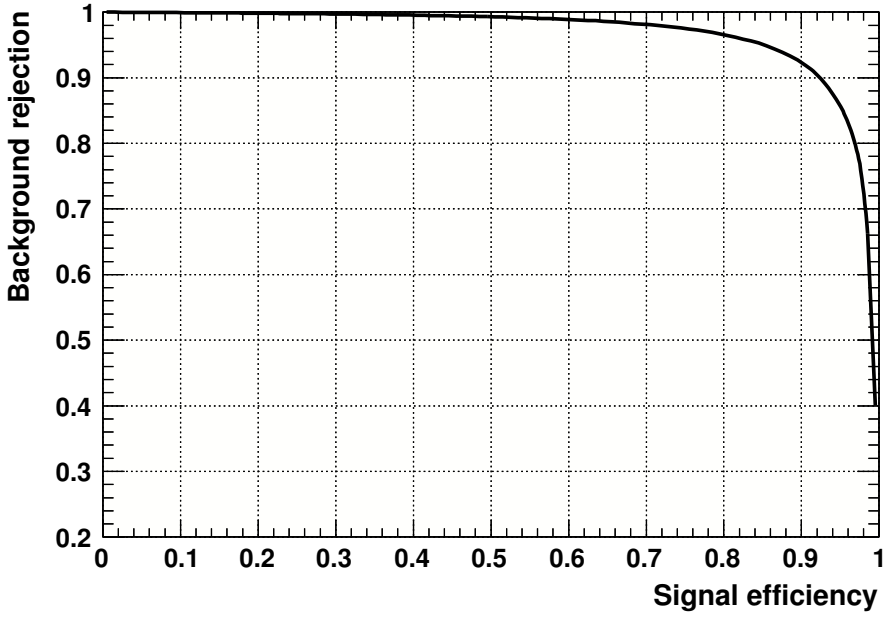

Figure B-2: Background rejection versus signal efficiency for carbon.

Appendix C

He Isotopes Mass Template Fit

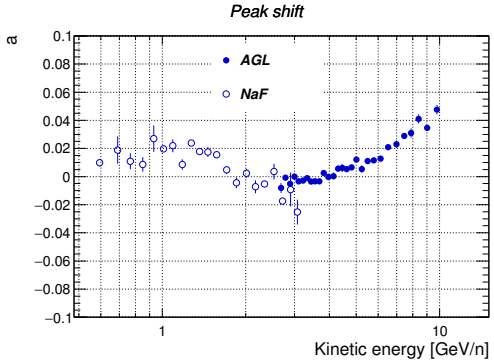

Figure C-1: Fitted values of the shift parameter for MC mass distributions measured with the aerogel (solid circles) and NaF (open circles) radiators.

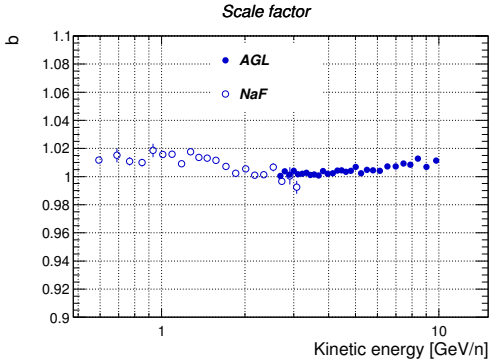

Figure C-2: Fitted values of the Rescaling parameter for MC mass distributions measured with the aerogel (solid circles) and NaF (open circles) radiators.

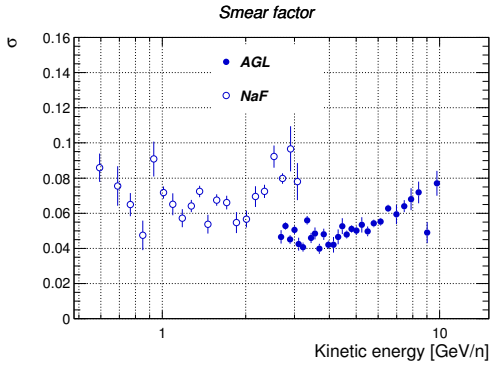

Figure C-3: Fitted values of the smearing parameter for MC mass distributions measured with the aerogel (solid circles) and NaF (open circles) radiators.

Bibliography

[1] Alessandro De Angelis and Mário Jo ao Martins Pimenta. *Introduction to Particle and Astroparticle Physics*. Springer-Verlag Mailand, 2015.

[2] G. A. Bazilevskaya. Solar cosmic rays in the near Earth space and the atmosphere. *Advances in Space Research*, 35(3):458–464, 2005.

[3] Victor Franz Hess. Über Beobachtungen der durchdringenden Strahlung bei sieben Freiballonfahrten. *Physikalische Zeitschrift*, 13:1084–1091, 1912.

[4] William Hanlon. `http://www.physics.utah.edu/~whanlon/spectrum.html`. Accessed: 2016-10-26.

[5] C. Patrignani. Review of Particle Physics. *Chin. Phys.*, C40(10):100001, 2016.

[6] G. V. Kulikov and G. B. Khristiansen. On the size spectrum of extensive air showers. *SOVIET PHYSICS JETP-USSR*, 8(3):441–444, 1959.

[7] Andreas Haungs, Heinigerd Rebel, and Markus Roth. Energy spectrum and mass composition of high-energy cosmic rays. *Reports on Progress in Physics*, 66(7):1145, 2003.

[8] R. U. Abbasi et al. (High Resolution Fly's Eye Collaboration). Observation of the ankle and evidence for a high-energy break in the cosmic ray spectrum. *Physics Letters B*, 619(3–4):271–280, 2005.

[9] R. U. Abbasi et al. (High Resolution Fly's Eye Collaboration). Measurement of the flux of ultra high energy cosmic rays by the stereo technique. *Astroparticle Physics*, 32(1):53–60, 2009.

[10] J. Abraham et al. (Pierre Auger Collaboration). Measurement of the energy spectrum of cosmic rays above 10^{18} eV using the Pierre Auger Observatory. *Physics Letters B*, 685(4–5):239–246, 2010.

[11] V. S. Berezinskii, S. V. Bulanov, V. A. Dogiel, and V. S. Ptuskin. *Astrophysics of cosmic rays*. 1990.

[12] A. W. Strong, I. V. Moskalenko, and V. S. Ptuskin. Cosmic-Ray Propagation and Interactions in the Galaxy. *Annual Review of Nuclear and Particle Science*, 57:285–327, Nov 2007.

[13] Kenneth Greisen. End to the Cosmic-Ray Spectrum? *Phys. Rev. Lett.*, 16:748–750, Apr 1966.

[14] G. T. Zatsepin and V. A. Kuz'min. Upper Limit of the Spectrum of Cosmic Rays. *Soviet Journal of Experimental and Theoretical Physics Letters*, 4:78, Aug 1966.

[15] Thomas K. Gaisser, Ralph Engel, and Elisa Resconi. *Cosmic Rays and Particle Physics*. Cambridge University Press, Cambridge, 2 edition, Jun 2016.

[16] Malcolm S. Longair. *High Energy Astrophysics*. Cambridge, 3 edition, Nov 2010.

[17] Peter L. Biermann et al. The Origin of Cosmic Rays: Explosions of Massive Stars with Magnetic Winds and Their Supernova Mechanism. *The Astrophysical Journal*, 725(1):184, 2010.

[18] Thomas K. Gaisser and Todor Stanev. High-energy cosmic rays. *Nuclear Physics A*, 777:98–110, 2006.

[19] K. Nagashima, K. Fujimoto, and R. M. Jacklyn. Galactic and heliotail-in anisotropies of cosmic rays as the origin of sidereal daily variation in the energy region $< 10^4$ GeV. *Journal of Geophysical Research: Space Physics*, 103(A8):17429–17440, 1998.

[20] D. L. Hall et al. Gaussian analysis of two hemisphere observations of galactic cosmic ray sidereal anisotropies. *Journal of Geophysical Research: Space Physics*, 104(A4):6737–6749, 1999.

[21] K. Munakata et al. Solar Cycle Dependence of the Diurnal Anisotropy of 0.6 TeV Cosmic-ray Intensity Observed with the Matsushiro Underground Muon Detector. *The Astrophysical Journal*, 712(2):1100, 2010.

[22] M. Amenomori et al. (Tibet ASgamma Collaboration). Large-Scale Sidereal Anisotropy of Galactic Cosmic-Ray Intensity Observed by the Tibet Air Shower Array. *The Astrophysical Journal Letters*, 626(1):L29, 2005.

[23] M. Amenomori et al. (Tibet ASgamma Collaboration). Anisotropy and Corotation of Galactic Cosmic Rays. *Science*, 314(5798):439–443, 2006.

[24] G. Guillian et al. (Super-Kamiokande Collaboration). Observation of the anisotropy of 10 TeV primary cosmic ray nuclei flux with the Super-Kamiokande-I detector. *Phys. Rev. D*, 75:062003, Mar 2007.

[25] A. A. Abdo et al. (Milagro Collaboration). Discovery of Localized Regions of Excess 10-TeV Cosmic Rays. *Phys. Rev. Lett.*, 101:221101, Nov 2008.

[26] A. A. Abdo et al. (Milagro Collaboration). The Large-Scale Cosmic-Ray Anisotropy as Observed with Milagro. *The Astrophysical Journal*, 698(2):2121, 2009.

[27] J. K. de Jong. Observations of Large Scale Sidereal Anisotropy in 1 and 11 TeV cosmic rays from the MINOS experiment. In *Proceedings, 32nd International Cosmic Ray Conference (ICRC 2011): Beijing, China, August 11–18, 2011*, volume 4, page 46, 2012.

[28] G. Di Sciascio (on behalf of the ARGO-YBJ Collaboration). Measurement of Cosmic Ray Spectrum and Anisotropy with ARGO-YBJ. *EPJ Web of Conferences*, 52:04004, 2013.

[29] B. Bartoli et al. (ARGO-YBJ Collaboration). Medium scale anisotropy in the TeV cosmic ray flux observed by ARGO-YBJ. *Phys. Rev. D*, 88:082001, Oct 2013.

[30] A. U. Abeysekara et al. (HAWC Collaboration). Observation of Small-scale Anisotropy in the Arrival Direction Distribution of TeV Cosmic Rays with HAWC. *The Astrophysical Journal*, 796(2):108, 2014.

[31] M. Aglietta et al. (EAS-TOP Collaboration). Evolution of the Cosmic-Ray Anisotropy Above 10^{14} eV. *The Astrophysical Journal Letters*, 692(2):L130, 2009.

[32] R. Abbasi et al. (IceCube Collaboration). Measurement of the Anisotropy of Cosmic-ray Arrival Directions with IceCube. *The Astrophysical Journal Letters*, 718(2):L194, 2010.

[33] R. Abbasi et al. (IceCube Collaboration). Observation of Anisotropy in the Arrival Directions of Galactic Cosmic Rays at Multiple Angular Scales with IceCube. *The Astrophysical Journal*, 740(1):16, 2011.

[34] R. Abbasi et al. (IceCube Collaboration). Observation of Anisotropy in the Galactic Cosmic-Ray Arrival Directions at 400 TeV with IceCube. *The Astrophysical Journal*, 746(1):33, 2012.

[35] M. G. Aartsen et al. (IceCube Collaboration). Anisotropy in Cosmic-Ray Arrival Directions in the Southern Hemisphere Based on Six Years of Data from the IceCube Detector. *The Astrophysical Journal*, 826(2):220, 2016.

[36] M. G. Aartsen et al. (IceCube Collaboration). Observation of Cosmic-Ray Anisotropy with the IceTop Air Shower Array. *The Astrophysical Journal*, 765(1):55, 2013.

[37] V. S. Ptuskin and J. F. Ormes. Expected Anisotropy of Very High Energy Electrons. In N. Iucci and E. Lamanna, editors, *Proceedings of the 24th International Cosmic Ray Conference*, volume 3, page 56, Rome, 1995.

[38] A. D. Erlykin and A. W. Wolfendale. The anisotropy of galactic cosmic rays as a product of stochastic supernova explosions. *Astroparticle Physics*, 25(3):183–194, 2006.

[39] I. Büsching, O. C. de Jager, M. S. Potgieter, and C. Venter. A Cosmic-Ray Positron Anisotropy due to Two Middle-Aged, Nearby Pulsars? *The Astrophysical Journal Letters*, 678(1):L39, 2008.

[40] Pasquale Blasi and Elena Amato. Diffusive propagation of cosmic rays from supernova remnants in the Galaxy. II: anisotropy. *Journal of Cosmology and Astroparticle Physics*, 2012(01):011, 2012.

[41] Martin Pohl and David Eichler. Understanding TeV-band Cosmic-Ray Anisotropy. *The Astrophysical Journal*, 766(1):4, 2013.

[42] L. G. Sveshnikova, O. N. Strelnikova, and V. S. Ptuskin. Spectrum and anisotropy of cosmic rays at TeV–PeV-energies and contribution of nearby sources. *Astroparticle Physics*, 50–52:33–46, 2013.

[43] Markus Ahlers. Deciphering the Dipole Anisotropy of Galactic Cosmic Rays. *Phys. Rev. Lett.*, 117:151103, Oct 2016.

[44] Arthur H. Compton and Ivan A. Getting. An Apparent Effect of Galactic Rotation on the Intensity of Cosmic Rays. *Phys. Rev.*, 47:817–821, Jun 1935.

[45] L. J. Gleeson and W. I. Axford. The compton-getting effect. *Astrophysics and Space Science*, 2(4):431–437, 1968.

[46] Gwenael Giacinti and Günter Sigl. Local Magnetic Turbulence and TeV–PeV Cosmic Ray Anisotropies. *Phys. Rev. Lett.*, 109:071101, Aug 2012.

[47] Markus Ahlers. Anomalous Anisotropies of Cosmic Rays from Turbulent Magnetic Fields. *Phys. Rev. Lett.*, 112:021101, Jan 2014.

[48] V. López-Barquero et al. Cosmic-Ray Small-scale Anisotropies and Local Turbulent Magnetic Fields. *The Astrophysical Journal*, 830(1):19, 2016.

[49] P. Desiati and A. Lazarian. Anisotropy of TeV Cosmic Rays and Outer Heliospheric Boundaries. *The Astrophysical Journal*, 762(1):44, 2013.

[50] Ming Zhang, Pingbing Zuo, and Nikolai Pogorelov. Heliospheric Influence on the Anisotropy of TeV Cosmic Rays. *The Astrophysical Journal*, 790(1):5, 2014.

[51] W. Baade and F. Zwicky. Cosmic Rays from Super-Novae. *Proceedings of the National Academy of Sciences*, 20(5):259–263, 1934.

[52] W. Baade and F. Zwicky. Remarks on Super-Novae and Cosmic Rays. *Phys. Rev.*, 46:76–77, Jul 1934.

[53] V. L. Ginzburg and S. I. Syrovatsky. Origin of Cosmic Rays. *Progress of Theoretical Physics Supplement*, 20:1–83, 1961.

[54] G. F. Krymskii. A regular mechanism for the acceleration of charged particles on the front of a shock wave. *Akademiia Nauk SSSR Doklady*, 234:1306–1308, Jun 1977.

[55] R. D. Blandford and J. P. Ostriker. Particle acceleration by astrophysical shocks. *The Astrophysical Journal Letters*, 221:L29–L32, Apr 1978.

[56] W. I. Axford, E. Leer, and G. Skadron. The acceleration of cosmic rays by shock waves. *International Cosmic Ray Conference*, 11:132–137, 1977.

[57] A. R. Bell. The acceleration of cosmic rays in shock fronts – I. *Monthly Notices of the Royal Astronomical Society*, 182(2):147–156, 1978.

[58] A. R. Bell. The acceleration of cosmic rays in shock fronts – II. *Monthly Notices of the Royal Astronomical Society*, 182(3):443–455, 1978.

[59] Pasquale Blasi. The origin of galactic cosmic rays. *The Astronomy and Astrophysics Review*, 21(1):70, 2013.

[60] L. O'C. Drury et al. Test of galactic cosmic-ray source models – Working Group Report. *Space Science Reviews*, 99(1):329–352, 2001.

[61] E. Fermi. On the Origin of the Cosmic Radiation. *Phys. Rev.*, 75:1169–1174, Apr 1949.

[62] Malcolm S. Longair. The acceleration of high energy particles. In *High Energy Astrophysics*, pages 561–582. Cambridge University Press, Cambridge, Nov 2010.

[63] E. Fermi. Galactic Magnetic Fields and the Origin of Cosmic Radiation. *The Astrophysical Journal*, 119:1, Jan 1954.

[64] Eric Herbst. Chemistry in the Interstellar Medium. *Annual Review of Physical Chemistry*, 46(1):27–54, 1995.

[65] V. L. Ginzburg and V. S. Ptuskin. On the origin of cosmic rays: Some problems in high-energy astrophysics. *Rev. Mod. Phys.*, 48:161–189, Apr 1976.

[66] Andrew W. Strong and Igor V. Moskalenko. Propagation of Cosmic-Ray Nucleons in the Galaxy. *The Astrophysical Journal*, 509(1):212, 1998.

[67] Carmelo Evoli et al. Cosmic-ray propagation with DRAGON2: I. numerical solver and astrophysical ingredients. 2016.

[68] R. Cowsik, Yash Pal, S. N. Tandon, and R. P. Verma. Steady State of Cosmic-Ray Nuclei—Their Spectral Shape and Path Length at Low Energies. *Phys. Rev.*, 158:1238–1242, Jun 1967.

[69] A. N. Kolmogorov. The local structure of turbulence in incompressible viscous fluid for very large Reynolds numbers. In *Dokl. Akad. Nauk SSSR*, volume 30, pages 301–305, 1941.

[70] A. N. Kolmogorov. The Local Structure of Turbulence in Incompressible Viscous Fluid for Very Large Reynolds Numbers. *Proceedings of the Royal Society of London A: Mathematical, Physical and Engineering Sciences*, 434(1890):9–13, 1991.

[71] Robert H. Kraichnan. Inertial-Range Spectrum of Hydromagnetic Turbulence. *Physics of Fluids*, 8(7):1385–1387, 1965.

[72] J. J. Engelmann et al. Charge composition and energy spectra of cosmic-ray nuclei for elements from Be to NI. Results from HEAO-3-C2. *Astronomy and Astrophysics*, 233:96–111, 1990.

[73] Dietrich Müeller et al. Energy spectra and composition of primary cosmic rays. *The Astrophysical Journal*, 374:356–365, 1991.

[74] S. P. Swordy et al. Relative abundances of secondary and primary cosmic rays at high energies. *The Astrophysical Journal*, 349:625–633, Feb 1990.

[75] J. Buckley et al. A new measurement of the flux of the light cosmic-ray nuclei at high energies. *The Astrophysical Journal*, 429:736–747, 1994.

[76] A. D. Panov et al. Energy spectra of abundant nuclei of primary cosmic rays from the data of ATIC-2 experiment: Final results. *Bulletin of the Russian Academy of Sciences: Physics*, 73(5):564–567, 2009.

[77] A. D. Panov et al. Relative abundances of cosmic ray nuclei B-C-N-O in the energy region from 10 GeV/n to 300 GeV/n. Results from ATIC-2 (the science flight of ATIC). *International Cosmic Ray Conference*, 2:3–6, 2008.

[78] H. S. Ahn et al. Measurements of cosmic-ray secondary nuclei at high energies with the first flight of the CREAM balloon-borne experiment. *Astroparticle Physics*, 30(3):133–141, 2008.

[79] H. S. Ahn et al. Energy Spectra of Cosmic-ray Nuclei at High Energies. *The Astrophysical Journal*, 707(1):593, 2009.

[80] A. Obermeier et al. Energy Spectra of Primary and Secondary Cosmic-Ray Nuclei Measured with TRACER. *The Astrophysical Journal*, 742(1):14, 2011.

[81] A. Obermeier, P. Boyle, J. Hörandel, and D. Müller. The Boron-to-carbon Abundance Ratio and Galactic Propagation of Cosmic Radiation. *The Astrophysical Journal*, 752(1):69, 2012.

[82] O. Adriani et al. Measurement of Boron and Carbon Fluxes in Cosmic Rays with the PAMELA Experiment. *The Astrophysical Journal*, 791(2):93, 2014.

[83] M. Aguilar et al. (AMS Collaboration). Precision Measurement of the Boron to Carbon Flux Ratio in Cosmic Rays from 1.9 GV to 2.6 TV with the Alpha Magnetic Spectrometer on the International Space Station. *Phys. Rev. Lett.*, 117:231102, Nov 2016.

[84] Maurizio Spurio. *Particles and Astrophysics*. Springer International Publishing, 1 edition, 2015.

[85] N. E. Yanasak et al. Measurement of the Secondary Radionuclides ^{10}Be, ^{26}Al, ^{36}Cl, ^{54}Mn, and ^{14}C and Implications for the Galactic Cosmic-Ray Age. *The Astrophysical Journal*, 563(2):768, 2001.

[86] A. Kounine, Int. J. Mod. Phys. E **21** 1230005 (2012); S. Rosier-Lees, in *Proceedings of Astroparticle Physics TEVPA/IDM*, Amsterdam, 2014 (to be published); S. Ting, Nucl. Phys. B, Proc. Suppl. **243-244**, 12 (2013); S.-C. Lee, in Proceedings of the 20th International Conference on Supersymmetry and Unification of Fundamental Interactions (SUSY 2012), Beijing, 2012 (unpublished); M. Aguilar, in Proceedings of the XL International Meeting on Fundamental Physics, Centro de Ciencias de Benasque Pedro Pascual, 2012 (unpublished); S. Schael, in Proceedings of the 10th Symposium on Sources and Detection of Dark Matter and Dark Energy in the Universe, Los Angeles, 2012 (unpublished); B. Bertucci, *Proc. Sci.*, EPS-HEP, (2011) 67; M. Incagli, AIP Conf. Proc. **1223**, 43 (2010); R. Battiston, Nucl. Instrum. Methods Phys. Res., Sect. A **588**, 227 (2008).

[87] B. Alpat et al. The internal alignment and position resolution of the AMS-02 silicon tracker determined with cosmic-ray muons. *Nuclear Instruments and Methods in Physics Research Section A: Accelerators, Spectrometers, Detectors and Associated Equipment*, 613(2):207–217, 2010.

[88] Thomas Kirn. The AMS-02 TRD on the international space station. *Nuclear Instruments and Methods in Physics Research Section A: Accelerators, Spectrometers, Detectors and Associated Equipment*, 706:43–47, 2013.

[89] Ph.v. Doetinchem et al. Performance of the AMS-02 transition radiation detector. *Nuclear Instruments and Methods in Physics Research Section A: Accelerators, Spectrometers, Detectors and Associated Equipment*, 558(2):526–535, 2006.

[90] F. Hauler et al. The AMS-02 TRD for the international space station. *IEEE Transactions on Nuclear Science*, 51(4):1365–1372, Aug 2004.

[91] V. Bindi et al. Calibration and performance of the AMS-02 time of flight detector in space. *Nuclear Instruments and Methods in Physics Research Section A: Accelerators, Spectrometers, Detectors and Associated Equipment*, 743:22–29, 2014.

[92] K. Lübelsmeyer et al. Upgrade of the Alpha Magnetic Spectrometer (AMS-02) for long term operation on the International Space Station (ISS). *Nuclear Instruments and Methods in Physics Research Section A: Accelerators, Spectrometers, Detectors and Associated Equipment*, 654(1):639–648, 2011.

[93] M. Aguilar et al. The Alpha Magnetic Spectrometer (AMS) on the International Space Station: Part I âĂŞ results from the test flight on the space shuttle. *Physics Reports*, 366(6):331–405, 2002.

[94] Ph. von Doetinchem et al. The AMS-02 Anticoincidence Counter. *Nuclear Physics B - Proceedings Supplements*, 197(1):15–18, 2009.

[95] F. Giovacchini. Performance in space of the AMS-02 RICH detector. *Nuclear Instruments and Methods in Physics Research Section A: Accelerators, Spectrometers, Detectors and Associated Equipment*, 766:57–60, 2014.

[96] M. Aguilar-Benitez et al. In-beam aerogel light yield characterization for the AMS RICH detector. *Nuclear Instruments and Methods in Physics Research Section A: Accelerators, Spectrometers, Detectors and Associated Equipment*, 614(2):237–249, 2010.

[97] P. Aguayo et al. Prototype study of the Cherenkov imager of the AMS experiment. *Nuclear Instruments and Methods in Physics Research Section A: Accelerators, Spectrometers, Detectors and Associated Equipment*, 560(2):291–302, 2006.

[98] B. Baret et al. In-beam tests of the AMS RICH prototype with 20 A GeV/c secondary ions. *Nuclear Instruments and Methods in Physics Research Section A: Accelerators, Spectrometers, Detectors and Associated Equipment*, 525(1âĂŞ2):126–131, 2004.

[99] J. Casaus. The AMS RICH detector. *Nuclear Physics B - Proceedings Supplements*, 113(1):147–153, 2002.

[100] C. Adloff et al. The AMS-02 lead-scintillating fibres Electromagnetic Calorimeter. *Nuclear Instruments and Methods in Physics Research Section A: Accelerators, Spectrometers, Detectors and Associated Equipment*, 714:147–154, 2013.

[101] Sylvie Rosier-Lees (on behalf of the AMS Collaboration). Performance of the AMS02 Electromagnetic Calorimeter in space. *Journal of Physics: Conference Series*, 404(1):012034, 2012.

[102] F. Cadoux et al. The AMS-02 electromagnetic calorimeter. *Nuclear Physics B - Proceedings Supplements*, 113(1âĂŞ3):159–165, 2002.

[103] L. Accardo et al. (AMS Collaboration). High Statistics Measurement of the Positron Fraction in Primary Cosmic Rays of 0.5–500 GeV with the Alpha Magnetic Spectrometer on the International Space Station. *Phys. Rev. Lett.*, 113:121101, Sep 2014.

[104] Hai Chen. *Precision Measurement of electron and positron flux in cosmic rays with the AMS-02 Detector*. PhD thesis, Massachusetts Institute of Technology, 2016.

[105] Philipp Azzarello. *Tests and production of the AMS-02 silicon tracker detectors*. PhD thesis, Université de Genève, 2004.

[106] Pierre Saouter. *Nuclei identification with the AMS-02 silicon tracker and measurement of cosmic ray nuclei fluxes*. PhD thesis, Université de Genève, 2014.

[107] G. Ambrosi et al. Alignment of the AMS-02 silicon Tracker. In *Proceedings, 33rd International Cosmic Ray Conference (ICRC2013): Rio de Janeiro, Brazil, July 2–9, 2013*, page 1260, 2013.

[108] G. Ambrosi et al. The spatial resolution of the silicon tracker of the Alpha Magnetic Spectrometer. *Nuclear Instruments and Methods in Physics Research Section A: Accelerators, Spectrometers, Detectors and Associated Equipment*, 869:29–37, 2017.

[109] V. Bindi et al. Calibration and performance of the AMS-02 time of flight detector in space. *Nuclear Instruments and Methods in Physics Research Section A: Accelerators, Spectrometers, Detectors and Associated Equipment*, 743:22–29, 2014.

[110] Matthew Scott Krafczyk. *A precision measurement of the cosmic ray positron fraction on the international space station*. PhD thesis, Massachusetts Institute of Technology, 2016.

[111] M. Aguilar et al. (AMS Collaboration). First Result from the Alpha Magnetic Spectrometer on the International Space Station: Precision Measurement of the Positron Fraction in Primary Cosmic Rays of 0.5–350 GeV. *Phys. Rev. Lett.*, 110:141102, Apr 2013.

[112] Hu Liu et al. The RICH detector of AMS-02: 5 years of operation in space. *Nuclear Instruments and Methods in Physics Research Section A: Accelerators, Spectrometers, Detectors and Associated Equipment*, pages –, 2016.

[113] L. Breiman, J. H. Friedman, C. J. Stone, and R. A. Olshen. *Classification and regression trees*. CRC press, 1984.

[114] Yoav Freund and Robert E Schapire. A Decision-Theoretic Generalization of On-Line Learning and an Application to Boosting. *Journal of Computer and System Sciences*, 55(1):119–139, 1997.

[115] Byron P. Roe et al. Boosted decision trees as an alternative to artificial neural networks for particle identification. *Nuclear Instruments and Methods in Physics Research Section A: Accelerators, Spectrometers, Detectors and Associated Equipment*, 543(2–3):577–584, 2005.

[116] M. Aguilar et al. (AMS Collaboration). Precision Measurement of the Helium Flux in Primary Cosmic Rays of Rigidities 1.9 GV to 3 TV with the Alpha Magnetic Spectrometer on the International Space Station. *Phys. Rev. Lett.*, 115:211101, Nov 2015.

[117] Stefan Schael. Precision measurements of the electron spectrum and the positron spectrum with AMS. In *Proceedings, 33rd International Cosmic Ray Conference (ICRC2013): Rio de Janeiro, Brazil, July 2–9, 2013*, page 1257, 2013.

[118] M. A. Abdu, I. S. Batista, A. J. Carrasco, and C. G. M. Brum. South Atlantic magnetic anomaly ionization: A review and a new focus on electrodynamic effects in the equatorial ionosphere. *Journal of Atmospheric and Solar-Terrestrial Physics*, 67(17–18):1643–1657, 2005.

[119] D. M. Sawyer and J. I. Vette. AP-8 trapped proton environment for solar maximum and solar minimum. Technical report, NASA Goddard Space Flight Center, Greenbelt, MD, United States, 1976.

[120] The US/UK World Magnetic Model for 2015-2020 (NOAA National Geophysical Data Center (NGDC) and Cooperative Institute for Research in Environmental Sciences (CIRES)). `https://www.ngdc.noaa.gov/geomag/WMM/`. Accessed: 2017-01-11.

[121] J. Allison et al. Geant4 developments and applications. *IEEE Transactions on Nuclear Science*, 53(1):270–278, Feb 2006.

[122] S. Agostinelli et al. GEANT4—a simulation toolkit. *Nuclear Instruments and Methods in Physics Research Section A: Accelerators, Spectrometers, Detectors and Associated Equipment*, 506(3):250–303, 2003.

[123] A. Boudard et al. New potentialities of the Liège intranuclear cascade model for reactions induced by nucleons and light charged particles. *Phys. Rev. C*, 87:014606, Jan 2013.

[124] S. Leray et al. Extension of the Liège Intra Nuclear Cascade model to light ion-induced collisions for medical and space applications. *Journal of Physics: Conference Series*, 420(1):012065, 2013.

[125] J. Ranft. Dual parton model at cosmic ray energies. *Phys. Rev. D*, 51:64–84, Jan 1995.

[126] V. G. Ableev et al. *Acta Phys. Pol. B*, 16:913, 1985.

[127] Isabelle A. Grenier, John H. Black, and Andrew W. Strong. The Nine Lives of Cosmic Rays in Galaxies. *Annual Review of Astronomy and Astrophysics*, 53(1):199–246, 2015.

[128] Antonella Castellina and Fiorenza Donato. Diffusion coefficient and acceleration spectrum from direct measurements of charged cosmic ray nuclei. *Astroparticle Physics*, 24(1–2):146–159, 2005.

[129] M. Aguilar et al. (AMS Collaboration). Precision Measurement of the Proton Flux in Primary Cosmic Rays from Rigidity 1 GV to 1.8 TV with the Alpha Magnetic Spectrometer on the International Space Station. *Phys. Rev. Lett.*, 114:171103, Apr 2015.

[130] J. Alcaraz et al. (AMS Collaboration). Leptons in near earth orbit. *Physics Letters B*, 484(1–2):10–22, 2000.

[131] C. C. Finlay et al. International Geomagnetic Reference Field: the eleventh generation. *Geophysical Journal International*, 183(3):1216–1230, 2010.

[132] Erwan Thébault et al. International Geomagnetic Reference Field: the 12th generation. *Earth, Planets and Space*, 67(1):79, 2015.

[133] D. F. Smart and M. A. Shea. A review of geomagnetic cutoff rigidities for earth-orbiting spacecraft. *Advances in Space Research*, 36(10):2012–2020, 2005.

[134] J. D. Sullivan. Geometric factor and directional response of single and multi-element particle telescopes. *Nuclear Instruments and Methods*, 95(1):5–11, 1971.

[135] G. D. Lafferty and T. R. Wyatt. Where to stick your data points: The treatment of measurements within wide bins. *Nuclear Instruments and Methods in Physics Research Section A: Accelerators, Spectrometers, Detectors and Associated Equipment*, 355(2):541–547, 1995.

[136] Laurent Basara, Vitaly Choutko, and Qiang Li. Light nuclear charge measurement with Alpha Magnetic Spectrometer Electromagnetic Calorimeter. *Nuclear Instruments and Methods in Physics Research Section A: Accelerators, Spectrometers, Detectors and Associated Equipment*, 821:23–27, 2016.

[137] J. Jaros et al. Nucleus-nucleus total cross sections for light nuclei at 1.55 and 2.89 GeV/c per nucleon. *Phys. Rev. C*, 18:2273–2292, Nov 1978.

[138] V. D. Aksinenko et al. Streamer chamber study of the cross sections and multiplicities in nucleus-nucleus interactions at the incident momentum of 4.5 GeV/c per nucleon. *Nuclear Physics A*, 348(4):518–534, 1980.

[139] S. Kox et al. Direct measurements of heavy-ion total reaction cross sections at 30 and 83 MeV/nucleon. *Nuclear Physics A*, 420(1):162–172, 1984.

[140] S. Kox et al. Trends of total reaction cross sections for heavy ion collisions in the intermediate energy range. *Phys. Rev. C*, 35:1678–1691, May 1987.

[141] D. Q. Fang et al. Measurements of total reaction cross sections for some light nuclei at intermediate energies. *Phys. Rev. C*, 61:064311, May 2000.

[142] A. Ozawa et al. Measurements of interaction cross sections for light neutron-rich nuclei at relativistic energies and determination of effective matter radii. *Nuclear Physics A*, 691(3):599–617, 2001.

[143] H. Y. Zhang et al. Measurement of reaction cross section for proton-rich nuclei (A<30) at intermediate energies. *Nuclear Physics A*, 707(3):303–324, 2002.

[144] T. Zheng et al. Study of halo structure of 16C from reaction cross section measurement. *Nuclear Physics A*, 709(1):103–118, 2002.

[145] M. Takechi et al. Reaction cross sections at intermediate energies and Fermi-motion effect. *Phys. Rev. C*, 79:061601, Jun 2009.

[146] G. D'Agostini. A multidimensional unfolding method based on Bayes' theorem. *Nuclear Instruments and Methods in Physics Research Section A: Accelerators, Spectrometers, Detectors and Associated Equipment*, 362(2):487–498, 1995.

[147] Volker Blobel. Unfolding methods in high-energy physics experiments. (DESY-84-118):40, Dec 1984.

[148] A. Kondor. Method of convergent weights—An iterative procedure for solving Fredholm's integral equations of the first kind. *Nuclear Instruments and Methods in Physics Research*, 216(1):177–181, 1983.

[149] J. Albert et al. Unfolding of differential energy spectra in the MAGIC experiment. *Nuclear Instruments and Methods in Physics Research Section A: Accelerators, Spectrometers, Detectors and Associated Equipment*, 583(2–3):494–506, 2007.

[150] P. Speckmayer, A. Höcker, J. Stelzer, and H. Voss. The toolkit for multivariate data analysis, TMVA 4. *Journal of Physics: Conference Series*, 219(3):032057, 2010.

[151] M. Aguilar et al. (AMS Collaboration). Antiproton Flux, Antiproton-to-Proton Flux Ratio, and Properties of Elementary Particle Fluxes in Primary Cosmic Rays Measured with the Alpha Magnetic Spectrometer on the International Space Station. *Phys. Rev. Lett.*, 117:091103, Aug 2016.

[152] J. Berdugo, V. Choutko, C. Delgado, and Q. Yan. Determination of the rigidity scale of the Alpha Magnetic Spectrometer. *Nuclear Instruments and Methods in Physics Research Section A: Accelerators, Spectrometers, Detectors and Associated Equipment*, 869:10–14, 2017.

[153] B. Coste, L. Derome, D. Maurin, and A. Putze. Constraining Galactic cosmic-ray parameters with $Z \leq 2$ nuclei. *Astronomy and Astrophysics*, 539:A88, 2012.

[154] Measurement of the centrality dependence of open heavy flavour production in lead-lead collisions at $\sqrt{s} = 2.76$ TeV with the ATLAS detector. Technical Report ATLAS-CONF-2012-050, CERN, Geneva, May 2012.

[155] F. James and M. Roos. Minuit - a system for function minimization and analysis of the parameter errors and correlations. *Computer Physics Communications*, 10(6):343–367, 1975.

[156] Wouter Verkerke and David P. Kirkby. The RooFit toolkit for data modeling. *eConf*, C0303241:MOLT007, 2003. [arXiv:0306116].

[157] W. Gillard, F. Barao, and L. Derome. Isotopic Identification with the Geomagnetic Field for Space Experiments. In *Proceedings, 32nd International Cosmic Ray Conference (ICRC 2011): Beijing, China, August 11–18, 2011*, volume 6, page 178.

[158] Einar Juliusson. Charge composition and energy spectra of cosmic-ray nuclei at energies above 20 GeV per nucleon. *The Astrophysical Journal*, 191:331–348, 1974.

[159] Charles D. Orth et al. Abundances and spectra for cosmic-ray nuclei from lithium to iron for 2 to 150 GeV per nucleon. *The Astrophysical Journal*, 226:1147–1161, 1978.

[160] J. A. Lezniak and W. R. Webber. The charge composition and energy spectra of cosmic-ray nuclei from 3000 MeV per nucleon to 50 GeV per nucleon. *The Astrophysical Journal*, 223:676–696, 1978.

[161] J. H. Derrickson et al. A measurement of the absolute energy spectra of galactic cosmic rays during the 1976–77 solar minimum. *International Journal of Radiation Applications and Instrumentation. Part D. Nuclear Tracks and Radiation Measurements*, 20(3):415–421, 1992.

[162] M. Simon et al. Energy spectra of cosmic-ray nuclei to above 100 GeV per nucleon. *The Astrophysical Journal*, 239:712–724, 1980.

[163] Maurin, D., Melot, F., and Taillet, R. A database of charged cosmic rays. *Astronomy and Astrophysics*, 569:A32, Sep 2014.